Site C0021[1]

M. Strasser, B. Dugan, K. Kanagawa, G.F. Moore, S. Toczko, L. Maeda, Y. Kido, K.T. Moe, Y. Sanada, L. Esteban, O. Fabbri, J. Geersen, S. Hammerschmidt, H. Hayashi, K. Heirman, A. Hüpers, M.J. Jurado Rodriguez, K. Kameo, T. Kanamatsu, H. Kitajima, H. Masuda, K. Milliken, R. Mishra, I. Motoyama, K. Olcott, K. Oohashi, K.T. Pickering, S.G. Ramirez, H. Rashid, D. Sawyer, A. Schleicher, Y. Shan, R. Skarbek, I. Song, T. Takeshita, T. Toki, J. Tudge, S. Webb, D.J. Wilson, H.-Y. Wu, and A. Yamaguchi[2]

Chapter contents

[1] Strasser, M., Dugan, B., Kanagawa, K., Moore, G.F., Toczko, S., Maeda, L., Kido, Y., Moe, K.T., Sanada, Y., Esteban, L., Fabbri, O., Geersen, J., Hammerschmidt, S., Hayashi, H., Heirman, K., Hüpers, A., Jurado Rodriguez, M.J., Kameo, K., Kanamatsu, T., Kitajima, H., Masuda, H., Milliken, K., Mishra, R., Motoyama, I., Olcott, K., Oohashi, K., Pickering, K.T., Ramirez, S.G., Rashid, H., Sawyer, D., Schleicher, A., Shan, Y., Skarbek, R., Song, I., Takeshita, T., Toki, T., Tudge, J., Webb, S., Wilson, D.J., Wu, H.-Y., and Yamaguchi, A., 2014. Site C0021. *In* Strasser, M., Dugan, B., Kanagawa, K., Moore, G.F., Toczko, S., Maeda, L., and the Expedition 338 Scientists, *Proc. IODP,* 338: Yokohama (Integrated Ocean Drilling Program). doi:10.2204/iodp.proc.338.106.2014
[2] **Expedition 338 Scientists' addresses.**

Background and objectives

During Integrated Ocean Drilling Program (IODP) Expedition 338, a slope basin seaward of the megasplay was logged and cored at Site C0021. The slope basin, characterized in 3-D seismic data by stacked mass transport deposits (MTDs) (Strasser et al., 2011), was drilled and sampled in IODP Hole C0018A during IODP Expedition 333 and logged during Expedition 338 (Figs. **F1, F2, F3**) (Expedition 333 Scientists, 2012a) to establish the stratigraphy of a Quaternary mass-movement event and to sample the distal part of a thick MTD for analyzing its rheological behavior to constrain sliding dynamics and tsunamigenic potential. Site C0018 was drilled at a location where the MTD bodies wedge out and basal erosion is minimal.

During Expedition 338, logging while drilling (LWD) and coring to 294 and 194.5 meters below seafloor (mbsf), respectively, were conducted at Site C0021 (proposed Site NTS-1C) as contingency operations. This site is located ~2 km northwest of Site C0018 at a more proximal site for the MTDs analyzed at Site C0018 (Figs. **F2, F3, F4**). Therefore, LWD and coring at Site C0021 provided additional information on the nature, provenance, and kinematics of MTDs. By combining data from drilling and postexpedition laboratory experiments on samples from Sites C0021 and C0018 (see the **"Site C0018"** chapter [Strasser et al., 2014c]), we will improve our understanding of dynamics of submarine landslides as it relates to their tsunamigenic potential.

Hole C0021B core processing and measurements were divided into two phases: shipboard and shore based. The lack of ship time to completely process Hole C0021B cores on board during Expedition 338 dictated that only whole-round examinations could be performed; all remaining sampling tasks and analyses were deferred to a shore-based sampling party at the Kochi Core Center (KCC). Selected personnel from the science party, with some shore-based researchers, met at KCC in Kochi, Japan, from 25 to 30 April 2013 to participate in the sampling party and complete the site chapter reports.

Operations

Hole C0021A

The D/V *Chikyu* shifted from Hole C0018B, where LWD operations were just completed, and we prepared to run the LWD bot-

doi:10.2204/iodp.proc.338.106.2014

tom-hole assembly (BHA) into the hole from 2200 h on 26 December 2012. The seabed was tagged (water depth = 2940.5 meters below sea level [mbsl]) at 2330 h, and washing down to 40 mbsf in Hole C0021A commenced. From 40 mbsf, drilling ahead began at 0100 h on 27 December, and rotation speed gradually increased until reaching total depth (TD) (294.0 mbsf): 15 rpm × 1.8–2.5 kNm (40–45 mbsf), 30 rpm × 0–5.0 kNm (45–50 mbsf), 45 rpm × 0–5.0 kNm (50–60 mbsf), 60 rpm × 0–5.0 kNm (60–103 mbsf), and 80 rpm × 1.6–8.3 kNm (103–294 mbsf). TD was reached at 1100 h, and the hole was spotted with kill mud. While the LWD BHA was pulled out of the hole to the surface, overpull (80 kN) was observed from 88 to 101 mbsf; no other overpull was observed. The drill string was broken and racked back to the derrick while the vessel moved to the next site by 2030 h in preparation for LWD at IODP Site C0022.

Hole C0021B

After coring operations were completed in Hole C0022B, preparations began for testing the small-diameter rotary core barrel (SD-RCB) system at 1515 h on 6 January 2013; however, during make-up of the SD-RCB BHA, it was found that the head sub would not fit the other SD-RCB parts, so the test was cancelled at 1900 h. From that time, making up the hydraulic piston coring system (HPCS) BHA and running into the hole began for coring at Site C0021. By 0300 h on 7 January, the BHA reached 2930.7 m drilling depth below rig floor (DRF) while drifting to Site C0021 (the well center was reached by 0145 h). From 0330 h, troubleshooting the crown-mounted heave compensator began, during which operations continued in stand-by while the main Hydralift Power Swivel line was also cut and slipped. Upon completion at 1030 h, the coring BHA continued to be run into the hole to 2964 m DRF. The coring BHA was set to capture the first core while still above the seafloor. At 1145 h, while the BHA was at 2969 m DRF, the HPCS inner barrel was shot, penetrating 5.9 m. The seafloor was then determined as being 2972.5 m DRF (2944.0 mbsl). After the first core was taken, the BHA was washed down to 80 mbsf before coring resumed at 1515 h. There was a short pause in coring from 1845 to 2045 h while the wireline blowout preventer hydraulic hose leak was fixed. Coring resumed with Core 338-C0021B-5H at 108.5 mbsf from 2100 h and ended at Core 12H. Cores 10H, 11H, and 12H became stuck in the inner core barrel; therefore, coring continued with the extended punch coring system (EPCS) for the last two cores. Efforts to recover the stuck core liners continued on the rig floor until 9 January as coring continued. EPCS Core 13T was cut at 1730 h from 175.5 mbsf, and coring finished with EPCS Core 14T to a final TD of 194.5 mbsf at 2100 h on 8 December. Kill mud was spotted at 2230 h, and the EPCS BHA was pulled out of the hole to the surface, finishing at 0130 h on 10 January and ending operations related to Site C0021.

The ship began transit to Shimizu port, Japan, reaching port on the morning of 11 January. The scientists disembarked, and the expedition officially ended on 13 January.

Logging while drilling

LWD and measurement-while-drilling (MWD) data were collected in Hole C0021A to a TD of 294.0 mbsf. Both real-time and memory data from Schlumberger's MWD TeleScope and LWD geoVISION tool were collected (see the **"Methods"** chapter [Strasser et al., 2014a]), including drilling parameters, gamma radiation, resistivity, and azimuthal resistivity images. The gamma radiation, resistivity, and resistivity images were interpreted for lithologic and structural features, and three subunits were identified. Porosity and bulk density were calculated from resistivity, and in situ stress orientations were determined from compressional borehole breakout orientations.

Data processing

The seafloor was confirmed at 2969.0 m DRF based on the gamma ray and resistivity data extracted from the memory data.

Data quality

The overall quality of the processed logging data was determined to be good. Because of no rotation during wash down and drilling with low rotations per minute, poor quality resistivity images were recorded above 48.0 mbsf. Sharp horizontal lines, artifacts from ship heave and pipe vibration, were observed throughout the processed resistivity images. Missing data because of high stick-slip (>300 cycles/min) were also observed. Compressional borehole breakouts were only observed after pipe stand connections.

Logging units and lithostratigraphy

Site C0021 is located in a region of large MTDs, upslope from Site C0018. Hole C0021A penetrated slope basin sediment only. To maintain consistency with previous work (e.g., Expedition 333 Scientists, 2012b; Kimura et al., 2011; Strasser et al., 2011), a single logging unit is assigned to the entire drilled

interval (0–294 mbsf). The gamma ray data support this classification, as its character does not change significantly throughout; however, three subunits were identified based on changes in resistivity (Fig. F5).

Subunit IA (0–176.8 mbsf)

Subunit IA extends from the seafloor to 176.8 mbsf, exhibits three and a half broad gamma ray cycles, and generally has minor variations in the resistivity log (Fig. F6). From 0 to 8.8 mbsf, the gamma ray log exhibits a steady increase to ~70 gAPI and resistivity increases to a constant ~0.9 Ωm baseline. Between 8.8 and 57.5 mbsf, the gamma ray log exhibits fluctuations of ~10–20 gAPI around the 70 gAPI baseline, with some prominent spikes to low values at 23.2 and 48.4 mbsf (44 and 48.7 gAPI, respectively) and a spike to 87 gAPI at 39 mbsf. A gamma ray value low at 23.2 mbsf corresponds to a low spike (0.5 Ωm) in resistivity. Below this spike, resistivity continues to fluctuate around a 1.0 Ωm baseline, with minor increases and decreases to 69.9 mbsf, where the baseline steps down to ~0.9 Ωm, which it maintains to 144 mbsf. Between 57.5 and 96.6 mbsf, the gamma ray log decreases to ~50 gAPI at ~80 mbsf and then increases again to the baseline of ~75 gAPI. From 96.6 to 143 mbsf, the gamma ray log continues to exhibit 10–20 gAPI fluctuations around a baseline of ~75 gAPI, with small-scale fining and coarsening-upward sequences.

From 144 to 166.5 mbsf, gamma ray values gradually increase to ~92 gAPI. Through this same depth interval, the resistivity log exhibits two sharp increases and gradual decreases, peaking at 154 (1.75 Ωm) and 163 mbsf (1.4 Ωm), but no corresponding change is observed in the gamma ray log (Fig. F6). At 166.5 mbsf, gamma ray values sharply drop to ~70 gAPI.

Subunit IB (176.8–276.7 mbsf)

Resistivity through Subunit IB exhibits an overall gradual increase (from ~1.0 to 1.4 Ωm) but with some large-scale fluctuations (Fig. F6), whereas the gamma ray log continues to exhibit large-scale coarsening- and fining-upward cycles. At 276.7 mbsf, resistivity sharply drops from 1.2 to 1.0 Ωm and gamma ray values sharply drop from 100 to 82 gAPI, which marks the base of Subunit IB.

Subunit IC (276.7–294.0 mbsf)

Through Subunit IC, the gamma ray log exhibits an overall coarsening-upward cycle, most notably increasing from ~80 to ~100 gAPI between 276.7 and 285.3 mbsf. From 285.3 mbsf to the base of the hole (294.0 mbsf), gamma ray values gradually decrease to ~80 gAPI (Fig. F6).

Resistivity image analysis

The statically normalized shallow, medium, and deep button resistivity images were the primary images used for structural and geomechanical analyses. Two different resistivity ranges were selected to normalize the data: 0–5 Ωm was used for overall analysis and 0–10 Ωm was used to clearly identify highly resistive features. In the absence of a caliper measurement, the bit diameter was used as the borehole diameter and assumed to be constant.

Bedding and fractures

The dominant bedding dip direction is south-southeast, matching the expected trend for the slope sediment (Fig. F7). The majority of bedding dips are moderate (15°–40°), but many high-angle (>45°) beds are interspersed throughout (Fig. F5). Two distinct intervals exhibiting consistently high-angle (>50°) bedding planes with mixed dip directions were identified between 95 and 100 mbsf and between 148 and 178 mbsf. High-angle fractures were also observed in areas of chaotic, high-angle bedding, with fewer fractures observed in regions characterized by moderate bedding dips.

The upper interval of chaotic, high-angle bedding displays at least one clear switch in dip direction (from south to west-northwest) between 97 and 100 mbsf (Fig. F8A), and at least one of the bedding surfaces is nonplanar. A rapid change in dip direction and nonplanar bedding surfaces could result from deformation, possibly related to mass transport.

In contrast, the lower interval of chaotic, high-angle bedding does not show repeated switches in bedding dip direction throughout. Instead, the changes are either more gradational or separated by mottled, low-resistivity fractures (Fig. F8B). These observations suggest that deformation within this interval was different to that of the upper interval, perhaps reflecting a change in sediment properties. These intervals are interpreted to represent MTDs, also recovered in Hole C0021B (see **"Lithology"**). Within Subunit IB, several regions displaying patches of low resistivity are often found to occur either above or below distinct low-angle, low-resistivity beds or fractures (e.g., Fig. F8C). It is possible that these are pyrite-rich zones, as observed at Site C0018, located ~2 km to the southeast (see the **"Site C0018"** chapter [Strasser et al., 2014c]; Expedition 333 Scientists, 2012b).

Borehole breakouts

Well-developed (wide) borehole breakouts were observed at depths where drilling ahead was stopped during pipe connections (Fig. F8) (e.g., at 101.5 mbsf

[3070.5 m DRF], 139 mbsf [3108.0 m DRF], 177 mbsf [3146 m DRF], 215.5 mbsf [3184.5 m DRF], and 253.5 mbsf [3222.5 m DRF]). Breakouts could be associated with pipe stand connections because of lower annular pressure during connections or because of time-dependent evolution of breakouts.

Aside from the regular pipe connection–related breakouts (approximately every 38 m), no other failures were observed in Subunit IA. However, below 225 mbsf in Subunits IB and IC, breakouts were frequently observed, although they were generally much thinner than those in Subunit IA (<20° width). Additionally, the width of pipe connection–related breakouts increased from ~50° to >70° at depths >215 mbsf. The average orientations of paired breakout intervals were 42° and 222°, indicating a northwest–southeast direction of maximum horizontal stress (S_{HMAX}). This direction is comparable to the convergence vector of the Philippine Sea plate and matches the overall trend observed at other IODP Nankai Trough Seismogenic Zone Experiment (NanTroSEIZE) sites (C0001, C0004, C0006, and C0009) (Chang et al., 2010; Lin et al., 2010; Byrne et al., 2009; Kinoshita et al., 2008) and Ocean Drilling Program Site 808 (Ienaga et al., 2006; McNeill et al., 2004).

Physical properties

Estimation of porosity and bulk density from resistivity

We estimated porosity using Archie's law (Archie, 1947) (see the **"Methods"** chapter [Strasser et al., 2014a]). Cores from Site C0021 were subject to post-expedition analysis; thus, the parameters necessary for use of Archie's law were taken from a variety of sources. Seawater electrical resistivity was calculated using the temperature profile that was estimated for Hole C0018A during Expedition 333. Hole C0018A is ~2 km from Hole C0021A and should provide a reasonable estimate for temperature at Site C0021. The temperature at the seafloor is estimated at 1.48°C, with an average thermal gradient of 63°C/km (Expedition 333 Scientists, 2012b). Because of uncertainties in the Archie parameters estimated for Site C0018 (see the **"Site C0018"** chapter [Strasser et al., 2014c]), parameters a = 1 and m = 2.4 estimated for Kumano Basin sediments at IODP Site C0002 during IODP Expedition 314 were applied to Hole C0021A (Expedition 314 Scientists, 2009). Bulk density was estimated from the resistivity-derived porosity using the average grain density (ρ_g) of 2.66 g/cm³ found in Hole C0018A (see the **"Site C0018"** chapter [Strasser et al., 2014c]; Expedition 333 Scientists, 2012b).

The resistivity-derived porosity and bulk density depth trends are shown in Figure **F5.** Within Subunit IA, porosity generally decreases rapidly from ~80% at the seafloor to 61% at 35 mbsf. From 35 to 70 mbsf, porosity is slightly scattered but is generally constant at 61% then increases slightly to 64%. From 70 to 162 mbsf, porosity decreases from 64% to 53%. A large negative spike to 46% is at 152 mbsf. From 162 to 166.5 mbsf, porosity increases from 53% to 57%. From 166.5 to 198 mbsf, porosity decreases to 48%, below which it spikes to 57% at 203 mbsf and decreases rapidly to 52% at 204 mbsf. Porosity then generally decreases to 47% at 231 mbsf before generally increasing to 57% at 246 mbsf. At 246 mbsf, porosity again generally decreases to 46% at 271 mbsf before increasing to 51% at the base of Subunit IB at 276.7 mbsf. Within Subunit IC, porosity decreases to 49% at 284 mbsf, then increases to 53% at 288 mbsf, and finally decreases to 50% near the base of Hole C0021A (294.3 mbsf).

Trends in resistivity-derived bulk density mirror those described above for the resistivity-derived porosity because reported bulk density values are a mathematical manipulation of the derived porosity values (Fig. **F5**). Generally, bulk density increases from ~1.2 g/cm³ at the seafloor to ~1.9 g/cm³ at the base of Subunit 1A. Three increasing trends correlate to the decreasing trends described for porosity. Within Subunit IB, bulk density decreases from ~1.9 to 1.8 g/cm³. Bulk density through Subunit IC to the base of Hole C0021A is slightly scattered at ~1.8 g/cm³.

Lithology

Hole C0021B was drilled to 194.5 mbsf. A total of 14 cores were recovered in two intervals: 0–5.9 and 80–194.5 mbsf. Core recovery was high, often exceeding 100% because of core expansion. Core quality was generally high, although pervasive core disturbance (flow-in and liner jamming in the core barrel) occurred in Cores 338-C0021B-11H and 12H, which led to a change in coring system to acquire Cores 13T and 14T (see **"Operations"**).

The recovered sedimentary succession is divided into one lithologic unit (I), including two subunits (IA and IB), on the basis of visual core descriptions (including smear slides) and X-ray computed tomography (CT) (Fig. **F9;** Table **T1**). These subunits are consistent with LWD data from Hole C0021A (see **"Logging while drilling"**) and regional seismic stratigraphy (Strasser et al., 2011). The naming convention used here is consistent with nearby Site C0018 (Expedition 333 Scientists, 2011). However, Subunits

IA and IB defined here and at Site C0018 are equivalent to Subunit IA at Site C0022 (see **"Lithology"** in the "Site C0022" chapter [Strasser et al., 2014d]), according to regional seismic stratigraphic interpretation (Strasser et al., 2011).

Lithologic Subunit IA is composed of mottled greenish gray silty clay with local thin interbeds of fine sand and ash layers. Subunit IA also contains intervals with chaotic and distorted bedding interpreted to be evidence of MTDs. The Subunit IA/IB boundary is defined at 176.16 mbsf. Subunit IB is composed of a succession of thin sand beds interbedded with silty clay and local ash layers. Individual sand beds are generally 2–10 cm thick (35 cm thick maximum) (Fig. **F10**) and spaced ~20–30 cm apart.

Subunit IA (slope basin)

Interval: Sections 338-C0021B-1H-1, 0 cm, to 13T-1, 66 cm

Depth: 0–176.16 mbsf

The dominant lithology of Subunit IA is mottled greenish gray silty clay that contains a variable amount of calcareous nannofossils, foraminifers, siliceous biogenic debris (sponge spicules, diatoms, silicoflagellates, and radiolarians), and volcanic ash (Fig. **F11;** see Site C0021 smear slides in **"Core descriptions"**). Within the silty clay, minor interbeds of fine sand and volcanic ash vary significantly in thickness and frequency (Figs. **F10, F11A**). A few beds with recognizable fining-upward successions are observed. Such beds typically begin with sharp-based ~2 cm dark gray sand, grading upward through burrowed silty clay. Dispersed volcanic ash (possible lapilli), discrete pumice fragments (granule to pebble size), and thin ash layers are widely distributed through most of the core sections.

Faint green–brown color banding and mottling is common throughout most of Subunit IA, interpreted to be a signature of bioturbation. Bioturbation includes *Chondrites, Zoophycos*, possible *Trichichnus*, and other discrete burrows, many of which are pyritized. Bioturbation is particularly apparent in CT images as thin, subvertically oriented ribbons with high CT values.

Bulk mineral compositions (total clay, quartz, feldspar, and calcite) were estimated by X-ray diffraction (XRD). Calcite content ranges between 4 and 35 wt%, with an average of ~18 wt%. A trend toward diminishing carbonate content with depth is observed (Fig. **F12;** Table **T2**). Total clay, quartz, and feldspar contents are variable across the depth range of this subunit around average values of 44.6, 20.7, and 16.5 wt%, respectively (Fig. **F12**).

Two MTD intervals, including mud clasts, chaotic bedding, and steeply dipping beds, occur within Subunit IA (Table **T3;** Fig. **F13**) (see **"Mass transport deposits"**). The style of deformation is distinct from drilling/coring/handling and flow-in disturbance observed in Cores 338-C0021B-11H and 12H. The first interval (MTD A) occurs between 94.16 and 116.75 mbsf. A second, thicker MTD interval (MTD B) occurs between 133.76 and 176.16 mbsf.

Subunit IB (sand-rich slope basin)

Interval: Sections 338-C0021B-13T-1, 66 cm, through 14T-CC

Depth: 176.16–194.5 mbsf (end of core)

Subunit IB consists of interbedded fine-grained sand and silty clay (Fig. **F11**). The top of Subunit IB is defined at 176.16 mbsf at the first occurrence of repeating sand beds with spacing of 20–30 cm. This depth marks the boundary between the predominantly silty clay above (Subunit IA) and a succession of thin, frequent sand beds with minor interbeds of silty clay below (Subunit IB). This depth also corresponds to a prominent decrease in shear strength and increase in porosity (**"Physical properties"**).

Bulk mineralogy of the silty clay, determined by XRD, shows higher feldspar and quartz values in this subunit compared to Subunit IA (Fig. **F12;** Table **T2**), whereas the ratio of feldspar to quartz + feldspar remains constant across the subunit boundary. Mean values for calcite are low in Subunit IB, ranging from 3.1 wt% to below detection limit (<0.5 wt%).

Individual sand beds in Subunit IB are subhorizontal and typically a few centimeters to a few decimeters thick; these beds have a sharp base and a fining-upward grading (Fig. **F11B**). Sand bed spacing is ~20–40 cm. Sand mineralogy is dominated by quartz, feldspar, and metasedimentary lithic fragments (Fig. **F11;** Site C0021 smear slides in **"Core descriptions"**). Many of the sands are dark gray to nearly black, a coloration that arises from the high content of authigenic pyrite, similar to what has been described at Site C0022 (see **"Lithology"** in the "Site C0022" chapter [Strasser et al., 2014d]).

Mass transport deposits

MTD intervals (MTDs A and B) were defined based on the supporting information of visual core descriptions, X-ray CT images, physical properties, measurements of structural geology elements, and seismic data interpretation (Fig. **F13;** Table **T3**). Each MTD corresponds to

- The occurrence of mud clasts, tilted bedding, and/or chaotic bedding,

- An increase in shear strength and a decrease in porosity (see **"Physical properties"**),
- The occurrence of shear zones/faults (see **"Structural geology"**), and
- A semitransparent seismic facies (see **"Core-log-seismic integration"**).

The tops of MTDs A and B are defined as zones of mud clasts capped by thin, draping sand. Mud clasts are round and are 1–3 cm in the longest dimension. Below the mud clasts, a zone of variable chaotic/tilted/homogeneous bedding occurs. The bases of the MTDs are not obvious visually or in CT images. Therefore, the bases of the MTDs are defined based on the supporting data of structural elements and physical properties. Specifically, the base of MTD A is defined as the last occurrence of a shear zone in Section 338-C0021B-5H-8, 6 cm (116.75 mbsf). This also corresponds to the base of a zone with relatively high shear strength. The base of MTD B (176.16 mbsf) is defined as the last occurrence of a shear zone in Section 13T-1, 80 cm (see **"Structural geology"**). This also corresponds to the base of a zone of relatively high shear strength (see **"Physical properties"**). Preliminary core-log-seismic integration suggests that MTD B is correlative to MTD 6 at Site C0018 (see **"Core-log-seismic integration"**).

X-ray fluorescence analyses

X-ray fluorescence (XRF) analyses were performed on 24 samples from Hole C0021B to estimate the bulk chemical composition of the sediment and to characterize compositional trends with depth and/or lithologic characteristics (Fig. **F14;** Table **T4**).

The silty clay of Subunit IA is characterized by relatively low SiO_2 and Al_2O_3 content (~60 and 15 wt% on average, respectively). Below ~150 mbsf, these increase to higher values reaching 63.3 and 16.8 wt%, respectively, in bulk silty clay samples from sand-rich Subunit IB (Fig. **F14**). This downhole increase may be explained by a higher proportion of siliciclastic grains in Subunit IB. In contrast, Subunit IA contains somewhat higher CaO content. The marked decrease in CaO from ~9 wt% in Subunit IA to ~3 wt% in Subunit IB is consistent with the very low calcite content observed by XRD below ~176 mbsf and $CaCO_3$ determined by CARB measurements (see **"Geochemistry"**).

Large variations observed for almost all the major elements at various depths (e.g., at 91.8 mbsf; Fig. **F14**) likely result from the sampling of specific lithologies such as volcaniclastic sand beds and volcanic ash layers.

In general, the lower part of Subunit IA (i.e., where data are available below 80 mbsf) shows rather homogeneous composition of Al_2O_3, Fe_2O_3, K_2O, P_2O_5, MgO, and TiO_2 (Fig. **F14;** Table **T4**). The bulk composition of the MTDs does not differ from the composition of the homogeneous overlying strata. However, below 150 mbsf, and thus within the lower part of MTD B, systematic trends toward Subunit IB potentially suggest that the MTD partly incorporated the Subunit IB strata.

Summary

Sediment in Hole C0021B was drilled to 194.5 mbsf within the slope basin seaward of the megasplay fault. Cores were collected in two zones: 0–5.9 and 80–194.5 mbsf. Two lithologic subunits are defined: Subunits IA and IB. Subunit IA is dominated by silty clay and contains two MTDs. Subunit IB contains thin, frequent sand interbedded with silty clay. Volcaniclastic ash layers are present in both units. This succession is lithologically similar to previously drilled holes in this basin (Expedition 333 Scientists, 2011; Expedition 316 Scientists, 2009a, 2009b; Strasser et al., 2009, 2011; Kimura et al., 2011).

Structural geology

Structures observed in cores retrieved from Hole C0021B are mainly of three types: bedding, faults, and shear zones. Fissility was rarely observed and was likely induced by drilling because it is systematically observed at the very top of the first section of the cores.

Bedding

A total of 98 bedding measurements were made on Hole C0021B cores (Fig. **F15**). In undisturbed slope basin sediment, the recognition of bedding is straightforward. It is, however, harder to recognize in MTD intervals. In such cases, X-ray CT images were also used for bedding identification and measurement. Bedding dips mostly (74 of 98 measurements) between 0° and 20° but occasionally between 20° and 50°. In terms of bedding dip angles versus depth, three intervals are clearly visible. The upper interval from 80 to ~100 mbsf is characterized by gentle dip angles (<20°). The intermediate interval from ~100 to 180 mbsf is characterized by dip angles between 0° and 50°, likely reflecting sedimentary disturbance during MTD emplacement. The lower interval (correlative to lithologic Subunit IB), with one exception likely linked to a local disturbance (e.g., slumping), is characterized by gentle dip angles between 0° and 16°.

Figure **F16** shows the poles to bedding for Subunits IA and IB reoriented based on paleomagnetic data.

No strong preferred orientation can be recognized, but east–west strikes seem to predominate in Subunit IA.

Minor faults

A total of 19 minor faults were observed in Hole C0021B cores. These faults are characterized by sharp fault surfaces, along which cores can be split away. Fault surfaces are mostly planar and sometimes bear fine striations (Fig. F17A). Rakes of striations are close to 90°, suggesting predominantly dip slip. A normal sense of slip could be determined for two minor faults. Offset beds indicate separation of 6 and 37 mm for these two faults. A reverse sense of slip along one minor fault (interval 338-C0021B-7H-2, 84–90 cm) is suggested by intense striations on the restraining bends arrangement of possible P surfaces, but the lack of offset markers on either side of the fault precludes further confirmation.

Most faults (78%) cluster in two intervals: 94–96 and 129–134 mbsf (Fig. F18). Most faults dip between 44° and 66°, but three faults dip between 74° and 88°. Some faults observed in MTDs clearly offset mud clasts, indicating that faulting postdates MTD emplacement (Fig. F19).

Figure F20A shows the projections of faults from intervals for which corrections based on paleomagnetic data were available (the section between MTDs A and B). Faults preferentially strike north–south to northwest–southeast and dip consistently to the west or southwest. The scarcity of striations borne by the fault surfaces precludes any interpretation in terms of paleostress.

Shear zones

A total of 45 shear zones were measured in cores from Hole C0021B. Shear zones typically appear on cores as faint, 1 or 2 mm thick, rectilinear zones that are slightly darker than the surrounding host sediment (Fig. F17B). On X-ray CT images, shear zones clearly appear as bright zones with higher density than the host sediment. Although most shear zones are ~1 or 2 mm thick, several centimeter-thick shear zones were also observed (e.g., Fig. F17C). Particularly, the 1 cm thick shear zone observed at interval 338-C0021B-13T-1, 60–66 cm (Fig. F21), could represent the basal shear zone of MTD B (see "Lithology"). Sense of displacement along shear zones could not be determined. However, in one case (interval 10H-7, 1–21 cm), the en echelon arrangement of three shear zone segments suggests a reverse component of slip, but the lack of independent indicators, such as offset markers, prevents further confirmation.

Shear zones are mainly observed in two intervals (Fig. F18): 100–130 and 147–176.16 mbsf. In either interval, shear zones dip gently (~20°) to almost vertical but mostly dip between 30° and 70°. Unlike faults, shear zone attitudes are scattered and no preferred orientation can be observed (Fig. F20B).

Summary

Structural observations of core from Hole C0021B confirm the conclusions obtained in nearby Hole C0018A (Expedition 333 Scientists, 2012b). Slope sediments are characterized by flat or gently dipping bedding and a lack of shear zones. In contrast, MTDs are characterized by a wider range of bedding dip angles (0°–50°) and by the occurrence of millimeter to centimeter thick shear zones, reflecting disruption during emplacement. The post-MTD emplacement deformation style is characterized mostly by normal-sense faulting.

Biostratigraphy

Preliminary biostratigraphy for Hole C0021B is based on shore-based examination of calcareous nannofossils and planktonic foraminifers. Ages constrained by calcareous nannofossils and planktonic foraminifers are generally consistent; both nannofossils and foraminifers indicate that sediment at the bottom of the hole at 195 mbsf is ~1.3 Ma in age. Biostratigraphic age datums are generally in stratigraphic order; however, calcareous nannofossils indicate age reversals and thus the presence of older sediment mixed with younger sediment at ~109 mbsf and within the interval between 146.48 and 175.17 mbsf, which are the intervals of MTDs A and B (see "Lithology").

Calcareous nannofossils

Calcareous nannofossils are abundantly observed, and their preservation is generally good. A total of 15 samples recovered from 338-C0021B-1H-CC (5.88 mbsf) through 14T-CC (194.48 mbsf) in Hole C0021B were examined (Table T5).

Sample 338-C0021B-1H-CC (5.88 mbsf), which is the uppermost sample examined, contains abundant *Emiliania huxleyi* (Table T5). Therefore, the interval above this sample is correlated with calcareous nannofossil Zone NN21, corresponding to ages younger than 0.291 Ma (see Fig. F15 in the "Methods" chapter [Strasser et al., 2014a]). The last occurrence (LO) of *Pseudoemiliania lacunosa* (0.436 Ma) is placed between Samples 338-C0021B-1H-CC and 2H-CC (89.48 mbsf) because of the presence of *P. lacunosa* below the latter. This event coincides with the base of Zone NN20. Reentrance (RE) of medium *Gephyro-*

capsa spp. (≥4 µm and with a parallel bar oriented to the short axis of a specimen) without *Reticulofenestra asanoi* indicates that Samples 338-C0021B-2H-CC (89.48 mbsf) through 7H-CC (136.98 mbsf) correspond to 0.436–0.903 Ma.

Sample 338-C0021B-5H-1WR (108.98 mbsf) is older (1.24–1.34 Ma) than the samples above and below based on the presence of *Gephyrocapsa* spp. (>5.5 µm) (Table **T5**), indicating that there is a chronostratigraphic discontinuity between 108.5 and 118 mbsf. This interval correlates to MTD A (94.16–116.75 mbsf), suggesting that older sediment was eroded and mixed during MTD emplacement. Moreover, there are also significant stratigraphic discontinuities between Samples 338-C0021B-8H-CC (146.48 mbsf) and 12H-CC (175.17 mbsf). This interval in total corresponds to the age between the LO of *P. lacunosa* (0.436 Ma) and the RE of medium *Gephyrocapsa* spp. (≥4 µm) (1.04 Ma), but older sediments are apparently frequently intercalated. This interval corresponds to MTD B (133.76–176.16 mbsf). The lower part of the examined sequences (Samples 338-C0021B-13T-CC [183.75 mbsf] and 14T-CC [194.48 mbsf]) are placed between the LO of *Gephyrocapsa* spp. (>5.5 µm) (1.24 Ma) and the LO of *Helicosphaera sellii* (1.34 Ma).

Planktonic foraminifers

Planktonic foraminifers are abundant through the 15 samples examined, and their preservation is generally good (Table **T6**). The LO of *Truncorotalia tosaensis* (0.61 Ma) is placed between Samples 338-C0021B-3H-CC (98.98 mbsf) and 4H-CC (108.48 mbsf). In addition, the LO of *Globoturborotalita obliquus* (1.30 Ma) is placed between Samples 13T-CC (183.75 mbsf) and 14T-CC (194.48 mbsf).

Geochemistry

Inorganic geochemistry

Interstitial water geochemistry

Interstitial water (IW) was sampled (1 IW sample/core) from 3.7 to 186.4 mbsf in Hole C0021B, except for the interval between 5.9 and 80 mbsf, which was washed down without coring. Table **T7** shows the analytical results of IW analyses, and Figures **F22, F23,** and **F24** show the variations of IW chemistry with depth.

Although very close to the sea bottom, the uppermost sample at 3.7 mbsf shows IW chemistry different from that of seawater (e.g., pH 8.01 is slightly lower than that of seawater of ~8.2). The chemistry of samples below 80 mbsf is clearly different from the uppermost one: refractive index, pH, and chlorinity are lower than seawater, possibly indicating freshwater input and subsequent dilution. Chlorinity slightly increases with increasing depth between 80 and 170 mbsf and decreases again below 170 mbsf. The origin of freshwater could be dissociation of gas hydrates, clay mineral dehydration, and/or fluid flow along a fracture zone. The drilled interval lies within the hydrate stability zone; therefore, gas hydrate dissociation is a plausible scenario, although no hydrates were directly observed in the cores.

SO_4^{2-} concentration decreases from the uppermost sample to that of IW at 80 mbsf and does not change below that depth. Alkalinity and PO_4^{3-} are higher in IW at 80 mbsf than the uppermost one and then decrease with increasing depth to 170 mbsf and increase again to the bottom of the hole. These three components should behave concordantly with microbial activity (i.e., aerobic respiration consuming oxygen from oxoacid). In contrast, Br^- and NH_4^+ increase with increasing depth, possibly because of decomposition and dissolution of organic matter. Alkaline metal elements (Li, Na^+, K^+, Rb, and Cs) and Mg^{2+} and Ba should behave according to those affinities of adsorption. Such an adsorption affinity depends on the radius of the hydrated ion and generally becomes stronger with increasing mass and valence among cations (Fuerstenau et al., 1981; Piasecki et al., 2010). Among those elements, K^+, Rb, Cs, Mg^{2+}, and Ba decrease and Na^+ and Li increase with increasing depths to 170 mbsf, probably because of cation exchange reactions. The Ca^{2+} and Sr increase with depth may be caused by the higher dissolution rate of plagioclase and/or carbonate minerals than adsorption.

Among the trace elements not described above, Si, Fe, Mn, and Cu are higher in sediment deeper than 80 mbsf than in the sample at 3.7 mbsf. Si is released from minerals via hydration and dissolution. Mo behaves similar to Si. Fe and Mn should be partly released via dissolution of minerals and should also be partly released via desorption in association with a reducing condition of IW. Fe, Mn, and Cu decrease with increasing depth below 80 mbsf in a manner similar to the other elements (B, V, Pb, Zn, and U).

When investigating the different changes in element concentrations more closely, variations in trend and scatter seem to relate to MTDs (see **"Lithology"**). MTD A is located between ~94 and 116 mbsf, and MTD B occurs between ~133 and 176 mbsf. However, a systematic pattern that would describe every component is hardly recognizable (Figs. **F22, F23, F24**). For example, alkalinity, chlorinity, pH, Mg^{2+}, B, Li, PO_4^{3-}, and Mn show a change in slope of the overall trend across MTDs tops and bases, whereas

Ba, Rb, and NH_4^+ remain unaffected. In general, the most prominent excursions occur close to the base of MTD B (i.e., close to the Subunit IA/IB boundary) at ~170 mbsf. At this depth, most data show an overall change or even a reversal in trend. The reasons for these observations remain unclear and will be the subject of future postcruise studies.

Geochemistry of liquid in core liner

Two water samples were taken from the core liner at 0 and 179.4 mbsf to check the chemical composition of mud water that may have contaminated the IW. Results of shipboard analyses are shown in Table T8. The liquid in core liner (LCL) from the top of the core (0 mbsf) is the same as seawater. The water from 179.4 mbsf has a slightly lower concentration of chlorinity (551 mM) than that of the LCL at 0 mbsf (555 mM) as well as SO_4^{2-} (25 mM at 0 mbsf and 20 mM at 179.4 mbsf).

Organic geochemistry

Gas chemistry

Headspace gas and void gas samples were taken from cores in Hole C0021B, and concentrations of methane, ethane, and propane, as well as carbon isotopic compositions of methane ($\delta^{13}C$-CH_4), were measured (Tables T9, T10, T11).

Gas chemistry data (methane concentration, ethane concentration, ratio of $C_1/[C_2 + C_3]$, and $\delta^{13}C$-CH_4) obtained by conventional oven-heating gas extraction are compared with those obtained by NaOH-addition gas extraction (Fig. F25). Ethane concentration in headspace gases obtained by the oven-heating method was higher than that obtained by the NaOH addition method, whereas this difference was not observed for methane concentrations. This suggests that the difference likely results from higher solubility of ethane than that of methane. No significant difference between the two methods was found in the $\delta^{13}C$-CH_4 data.

The vertical distribution of methane, ethane, and propane concentrations are shown in Figure F26. Methane peaks appear at ~100 mbsf. Ethane increases with depth. Propane was not detected except at ~150 mbsf. Void gas samples were collected between 85 and 185 mbsf (Table T11), implying that degassing of the sediment took place at room temperature and atmospheric pressure. This suggests that gas generation took place at in situ conditions, as observed at Site C0022 (see "Geochemistry" in the "Site C0022" chapter [Strasser et al., 2014d]), and that sediments in the slope basins are rich in gas. Ethane increases with depth above 200 mbsf, as also observed at Site C0022.

Depth profiles of $C_1/(C_2 + C_3)$ ratios and $\delta^{13}C$-CH_4 are shown in Figure F27. $C_1/(C_2 + C_3)$ ratios decrease with increasing depth to 200 mbsf. $\delta^{13}C$-CH_4 values are almost constant throughout the whole cores at this site. $C_1/(C_2 + C_3)$ ratios and $\delta^{13}C$-CH_4 values can be used to determine the origin of methane (Bernard et al., 1978). A plot of data from Site C0021 on the Bernard diagram (Fig. F28) indicates that methane distributed at Site C0021 is of microbial origin rather than of thermogenic origin.

Although the highest concentrations of methane and total gas occur within MTDs A and B, respectively, a direct correlation between gas concentration and MTDs is difficult to draw (Fig. F26). The negative trend with depth of $C_1/(C_2 + C_3)$ ratios and constant $\delta^{13}C$-CH_4 values remain unaffected across MTDs or subunit boundaries, indicating no remarkable change in gas composition within MTDs or across the stratigraphic boundaries.

Inorganic carbon, total carbon, total nitrogen, and total sulfate

Calcium carbonate ($CaCO_3$) and total organic carbon (TOC) concentrations and TOC/total nitrogen (TN) (C/N) and TOC/total sulfur (TS) (C/S) ratios were determined from total inorganic carbon (IC), total carbon, TN, and TS measurements of sediment samples from 3.7 to 186.4 mbsf. $CaCO_3$, TOC, TN, and TS concentrations and C/N ratios are plotted in Figure F29 and listed in Table T12.

$CaCO_3$ in sediment at Site C0021 ranges from 2.9 to 23.6 wt%, with an average of 12.0 wt% (Fig. F29). Between 80 and 92 mbsf, $CaCO_3$ sharply decreases from 23.6 to 2.9 wt%. $CaCO_3$ then scatters around ~10 wt% between 100 and 175 mbsf before decreasing to lower values in Subunit IB, which is consistent with low calcite content values in Subunit IB determined from XRD analyses (see "Lithology"). TOC in sediment ranges from 0.12 to 0.76 wt% with a median of 0.46 wt%. TOC values in surface sediment above 5 mbsf are higher than those below 80 mbsf. TN concentration of sediment ranges from 0.020 to 0.090 wt% with an average of 0.070 wt%. TN values in surface sediment are higher than those below 80 mbsf. Below 80 mbsf, TN values are almost constant throughout the core. The lowest value was obtained at 92 mbsf, where $CaCO_3$ and TOC values also show the lowest values at Site C0021. At ~170 mbsf, $CaCO_3$, TN, and TS indicate a change in trend to lower values.

C/N ratio ranges from 5.0 to 8.4 with an average of 6.6 (Fig. F29) and is almost constant throughout the core. This suggests that organic matter at Site C0021 is dominantly of marine origin throughout the sec-

tion (Meyers, 1997). TS concentration in sediment is generally low with an average of 0.31 wt%. A few higher values can be associated with the precipitation of sulfide, which will be evaluated by shore-based analyses of samples.

Like the gas data, correlations between $CaCO_3$, TOC, TN, and TS remain to be established. Moreover, the increase in data scattering and deviation from the overall trend observed across MTDs (Fig. F29) should be addressed by future postcruise studies.

Physical properties

Physical properties measured on core samples from Site C0021 provide insights into the evolution of MTDs and associated deformation by comparing results from nearby Site C0018, where coring was conducted during NanTroSEIZE Stage 2 Expedition 333 (Expedition 333 Scientists, 2012b). Physical properties on core samples also help calibration and correlation with LWD data (see **"Logging while drilling"** and **"Core-log-seismic integration"**).

Whole-round multisensor core logger

Whole-round cores were analyzed using the whole-round multisensor core logger (MSCL-W). The results of gamma ray attenuation (GRA) density, magnetic susceptibility, natural gamma radiation (NGR), and electrical resistivity measurements (see the **"Methods"** chapter [Strasser et al., 2014a]) are summarized in Figure F30. Ultrasonic *P*-wave velocity (V_P) measurements on Core 338-C0021B-1H are summarized in Figure F31. GRA density increases with depth similarly to bulk density of moisture and density (MAD) measurements discussed in **"Moisture and density measurements (discrete cores)."** Magnetic susceptibility is mostly constant in lithologic Subunit IA, except for a slight increase above ~100 mbsf and higher values of magnetic susceptibility in lithologic Subunit IB. NGR generally increases with depth, and a rapid increase with depth is observed in the intervals from 80 to 100 mbsf in Subunit IA and below 176 mbsf in Subunit IB. Electrical resistivity generally increases with depth, with a slight drop at the Subunit IA/IB boundary. Only Core 338-C0021B-1H shows good quality V_P measured on the MSCL-W, whereas the other cores yield poor V_P data quality because of poor contact between the liner and sediment. V_P increases from 1.45 to 1.50 km/s within the top 6 m of core sediment.

Moisture and density measurements (discrete cores)

A total of 122 discrete samples from Hole C0021B were measured for MAD. MAD data from Hole C0021B are summarized in Table T13 and Figure F32. Between 1.2 and 194 mbsf, bulk density ranges from 1.40 to 1.95 g/cm^3, grain density ranges from 2.6 to 2.85 g/cm^3, and porosity ranges from 45% to 75%. Both bulk density and porosity change generally with depth; bulk density increases and porosity decreases. The slope of increasing and decreasing trends in bulk density and porosity, respectively, is steeper between 80 and 110 mbsf. Sand samples show higher bulk density and lower porosity than mud samples, whereas ash samples show similar values to those of mud samples.

It should be noted that MAD measurements on cluster samples, which were taken during whole-round core (WRC) sampling for IW samples and community WRC samples, were conducted on the *Chikyu*, whereas MAD measurements on samples taken from working halves were conducted at the Japan Agency for Marine-Earth Science and Technology (JAMSTEC) KCC during a core opening and sampling party (see **"Operations"**). The data show no difference between the measurements on the *Chikyu* and those at KCC, although different pycnometers and balances were used.

Thermal conductivity (whole-round cores and working halves)

Thermal conductivity was measured on whole-round cores from 3.2 (Core 338-C0021B-1H) to 185.3 mbsf (Core 14T) using a needle probe sensor. There is a clear boundary in thermal conductivity that corresponds to the lithologic Subunit IA/IB boundary. Thermal conductivity is generally constant at ~1.0 W/(m·K) above 177 mbsf in lithologic Subunit IA and increases to ~1.2 W/(m·K) in lithologic Subunit IB (Fig. F33).

Electrical resistivity (working halves and discrete core samples)

A total of 197 electrical resistivity measurements were conducted on working-half cores between 1.2 and 194 mbsf using the Wenner four-pin array probe. Each measurement was recorded in the dominant lithology types per section. Electrical resistivity ranges from 0.41 to 5.27 Ωm with an average of 1.02 Ωm and generally increases with depth as expected from the densification and porosity loss (Fig. F34; Table T14). The higher values at ~150 mbsf and below 178 mbsf reflect sand layers. Resistivity measured with the Wenner probe is almost the same as that of MSCL-W measurements. This is different from the data from other sites (C0002 and C0022), which show lower resistivity measured by Wenner probe than those of MSCL-W measurements (see **"Physical properties"** in the "Site C0002" chapter

and "Physical properties" in the "Site C0022" chapter [Strasser et al., 2014b, 2014d]). This is possibly because the correct values of standard seawater resistivity were not obtained because of the use of a small container when the measurements on cores from Sites C0002 and C0022 were conducted. Unexpectedly low resistivity values obtained for cores at Sites C0002 and C0022 are probably due to overestimation of seawater impedance.

Shear strength (working halves)

Undrained shear strength of sediment from Hole C0021B was determined using a vane shear device and a pocket penetrometer (see the "Methods" chapter [Strasser et al., 2014a]). Undrained shear strength based on penetrometer measurements varies from 4.9 to 246.9 kPa, with an average of 86.7 kPa, whereas undrained shear strength based on vane shear measurements ranges from 7.7 to 178.1 kPa, with an average of 58.2 kPa (Fig. F35; Table T15). Although the data are scattered and vane shear measurements result in overall smaller undrained shear strength, both penetrometer and vane shear data can be divided in distinct intervals. Undrained shear strength of the material from the uppermost 5 mbsf (Core 338-C0021B-1H) is 20–29 kPa, which is much weaker than that of the material starting at 80 mbsf. Most likely, higher porosity and less-indurated material in the uppermost interval are responsible for this observation. Between 80 and 106 mbsf, undrained shear strength increases from ~50 kPa up to 114.5 kPa. Between 106 and 116 mbsf, the material becomes weaker again and undrained shear strength drops to 18–33 kPa. Below 116 mbsf, undrained shear strength increases with depth again, with a slope change at 150 mbsf, and reaches the highest values of 246.9 kPa (penetrometer) and 178.1 kPa (vane shear) at 170 mbsf. Undrained shear strength quickly drops to ~100 kPa (penetrometer) and ~50 kPa (vane shear) at 170 mbsf, and the values remain almost constant below that depth. Undrained shear strength increases with depth within both MTDs and decreases rapidly at the base of the MTDs. This trend was also observed in MTDs at Site C0018 (Expedition 333 Scientists, 2012b).

Color spectroscopy (archive-half cores)

The results of color reflectance measurements using the color spectroscopy logger (MSCL-C) are summarized in Figure F36. General trends are a slight increase in L* and a* and a decrease in b* with depth. L* ranges from 11 to 61, a* ranges from –6.8 to 7.3, and b* ranges from –4.2 to 10.7.

Paleomagnetism

Hole C0021B

A total of 178 discrete samples were collected from Hole C0021B at a frequency of two samples per standard section (~140 cm) at the KCC. Magnetic measurements on the samples were then conducted using a magnetometer (2G Enterprises, model 760-3.0) at JAMSTEC, Yokosuka. Natural remanent magnetization (NRM) demagnetized directions and intensities of all samples at 0, 5, 10, 20, 30, 40, 50, and 60 mT peak fields were measured to identify characteristic remanent magnetization.

Typical demagnetization behavior of samples is shown in Figure F37. The large vertical component observed between 0 and 5 mT is generally considered a result of drilling-induced overprints (Fig. F37A) (e.g., Gee et al., 1989). Depth profiles of declination, inclination, and intensity after demagnetization at 20 mT are shown in Figure F38. The effectiveness of demagnetizing such a magnetic component is clearly demonstrated in the inclination profile as a shifting of the inclination pattern to the shallower side (Fig. F38B). In contrast, no change in the declination profile between 0 and 176 mbsf implies that only vertical components were removed by 20 mT cleaning (Fig. F38A). Less drilling-induced magnetizations are observed below 176 mbsf. At this depth, the coring method changed from HPCS to EPCS, suggesting that the EPCS method resulted in less drilling-induced magnetization.

Based on the geocentric axial dipole model, the expected inclination at Site C0021 is 52°. After demagnetization at 20 mT, inclination profiles at 0–10, 80–100, and 126–136 mbsf agree well with this expected inclination value (Fig. F38B), which means that the magnetic directions in these intervals are reliable for the polarity interpretation and structural reorientation.

Inclination in the MTD A interval (94.16–116.75 mbsf) is broadly concentrated between 40° and 90°, whereas declination is widely scattered (Fig. F38). Just below the base of MTD A, declination and inclination show a more clustered distribution. Wider scattering of both inclination and declination is also observed in the MTD B interval (133.76–176.16 mbsf). A similar signature was reported for MTD 6 in Hole C0018A (Expedition 333 Scientists, 2012b). The scattering of paleomagnetic direction in MTDs A and B likely reflects internal deformation structures of MTDs.

Other than these intervals that show scattered paleomagnetic data, two other enigmatic intervals are rec-

ognized: (1) inclinations between 117 and 125 mbsf are systematically shallower, and (2) below the base of MTD B, declination and inclination scattering is observed. Currently, causes for these intervals are unknown.

Polarity

Above the top of MTD B, all inclinations show positive values. Referring to the age model in Hole C0018, it is interpreted that the sections above MTD B belong to the Brunhes Normal Polarity Chron, although no data were obtained from the interval between 5.93 and 80 mbsf (Fig. **F39**). A shift of polarity 5 m above MTD 6 in Hole C0018A, accompanied with tephra occurrence of Azuki ash (0.86 Ma) below, is interpreted to be the Brunhes/Matuyama boundary (0.78 Ma) (Fig. **F39A**). However, such a polarity shift is not recognized above MTD B in Hole C0021B, although MTD B is correlated with MTD 6 in Hole C0018A (see **"Core-log-seismic integration"**). One of the possible interpretations is that the sequence overlying MTD B is much younger than that above MTD 6 at Site C0018. The paleomagnetic directions below MTD B are expected to be similar to those below MTD 6 in Hole C0018A. However, the inclination and declination scattering does not allow us to discriminate the magnetic polarity pattern below MTD B.

Core-log-seismic integration

Site C0021 is located ~2 km northwest of Site C0018, where coring during Expedition 333 characterized the slope basin sedimentary succession as hemipelagic deposits comprising several MTDs (Expedition 333 Scientists, 2012b; Strasser et al., 2012). LWD and coring at Site C0021 during Expedition 338 aimed to further investigate the MTDs in a more proximal site with respect to the interpreted mass transport direction (Strasser et al., 2011) (Figs. **F3, F4, F40**). LWD data were collected in Hole C0021A from the seafloor to a TD of 294.0 mbsf, and cores were recovered from 0 to 5.9 and 80.0 to 194.5 mbsf in Hole C0021B. Because of operational time constraints, cores from Hole C0021B were not analyzed on board the ship during Expedition 338; they were analyzed during a shore-based core opening, description, and sampling party at the JAMSTEC KCC.

The Kumano 3-D prestack depth migration (PSDM) seismic volume (Moore et al., 2009) ties to Hole C0021A at the intersection of In-line 2269 and Cross-line 5094. The seismic data in this region are characterized by several packages of chaotic, low-amplitude reflectivity separated by moderate to high-amplitude negative polarity reflections, which are sometimes truncated in the updip direction (Strasser et al., 2011) (Fig. **F40**). Figure **F41** presents an overview of the correlation between LWD data and lithostratigraphy from Holes C0021A and C0021B, respectively, and seismic data.

According to seismic stratigraphic mapping and previous drilling and coring in the slope basin seaward of the megasplay fault zone (Screaton et al., 2009; Expedition 333 Scientists, 2012b; Kimura et al., 2011; Strasser et al., 2011), a single unit was defined from analysis of both core samples and LWD data (Unit I [slope basin]; see **"Lithology"** and **"Logging while drilling"**). Two lithologic subunits were identified based on core data, whereas three subunits were identified from the LWD data (Fig. **F41**).

Lithologic Subunit IA is composed of mottled greenish gray silty clay with local thin interbeds of fine sand and ash layers. Subunit IB is composed of a succession of thin sand beds interbedded with silty clay and local ash layers. The Subunit IA/IB boundary is defined in cores at 176.16 mbsf as the first downhole occurrence of repeating sand beds with spacing of 20–30 cm. This boundary correlates to the logging Subunit IA/IB boundary, characterized by a change in the resistivity log character (lower to higher amplitude variability above and below, respectively). This boundary also reflects an abrupt change in bedding dip between an overlying well-defined zone of high-angle bedding, observed in resistivity images (see **"Logging while drilling"**) and measured in cores (see **"Structural geology"**), and an interval of predominantly low to moderately dipping bedding planes below. In the seismic data, this boundary correlates to a low amplitude, positive reflection within the uppermost part of seismic Subunit 1b (Strasser et al., 2011). Below this reflection, and within seismic Subunit 1b, a more prominent high-amplitude negative polarity reflection is observed at ~205 mbsf, which may correspond to a distinct ~35 gAPI decrease in the gamma ray curve, as well as a local minimum in resistivity (Fig. **F41**).

Within lithologic Subunit IA, two MTD intervals have been identified in Hole C0021B cores based on the occurrence of mud clasts, chaotic bedding, and steeply dipping beds (see **"Lithology"**); an increase in shear strength and a decrease in porosity (see **"Physical properties"**); and the occurrence of shear zones/faults (see **"Structural geology"**) (MTD A: 94.16–116.57 mbsf; MTD B: 133.76–176.16 mbsf [see **"Lithology"**]). Distinct log character in the lower part of logging Subunit IA (144.0–176.8 mbsf) appears to correlate to MTD B (Fig. **F41**), which also matches a zone of low-amplitude reflectivity observed in the seismic data at this interval and is inferred to represent a large, regional MTD (Strasser et

al., 2011). The top of MTD B is defined in the cores by a thin cogenetic turbidite overlying chaotic bedding intervals containing mud clasts. This boundary may correlate to the logging data at ~144 mbsf, characterized by a slight downsection increase in both resistivity and natural gamma ray values. This boundary appears to tie to a prominent reflection in the seismic data (Figs. **F40, F41**).

In logging data, moderate to high bedding dip angles are also present between 97 and 130 mbsf, but these are more variable, within a larger range (20°–75°). The top part of this interval appears to correlate with MTD A identified in cores from Hole C0021B and also matches the chaotic, low-reflective character of the seismic data in this interval (Fig. **F41**).

The equivalent depth of the logging Subunit IB/IC boundary, defined by a distinct drop in resistivity values and a change in the resistivity log character (from higher to lower amplitude variability above and below, respectively), has not been cored. This boundary, however, appears to correlate with a high-amplitude, negative polarity reflection observed at ~280 mbsf and may reflect the transition from seismic Subunit 1b (sand-rich slope basin) to seismic Subunit 1c (lower slope basin) (Strasser et al., 2011).

Comparison with Site C0018

Site C0021 is located ~2 km northwest of Site C0018 and is situated in an upslope position, closer to the scarp surface for the MTDs (Strasser et al., 2011, 2012). Based on the spatial coverage of the MTDs predicted from the seismic data, it should be possible to correlate events between the two sites. MTD A identified in Hole C0021B and the upper zone with chaotic bedding observed in Hole C0021A does not have the same characteristics as MTD A identified from structural analysis of the resistivity image data in Hole C0018B (see **"Logging while drilling"** and **"Core-log-seismic integration,"** both in the "Site C0018" chapter [Strasser et al., 2014c]), which was postulated to correspond to several of the smaller MTDs observed in Hole C0018A cores (see **"Core-log-seismic integration"** in the "Site C0018" chapter [Strasser et al., 2014c]; Expedition 333 Scientists, 2012b). The mismatch between the upper sections of these sites is corroborated by the seismic data (Fig. **F40**), which show that the package of low reflectivity at the corresponding depth at Site C0021 is truncated to the southeast and does not extend to Site C0018.

In contrast, core observation and analyses of MTD B in Hole C0021B and the character of the MTD B correlative interval in the logging data (144–176.8 mbsf in Hole C0021A) is very similar to MTD 6 of Hole C0018A and correlative to the logging interval between 103 and 170 mbsf in Hole C0018B (Fig. **F40**). This MTD has been traced throughout the Kumano 3-D seismic volume (Strasser et al., 2011, 2012). The base of the MTD does not remain within the same stratigraphic horizon and suggests that the processes associated with MTD emplacement at Site C0021 eroded deeper into the underlying strata than at Site C0018. The reflection defining the top of the MTD, in contrast, is well correlated throughout the seismic data set. Using seismic stratigraphy and bio-, magneto-, and tephra-stratigraphic age constraints from Site C0018, this MTD is inferred to have emplaced between 1.05 and 0.85 Ma (Strasser et al., 2012).

References

Archie, G.E., 1947. Electrical resistivity—an aid in core analysis interpretation. *AAPG Bull.,* 31(2):350–366.

Bernard, B.B., Brooks, J.M., and Sackett, W.M., 1978. Light hydrocarbons in recent Texas continental shelf and slope sediments. *J. Geophys. Res.: Oceans,* 83(C8):4053–4061. **doi:10.1029/JC083iC08p04053**

Byrne, T.B., Lin, W., Tsutsumi, A., Yamamoto, Y., Lewis, J.C., Kanagawa, K., Kitamura, Y., Yamaguchi, A., and Kimura, G., 2009. Anelastic strain recovery reveals extension across SW Japan subduction zone. *Geophys. Res. Lett.,* 36(23):L23310. **doi:10.1029/2009GL040749**

Chang, C., McNeill, L.C., Moore, J.C., Lin, W., Conin, M., and Yamada, Y., 2010. In situ stress state in the Nankai accretionary wedge estimated from borehole wall failures. *Geochem., Geophys., Geosyst.,* 11:Q0AD04. **doi:10.1029/2010GC003261**

Expedition 314 Scientists, 2009. Expedition 314 Site C0002. *In* Kinoshita, M., Tobin, H., Ashi, J., Kimura, G., Lallemant, S., Screaton, E.J., Curewitz, D., Masago, H., Moe, K.T., and the Expedition 314/315/316 Scientists, *Proc. IODP,* 314/315/316: Washington, DC (Integrated Ocean Drilling Program Management International, Inc.). **doi:10.2204/iodp.proc.314315316.114.2009**

Expedition 316 Scientists, 2009a. Expedition 316 Site C0004. *In* Kinoshita, M., Tobin, H., Ashi, J., Kimura, G., Lallemant, S., Screaton, E.J., Curewitz, D., Masago, H., Moe, K.T., and the Expedition 314/315/316 Scientists, *Proc. IODP,* 314/315/316: Washington, DC (Integrated Ocean Drilling Program Management International, Inc.). **doi:10.2204/iodp.proc.314315316.133.2009**

Expedition 316 Scientists, 2009b. Expedition 316 Site C0008. *In* Kinoshita, M., Tobin, H., Ashi, J., Kimura, G., Lallemant, S., Screaton, E.J., Curewitz, D., Masago, H., Moe, K.T., and the Expedition 314/315/316 Scientists, *Proc. IODP,* 314/315/316: Washington, DC (Integrated Ocean Drilling Program Management International, Inc.). **doi:10.2204/iodp.proc.314315316.136.2009**

Expedition 333 Scientists, 2011. NanTroSEIZE Stage 2: subduction inputs 2 and heat flow. *IODP Prel. Rept.,* 333. **doi:10.2204/iodp.pr.333.2011**

Expedition 333 Scientists, 2012a. Expedition 333 summary. *In* Henry, P., Kanamatsu, T., Moe, K., and the

Expedition 333 Scientists, *Proc. IODP,* 333: Tokyo (Integrated Ocean Drilling Program Management International, Inc.). **doi:10.2204/iodp.proc.333.101.2012**

Expedition 333 Scientists, 2012b. Site C0018. *In* Henry, P., Kanamatsu, T., Moe, K., and the Expedition 333 Scientists, *Proc. IODP,* 333: Tokyo (Integrated Ocean Drilling Program Management International, Inc.). **doi:10.2204/iodp.proc.333.103.2012**

Fuerstenau, D.W., Manmohan, D., and Raghavan, S., 1981. The adsorption of alkaline-earth metal ions at the rutile/aqueous solution interface. *In* Tewari, P.H. (Ed.), *Adsorption From Aqueous Solutions:* New York (Plenum Press), 93–117. **doi:10.1007/978-1-4613-3264-0_5**

Gee, J., Staudigel, H., and Tauxe, L., 1989. Contribution of induced magnetization to magnetization of seamounts. *Nature (London, U. K.),* 342(6246):170–173. **doi:10.1038/342170a0**

Heki, K., 2007. Secular, transient, and seasonal crustal movements in Japan from a dense GPS array: implication for plate dynamics in convergent boundaries. *In* Dixon, T.H., and Moore, J.C. (Eds.), *The Seismogenic Zone of Subduction Thrust Faults:* New York (Columbia Univ. Press), 512–539.

Ienaga, M., McNeill, L.C., Mikada, H., Saito, S., Goldberg, D., and Moore, J.C., 2006. Borehole image analysis of the Nankai accretionary wedge, ODP Leg 196: structural and stress studies. *Tectonophysics,* 426(1–2):207–220. **doi:10.1016/j.tecto.2006.02.018**

Kimura, G., Moore, G.F., Strasser, M., Screaton, E., Curewitz, D., Streiff, C., and Tobin, H., 2011. Spatial and temporal evolution of the megasplay fault in the Nankai Trough. *Geochem., Geophys., Geosyst.,* 12(3):Q0A008. **doi:10.1029/2010GC003335**

Kinoshita, M., Tobin, H., Moe, K.T., and the Expedition 314 Scientists, 2008. NanTroSEIZE Stage 1A: NanTroSEIZE LWD transect. *IODP Prel. Rept.,* 314. **doi:10.2204/iodp.pr.314.2008**

Lin, W., Doan, M.-L., Moore, J.C., McNeill, L., Byrne, T.B., Ito, T., Saffer, D., Conin, M., Kinoshita, M., Sanada, Y., Moe, K.T., Araki, E., Tobin, H., Boutt, D., Kano, Y., Hayman, N.W., Flemings, P., Huftile, G.J., Cukur, D., Buret, C., Schleicher, A.M., Efimenko, N., Kawabata, K., Buchs, D.M., Jiang, S., Kameo, K., Horiguchi, K., Wiersberg, T., Kopf, A., Kitada, K., Eguchi, N., Toczko, S., Takahashi, K., and Kido, Y., 2010. Present-day principal horizontal stress orientations in the Kumano forearc basin of the southwest Japan subduction zone determined from IODP NanTroSEIZE drilling Site C0009. *Geophys. Res. Lett.,* 37(13):L13303. **doi:10.1029/2010GL043158**

McNeill, L.C., Ienaga, M., Tobin, H., Saito, S., Goldberg, D., Moore, J.C., and Mikada, H., 2004. Deformation and in situ stress in the Nankai accretionary prism from resistivity-at-bit images, ODP Leg 196. *Geophys. Res. Lett.,* 31(2):L02602. **doi:10.1029/2003GL018799**

Meyers, P.A., 1997. Organic geochemical proxies of paleoceanographic, paleolimnologic, and paleoclimatic processes. *Org. Geochem.,* 27(5–6):213–250. **doi:10.1016/S0146-6380(97)00049-1**

Moore, G.F., Park, J.-O., Bangs, N.L., Gulick, S.P., Tobin, H.J., Nakamura, Y., Sato, S., Tsuji, T., Yoro, T., Tanaka, H., Uraki, S., Kido, Y., Sanada, Y., Kuramoto, S., and Taira, A., 2009. Structural and seismic stratigraphic framework of the NanTroSEIZE Stage 1 transect. *In* Kinoshita, M., Tobin, H., Ashi, J., Kimura, G., Lallemant, S., Screaton, E.J., Curewitz, D., Masago, H., Moe, K.T., and the Expedition 314/315/316 Scientists, *Proc. IODP,* 314/315/316: Washington, DC (Integrated Ocean Drilling Program Management International, Inc.). **doi:10.2204/iodp.proc.314315316.102.2009**

Piasecki, W., Zarzycki, P., and Charmas, R., 2010. Adsorption of alkali metal cations and halide anions on metal oxides: prediction of Hofmeister series using 1-pK triple layer model. *Adsorption,* 16(4–5):295–303. **doi:10.1007/s10450-010-9245-y**

Screaton, E.J., Kimura, G., Curewitz, D., and the Expedition 316 Scientists, 2009. Expedition 316 summary. *In* Kinoshita, M., Tobin, H., Ashi, J., Kimura, G., Lallemant, S., Screaton, E.J., Curewitz, D., Masago, H., Moe, K.T., and the Expedition 314/315/316 Scientists, *Proc. IODP,* 314/315/316: Washington, DC (Integrated Ocean Drilling Program Management International, Inc.). **doi:10.2204/iodp.proc.314315316.131.2009**

Seno, T., Stein, S., and Gripp, A.E., 1993. A model for the motion of the Philippine Sea plate consistent with NUVEL-1 and geological data. *J. Geophys. Res.: Solid Earth,* 98(B10):17941–17948. **doi:10.1029/93JB00782**

Strasser, M., Dugan, B., Kanagawa, K., Moore, G.F., Toczko, S., Maeda, L., Kido, Y., Moe, K.T., Sanada, Y., Esteban, L., Fabbri, O., Geersen, J., Hammerschmidt, S., Hayashi, H., Heirman, K., Hüpers, A., Jurado Rodriguez, M.J., Kameo, K., Kanamatsu, T., Kitajima, H., Masuda, H., Milliken, K., Mishra, R., Motoyama, I., Olcott, K., Oohashi, K., Pickering, K.T., Ramirez, S.G., Rashid, H., Sawyer, D., Schleicher, A., Shan, Y., Skarbek, R., Song, I., Takeshita, T., Toki, T., Tudge, J., Webb, S., Wilson, D.J., Wu, H.-Y., and Yamaguchi, A., 2014a. Methods. *In* Strasser, M., Dugan, B., Kanagawa, K., Moore, G.F., Toczko, S., Maeda, L., and the Expedition 338 Scientists, *Proc. IODP,* 338: Yokohama (Integrated Ocean Drilling Program). **doi:10.2204/iodp.proc.338.102.2014**

Strasser, M., Dugan, B., Kanagawa, K., Moore, G.F., Toczko, S., Maeda, L., Kido, Y., Moe, K.T., Sanada, Y., Esteban, L., Fabbri, O., Geersen, J., Hammerschmidt, S., Hayashi, H., Heirman, K., Hüpers, A., Jurado Rodriguez, M.J., Kameo, K., Kanamatsu, T., Kitajima, H., Masuda, H., Milliken, K., Mishra, R., Motoyama, I., Olcott, K., Oohashi, K., Pickering, K.T., Ramirez, S.G., Rashid, H., Sawyer, D., Schleicher, A., Shan, Y., Skarbek, R., Song, I., Takeshita, T., Toki, T., Tudge, J., Webb, S., Wilson, D.J., Wu, H.-Y., and Yamaguchi, A., 2014b. Site C0002. *In* Strasser, M., Dugan, B., Kanagawa, K., Moore, G.F., Toczko, S., Maeda, L., and the Expedition 338 Scientists, *Proc. IODP,* 338: Yokohama (Integrated Ocean Drilling Program). **doi:10.2204/iodp.proc.338.103.2014**

Strasser, M., Dugan, B., Kanagawa, K., Moore, G.F., Toczko, S., Maeda, L., Kido, Y., Moe, K.T., Sanada, Y., Esteban, L., Fabbri, O., Geersen, J., Hammerschmidt, S., Hayashi, H., Heirman, K., Hüpers, A., Jurado Rodriguez, M.J., Kameo, K., Kanamatsu, T., Kitajima, H., Masuda, H., Milliken, K., Mishra, R., Motoyama, I., Olcott, K., Oohashi, K.,

Pickering, K.T., Ramirez, S.G., Rashid, H., Sawyer, D., Schleicher, A., Shan, Y., Skarbek, R., Song, I., Takeshita, T., Toki, T., Tudge, J., Webb, S., Wilson, D.J., Wu, H.-Y., and Yamaguchi, A., 2014c. Site C0018. *In* Strasser, M., Dugan, B., Kanagawa, K., Moore, G.F., Toczko, S., Maeda, L., and the Expedition 338 Scientists, *Proc. IODP,* 338: Yokohama (Integrated Ocean Drilling Program). **doi:10.2204/iodp.proc.338.105.2014**

Strasser, M., Dugan, B., Kanagawa, K., Moore, G.F., Toczko, S., Maeda, L., Kido, Y., Moe, K.T., Sanada, Y., Esteban, L., Fabbri, O., Geersen, J., Hammerschmidt, S., Hayashi, H., Heirman, K., Hüpers, A., Jurado Rodriguez, M.J., Kameo, K., Kanamatsu, T., Kitajima, H., Masuda, H., Milliken, K., Mishra, R., Motoyama, I., Olcott, K., Oohashi, K., Pickering, K.T., Ramirez, S.G., Rashid, H., Sawyer, D., Schleicher, A., Shan, Y., Skarbek, R., Song, I., Takeshita, T., Toki, T., Tudge, J., Webb, S., Wilson, D.J., Wu, H.-Y., and Yamaguchi, A., 2014d. Site C0022. *In* Strasser, M., Dugan, B., Kanagawa, K., Moore, G.F., Toczko, S., Maeda, L., and the Expedition 338 Scientists, *Proc. IODP,* 338: Yokohama (Integrated Ocean Drilling Program). **doi:10.2204/iodp.proc.338.107.2014**

Strasser, M., Henry, P., Kanamatsu, T., Moe, K.T., Moore, G.F., and the IODP Expedition 333 Scientists, 2012. Scientific drilling of mass-transport deposits in the Nankai accretionary wedge: first results from IODP Expedition 333. *In* Yamada, Y., Kawamura, K., Ikehara, K., Ogawa, Y., Urgeles, R., Mosher, D., Chaytor, J., and Strasser, M. (Eds.), *Submarine Mass Movements and Their Consequences*. Adv. Nat. Technol. Hazard Res., 31(8):671–681. **doi:10.1007/978-94-007-2162-3_60**

Strasser, M., Moore, G.F., Kimura, G., Kitamura, Y., Kopf, A.J., Lallemant, S., Park, J.-O., Screaton, E.J., Su, X., Underwood, M.B., and Zhao, X., 2009. Origin and evolution of a splay fault in the Nankai accretionary wedge. *Nat. Geosci.,* 2(9):648–652. **doi:10.1038/ngeo609**

Strasser, M., Moore, G.F., Kimura, G., Kopf, A.J., Underwood, M.B., Guo, J., and Screaton, E.J., 2011. Slumping and mass-transport deposition in the Nankai forearc: evidence from IODP drilling and 3-D reflection seismic data. *Geochem., Geophys., Geosyst.,* 12:Q0AD13. **doi:10.1029/2010GC003431**

Publication: 13 January 2014
MS 338-106

Figure F1. Regional location map showing Site C0021 in context of the NanTroSEIZE project sites. Box = region with 3-D seismic data, red = Expedition 338 sites, blue = NanTroSEIZE Stage 1 and 2 sites, yellow arrows = estimated far-field vectors between Philippine Sea plate and Japan (Seno et al., 1993; Heki, 2007), stars = locations of 1944 and 1946 tsunamigenic earthquakes.

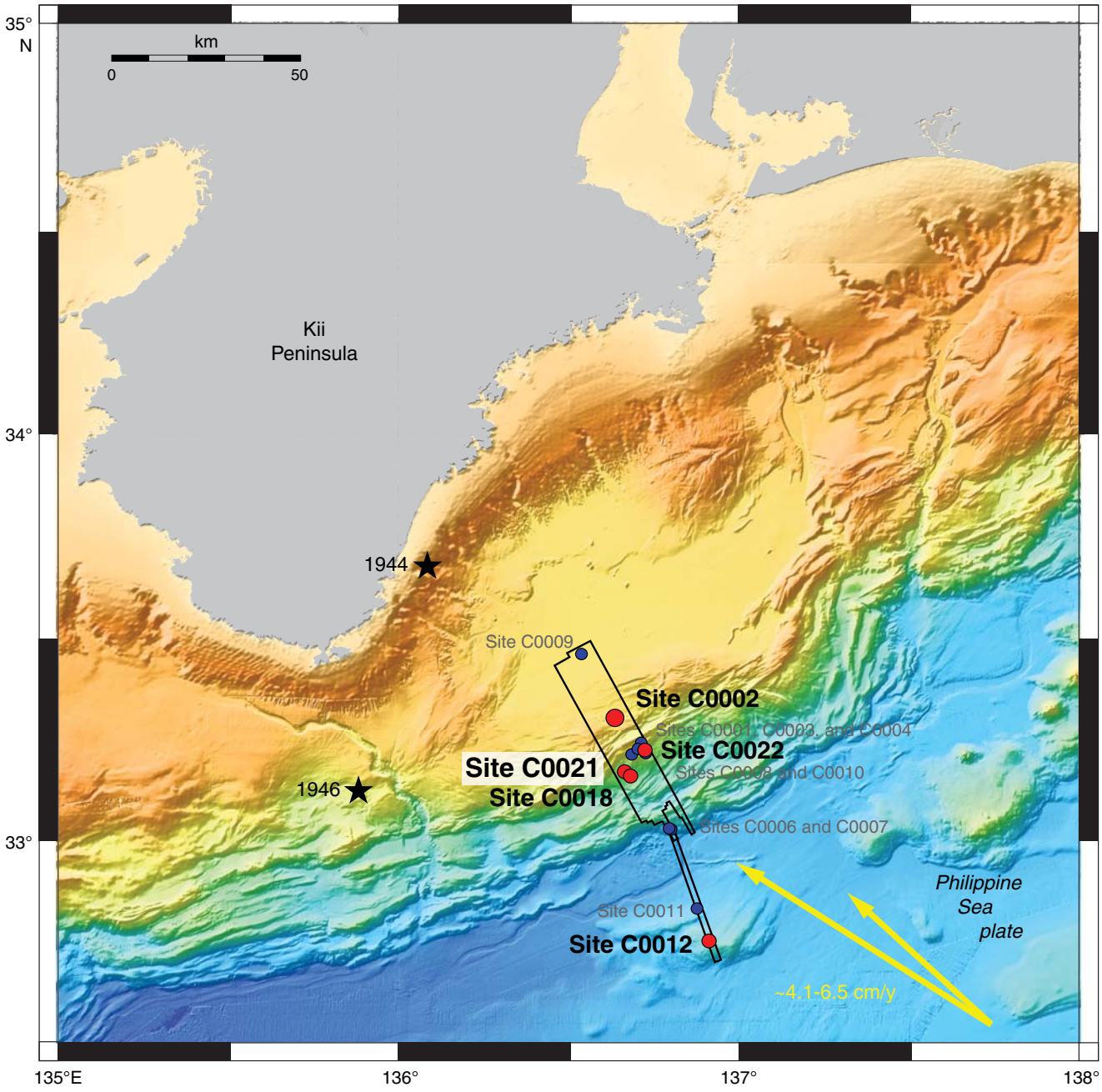

Figure F2. Detailed bathymetry and structure of the slope basin at the footwall of the splay fault (Strasser et al., 2011), showing location of Site C0021 relative to other Expedition 338 sites (red) and NanTroSEIZE Stage 1 and 2 sites. Solid black lines = locations of seismic lines A–A′ in Figure F3 and seismic lines B–B′ and C–C′ in Figure F4. MTD = mass transport deposit, IL = in-line, XL = cross-line.

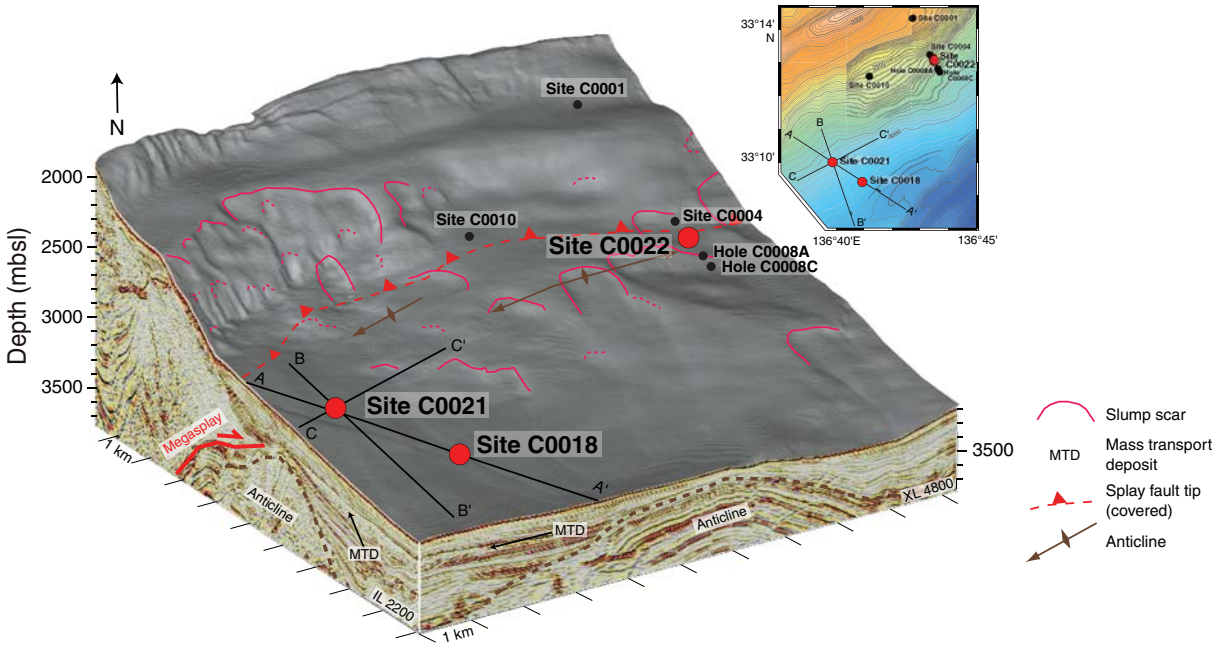

Figure F3. Arbitrary seismic line A–A′ through Sites C0018 and C0021. Location shown in Figure F2. VE = vertical exaggeration.

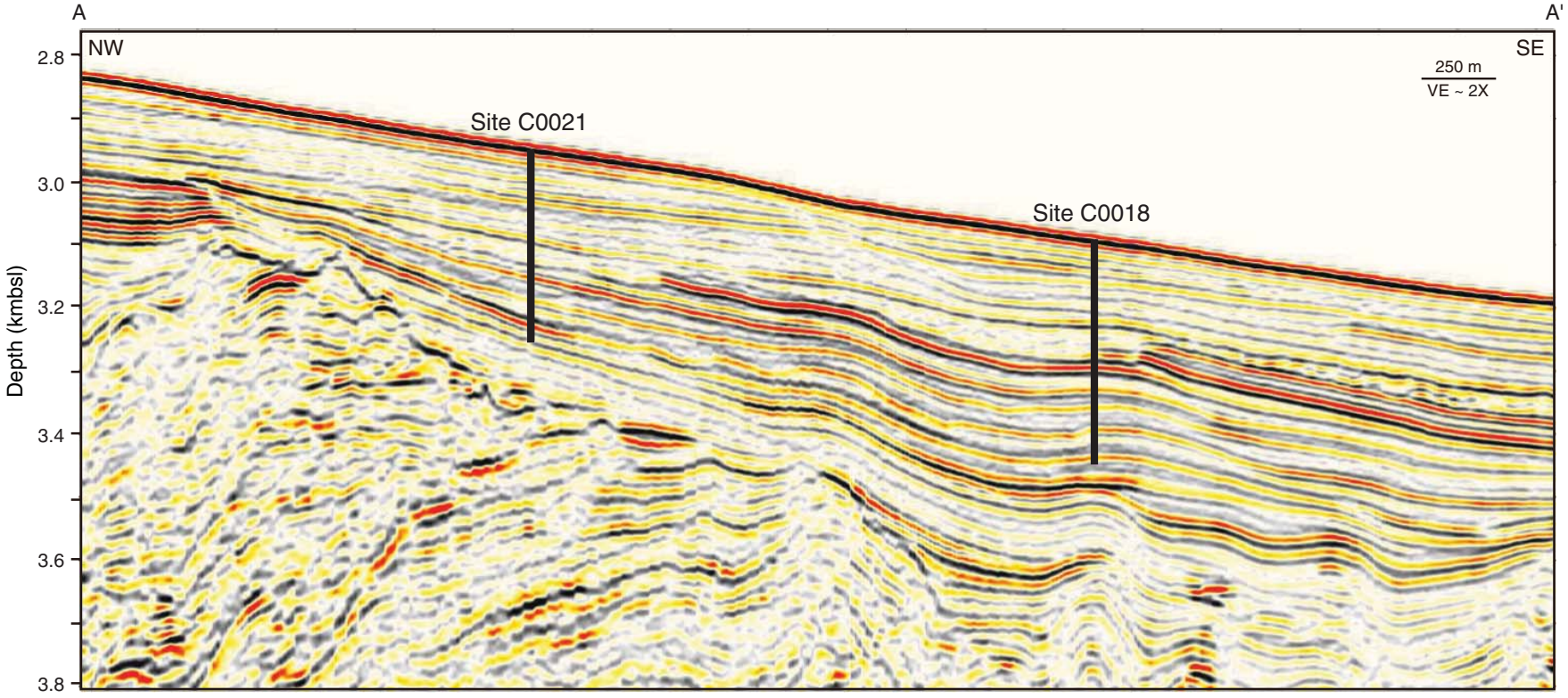

Figure F4. Seismic lines crossing Site C0021 showing locations of mass transport deposits (MTDs). Upper line is In-line (IL) 2269, lower line is Cross-line (XL) 5094. Thick line represents the extent of coring in Hole C0021B, and the thinner gray extension represents the extent of LWD in Hole C0021A. Locations shown in Figure F2. VE = vertical exaggeration.

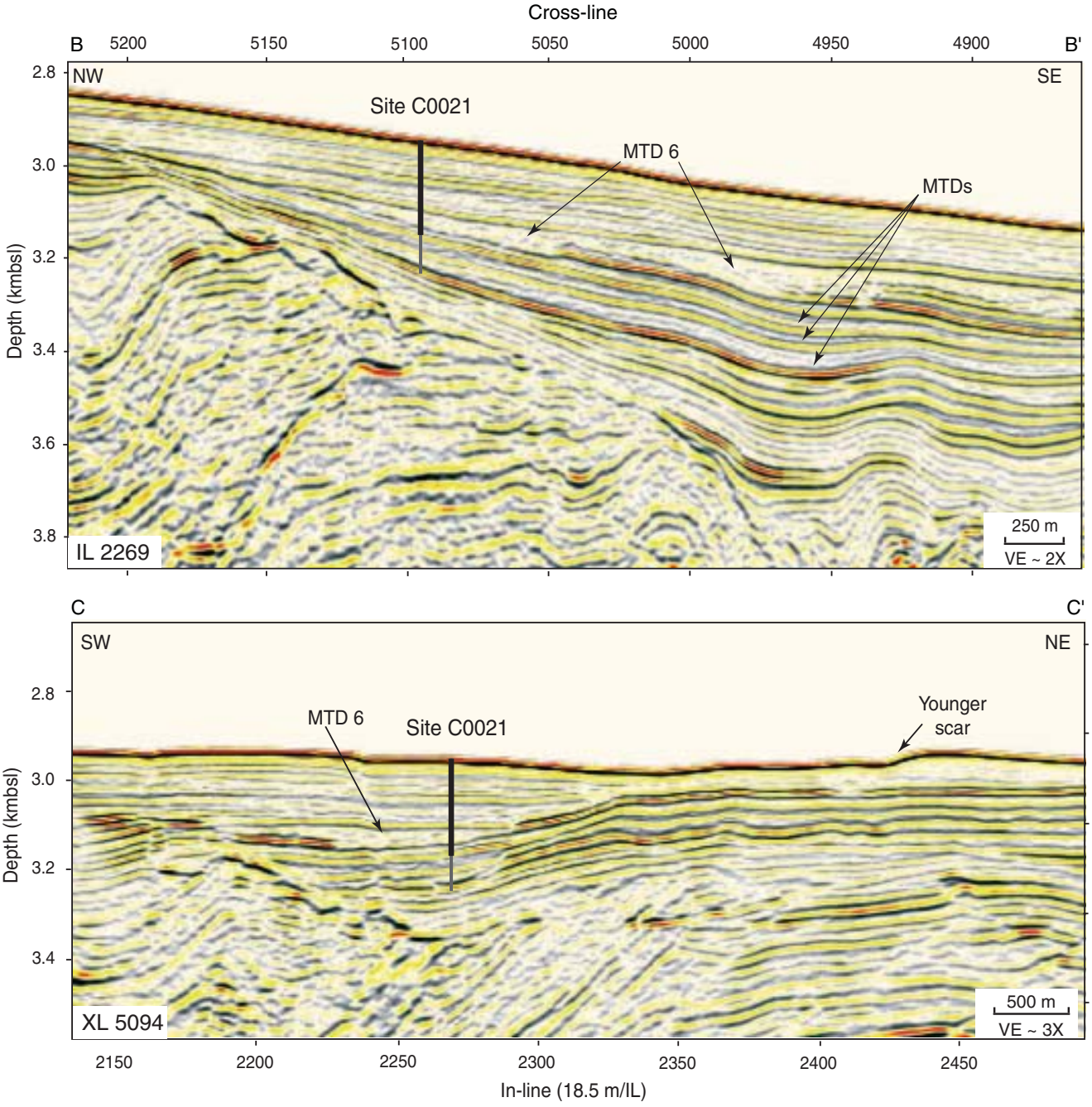

Figure F5. Overview composite plot of LWD data and deep resistivity image for Hole C0021A, with logging subunits, resistivity-derived porosity (red = Expedition 314 Archie parameters a = 1, m = 2.4; blue = Archie parameters as used for Hole C0018A; see **"Logging while drilling"** in the "Site C0018" chapter [Strasser et al., 2014c]) and bulk density, and bedding and fracture dips and dip directions.

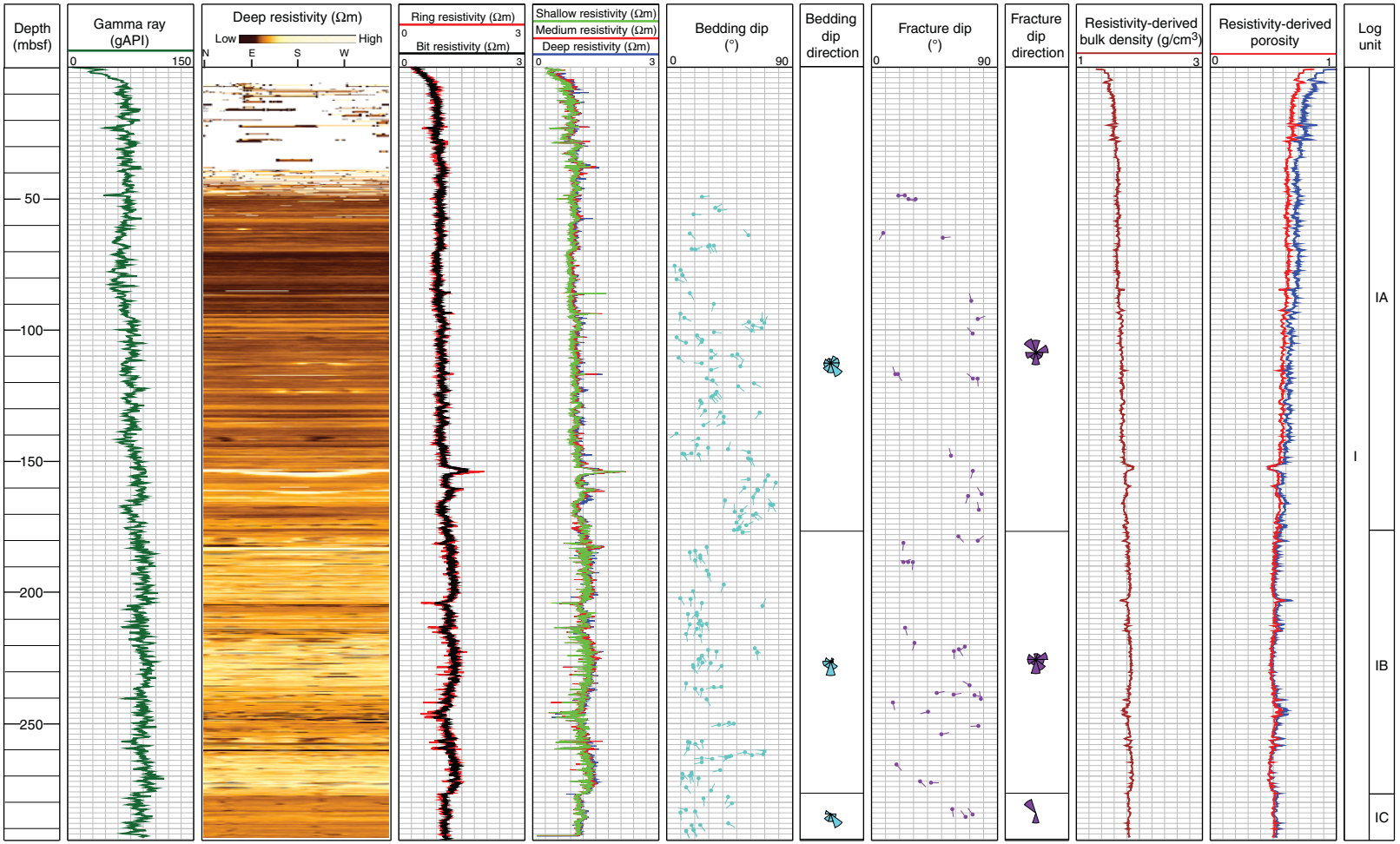

Figure F6. Composite plot of LWD gamma ray and resistivity data in Hole C0021A, with subunits and observed log trends highlighted. Black arrows = overall trends, red arrows = points of prominent high and low spikes.

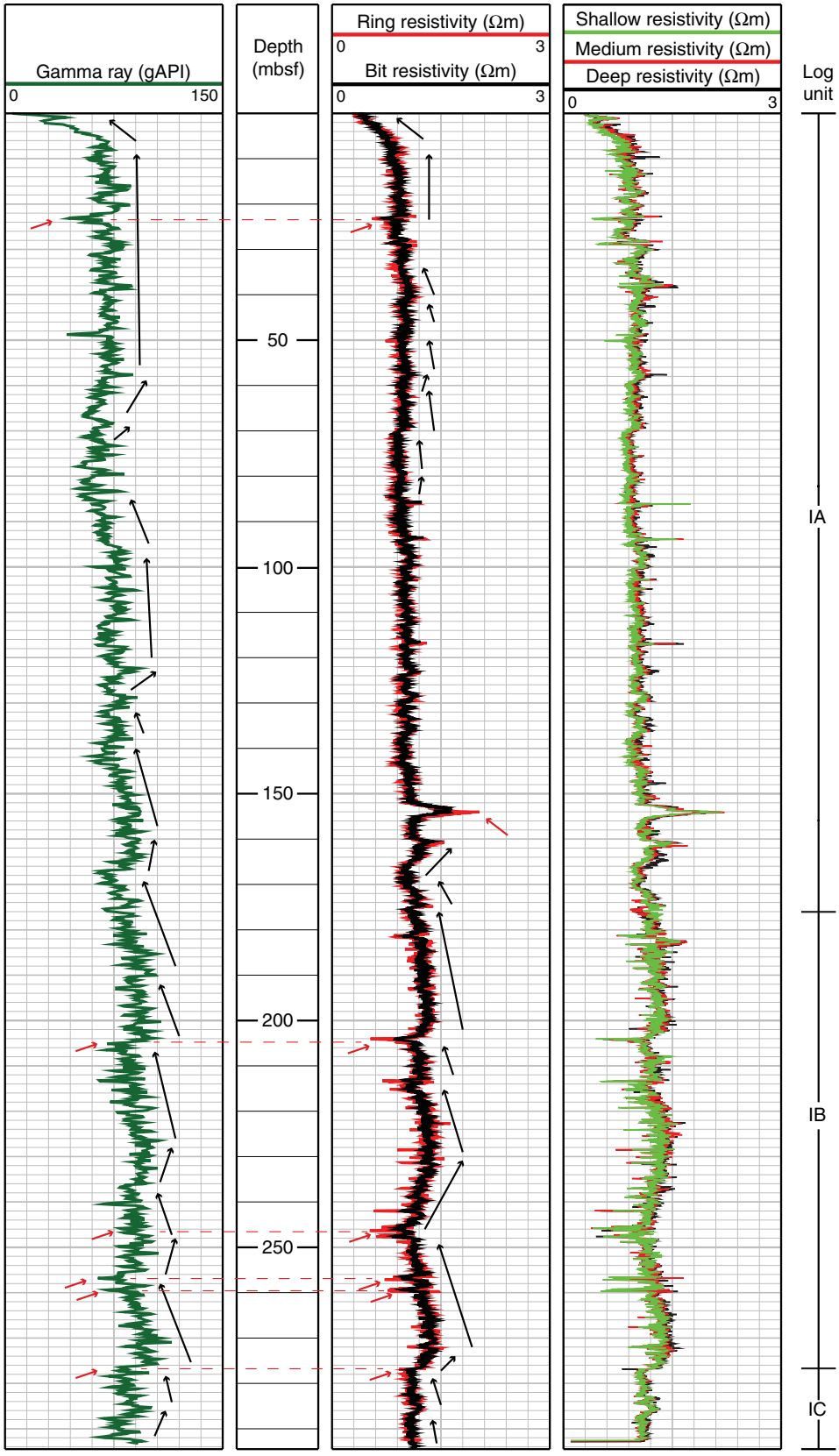

Figure F7. Stereonets and rose diagrams of the dip and azimuth of bedding and fractures, Hole C0021A. Stereonets are lower hemisphere projections plotting the poles to the planes.

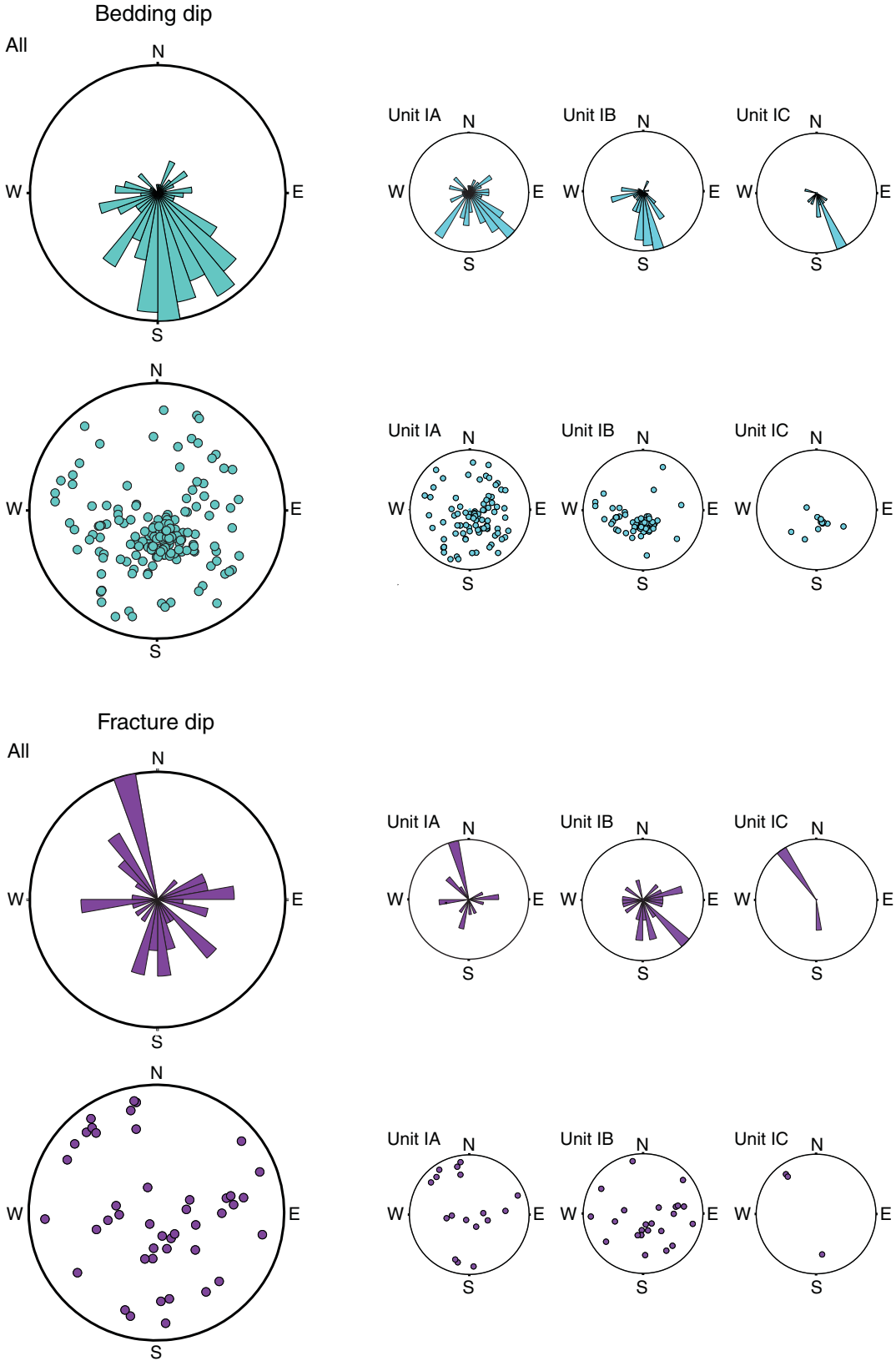

Figure F8. Prominent observations in the resistivity images of slope sediments in Hole C0021A. All images are plotted with a low-range resistivity scale (0.5–1.5 Ωm). **A.** Rapid change in dip direction observed in the upper interval of chaotic, high-angle bedding. **B.** Lower interval of high-angle bedding shows more gradational changes in dip direction, often separated by mottled, low-resistivity fractures. **C.** Patches of low resistivity are often observed in conjunction with low-resistivity beds or fractures.

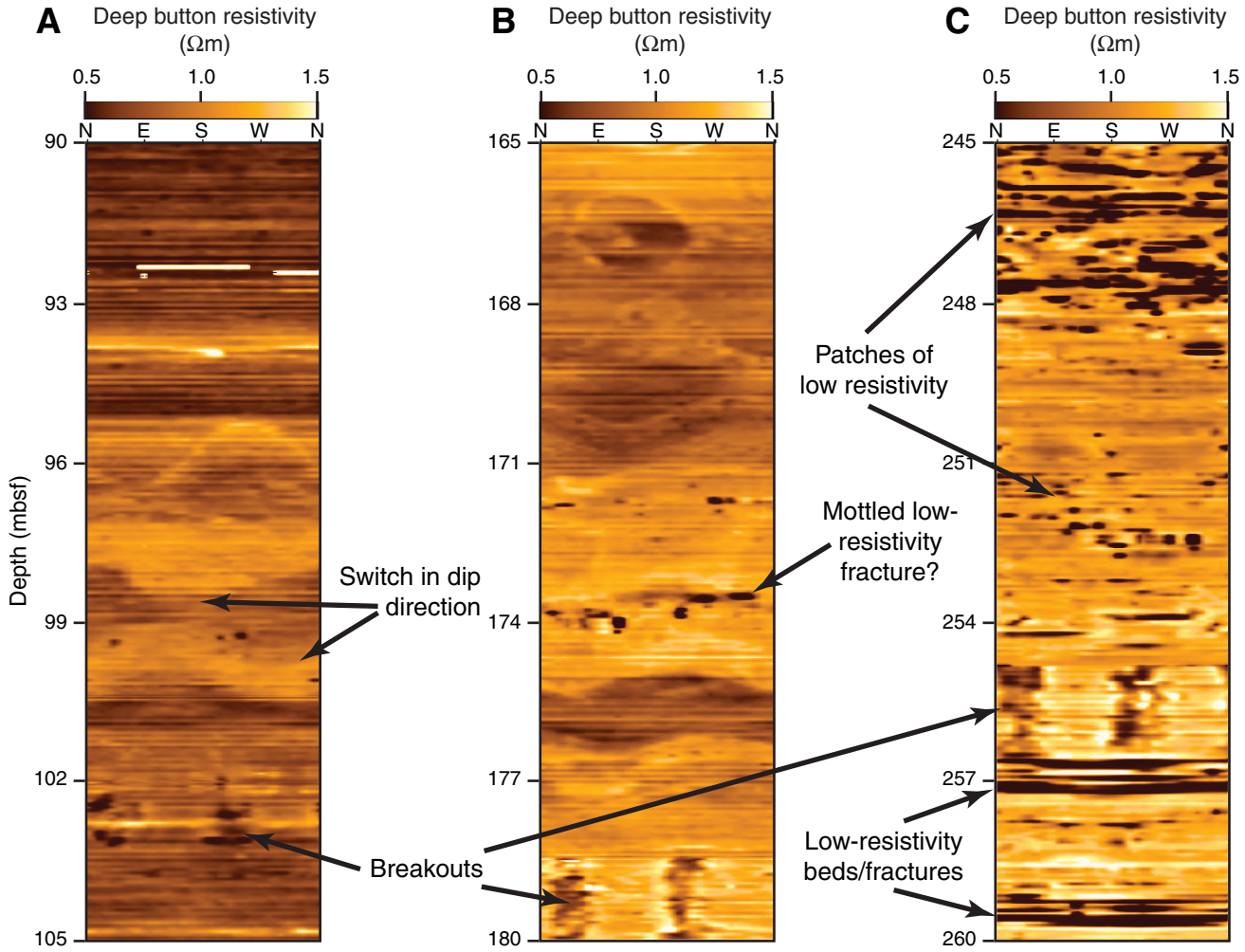

Figure F9. Lithologic column, Hole C0021B. MTD = mass transport deposit.

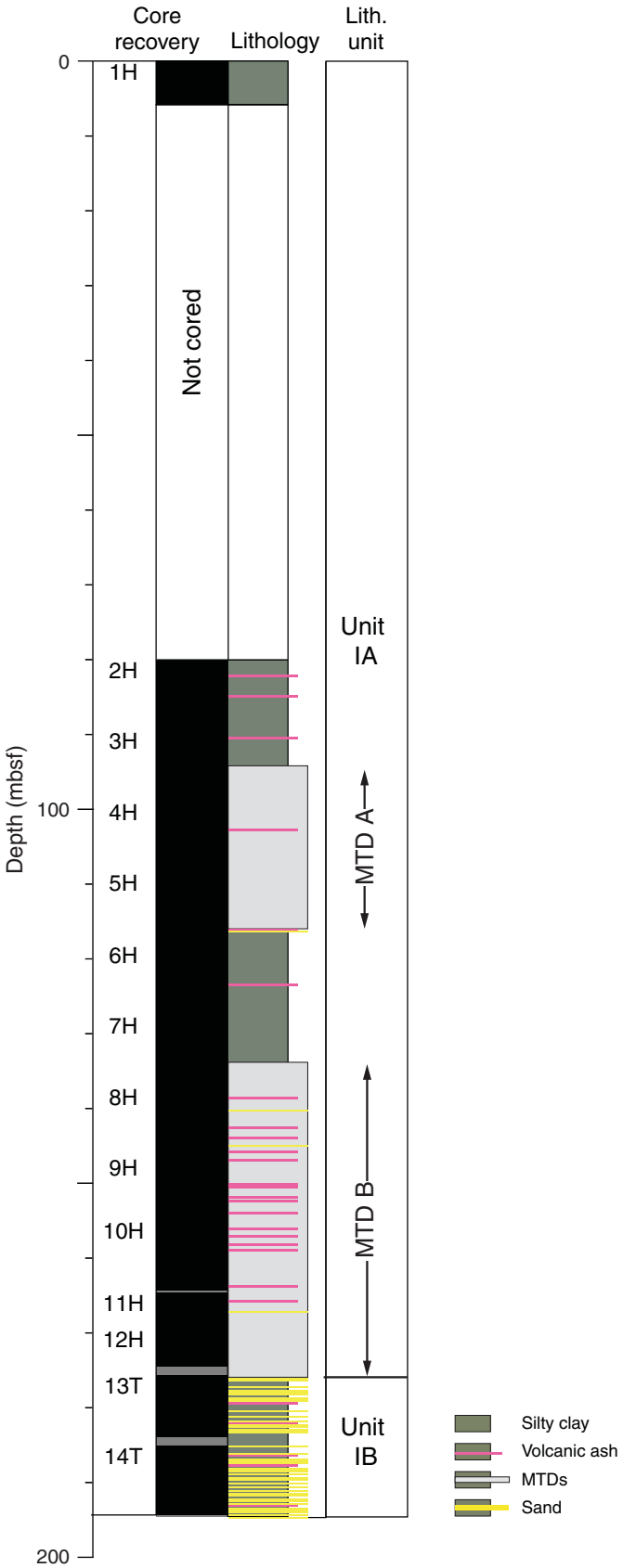

Figure F10. Sand and ash layer thickness versus depth, Hole C0021B.

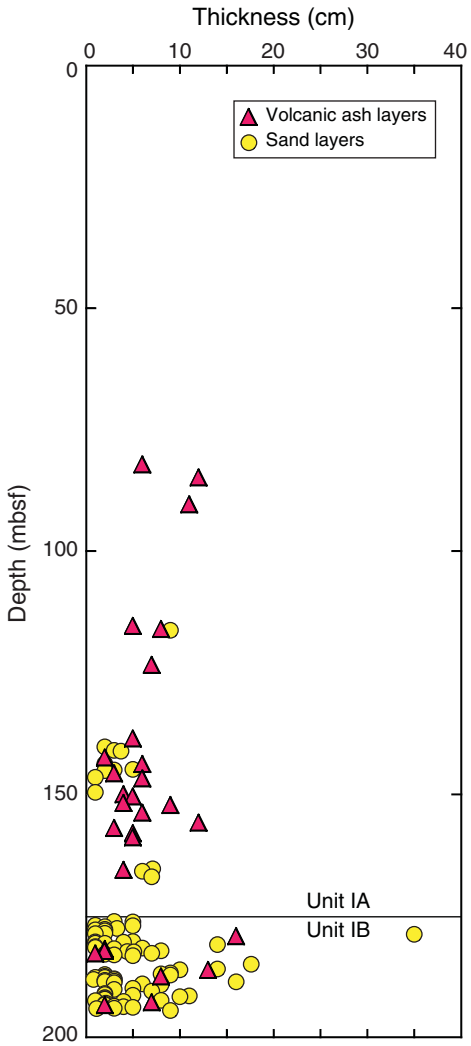

Figure F11. Characteristic lithologic features of Subunits IA and IB, Hole C0021B. **A.** Subunit IA (slope basin). Core photograph showing ash layer overlying greenish gray silty clay and smear slide close-up photographs in plane-polarized and cross-polarized light. **B.** Subunit IB (sand-rich slope basin). Core photograph showing representative sand layer overlying silty clay and smear slide close-up photographs in plane-polarized and cross-polarized light.

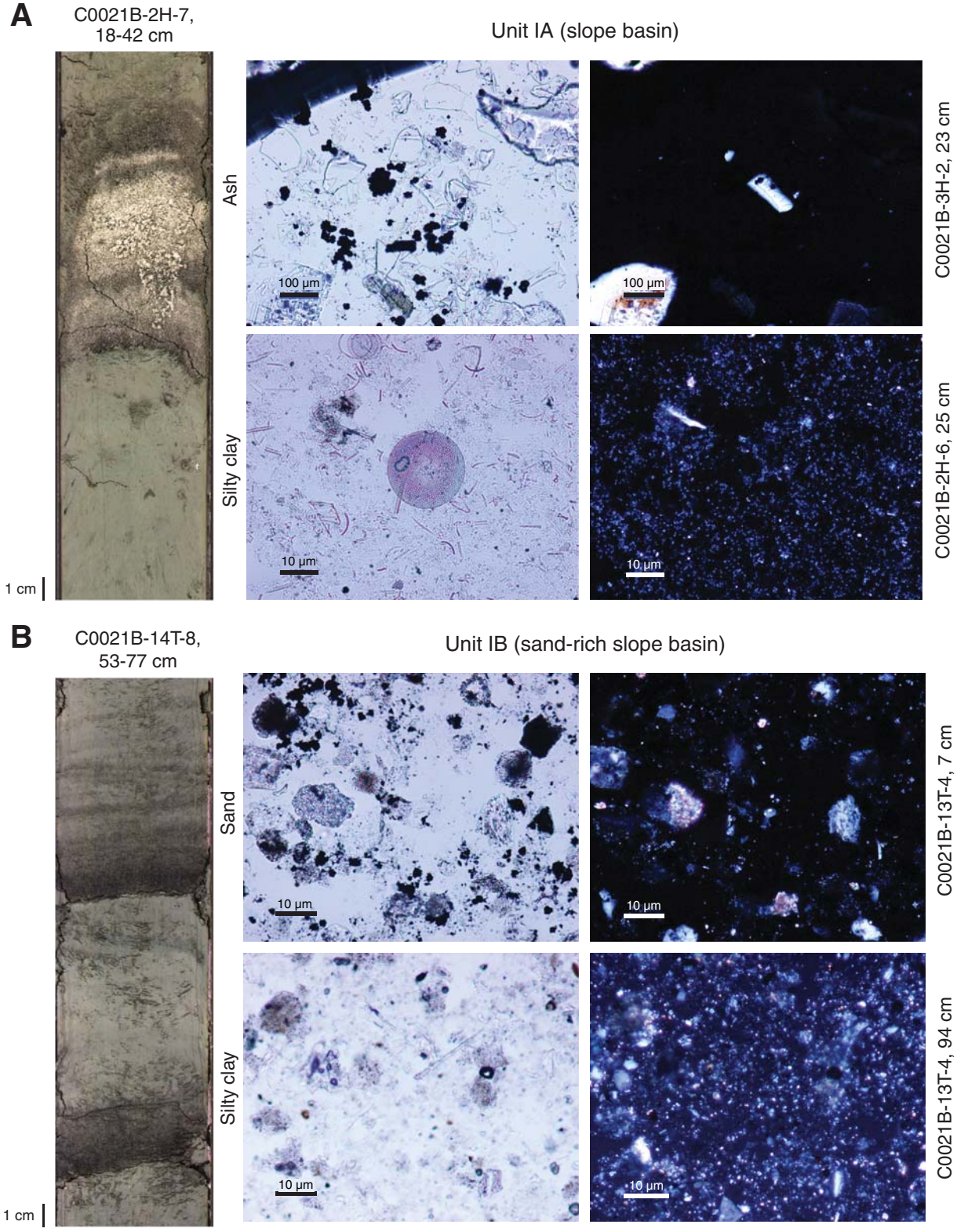

Figure F12. Depth profile of XRD bulk mineral composition data, Hole C0021B. Fsp = feldspar, Qtz = quartz.

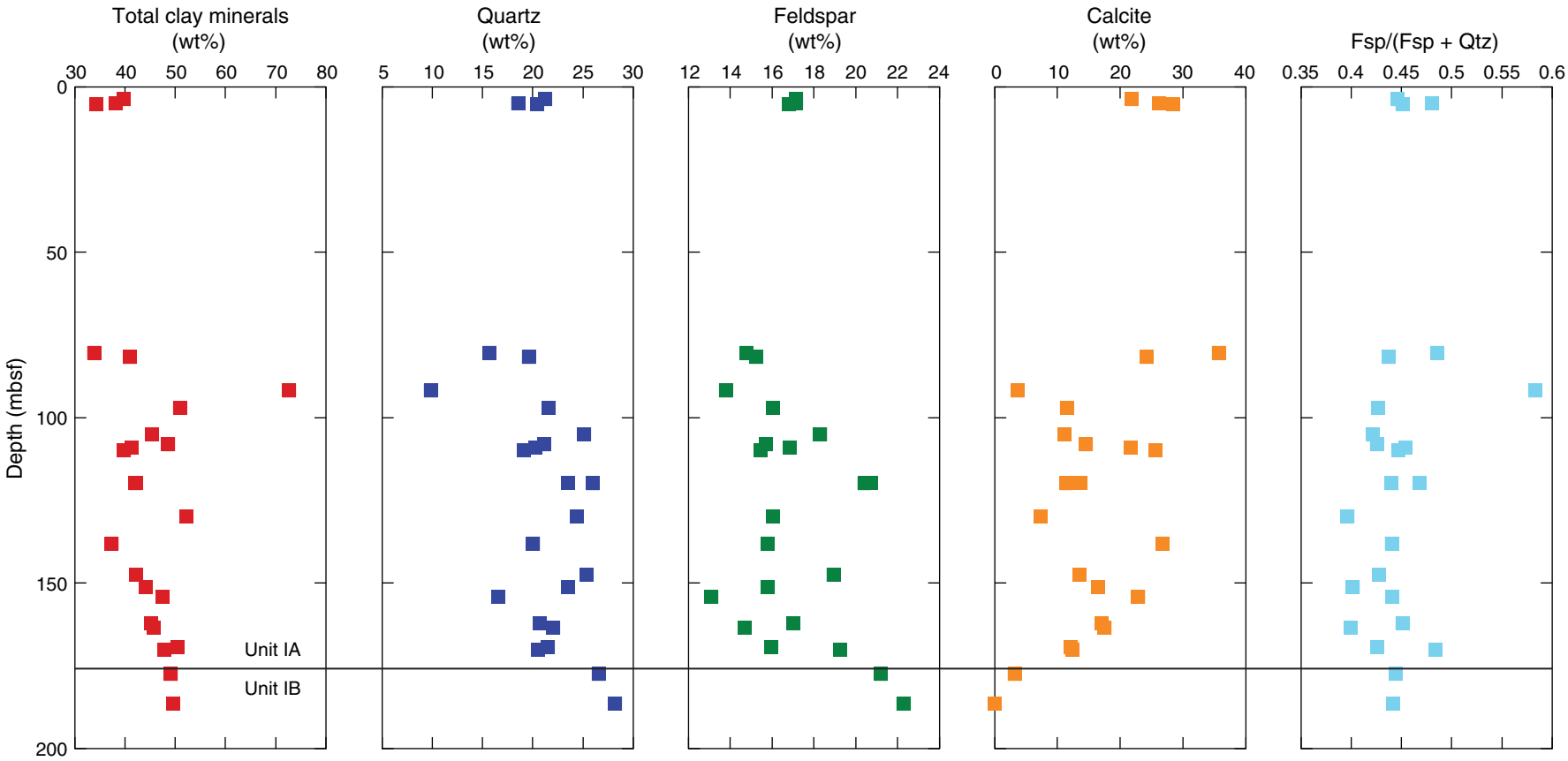

Figure F13. Characteristic features of MTDs within Subunit IA, Hole C0021B. **A.** Mud clasts overlain by thin, draping sand at top of MTD A (interval 338-C0021B-3H-6, 71–99 cm). **B.** Mud clasts overlain by thin, draping sand at top of MTD B (interval 338-C0021B-7H-7, 95–123 cm). **C.** Shear zone and tilted bedding in MTD B (interval 338-C0021B-7H-8, 57–86 cm). **D.** Tilted bedding in MTD B. (interval 338-C0021B-7H-8, 86–114 cm).

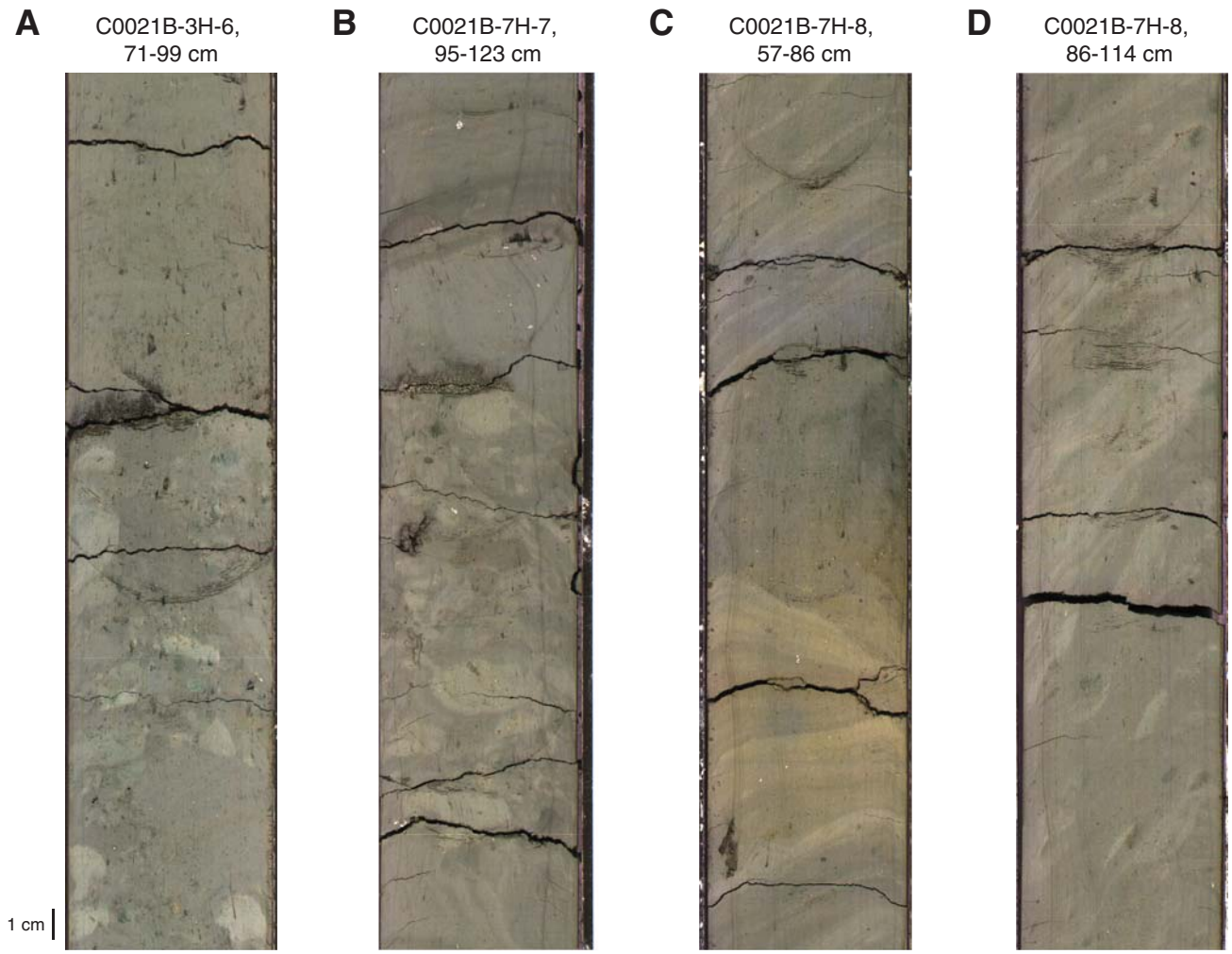

Figure F14. Depth profile of XRF bulk chemical composition data, Hole C0021B. MTD = mass transport deposit.

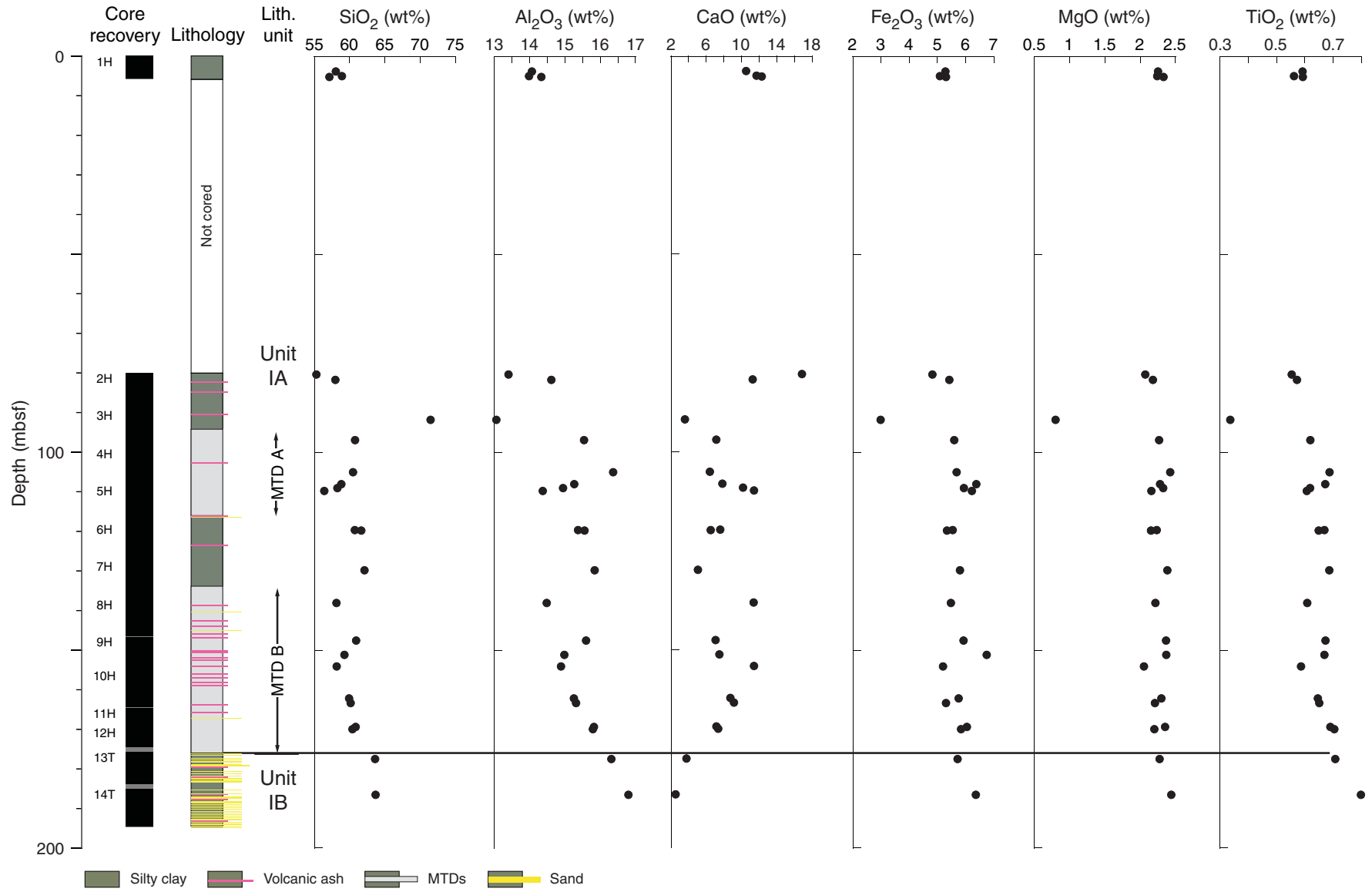

Figure F15. Variation in bedding strike and dip, Hole C0021B. Core recovery, possible mass transport deposit (MTD) interval locations (see **"Lithology"**), and lithologic units are also shown. RHR = right-hand rule.

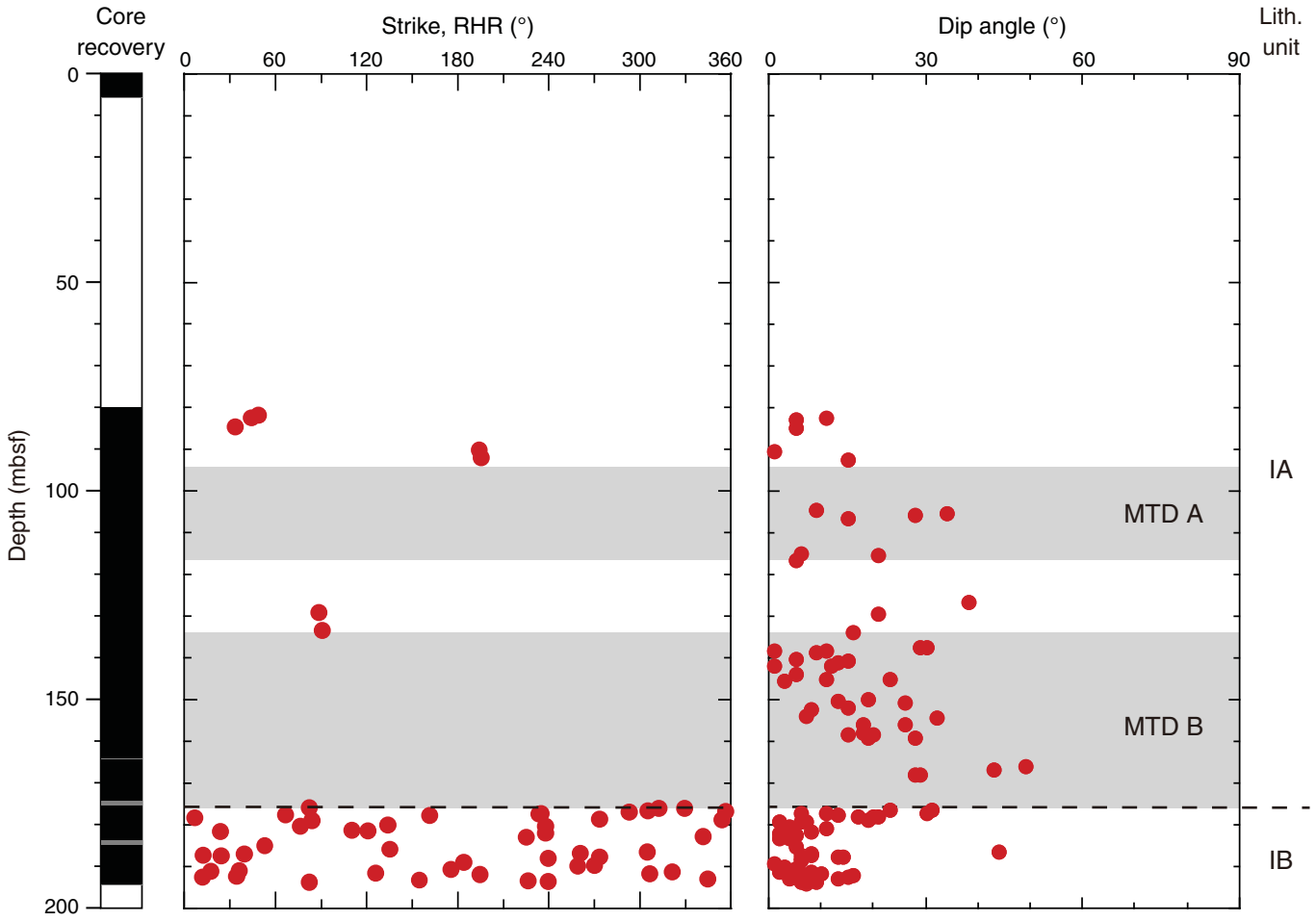

Figure F16. Lower-hemisphere equal-area projections of poles to bedding, Hole C0021B. **A.** Bedding, lithologic Subunit IA. Note that orientations of bedding within MTD depths are excluded because paleomagnetic poles would be disrupted within MTDs. **B.** Bedding, lithologic Subunit IB.

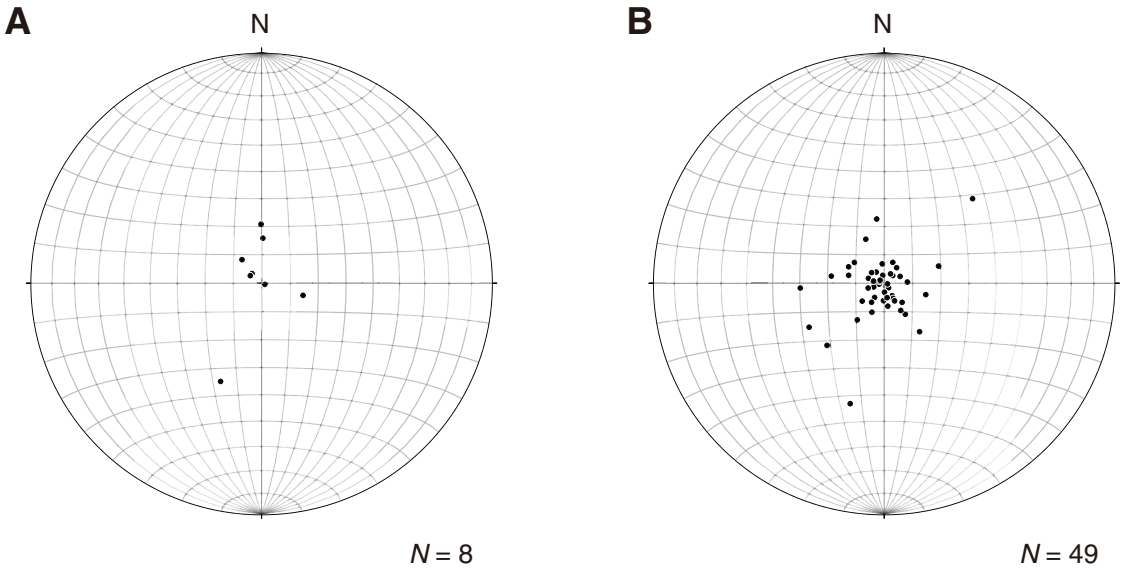

Figure F17. Examples of structures observed on working halves of split cores. **A.** Striated surface associated with a reverse fault (interval 338-C0021B-7H-2, 84–90 cm). **B.** Shear zone (interval C0021B-4H-1, 114–131 cm). **C.** X-ray CT image of shear zone (interval C0021B-9H-1, 51–71 cm).

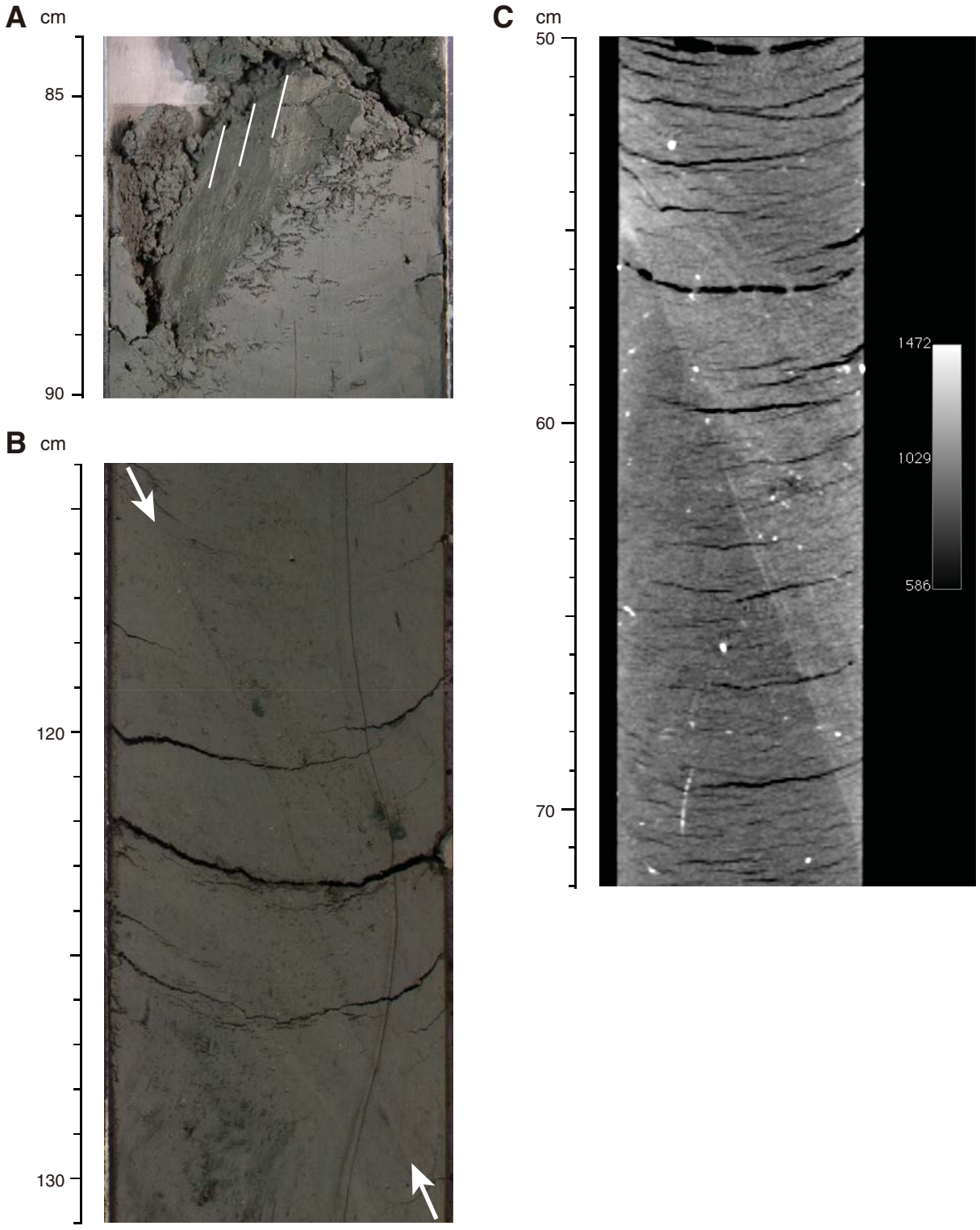

Figure F18. Variation in dip angle of faults and shear zones, Hole C0021B. Core recovery, mass transport deposit (MTD) locations (see "Lithology"), and lithologic units are also shown.

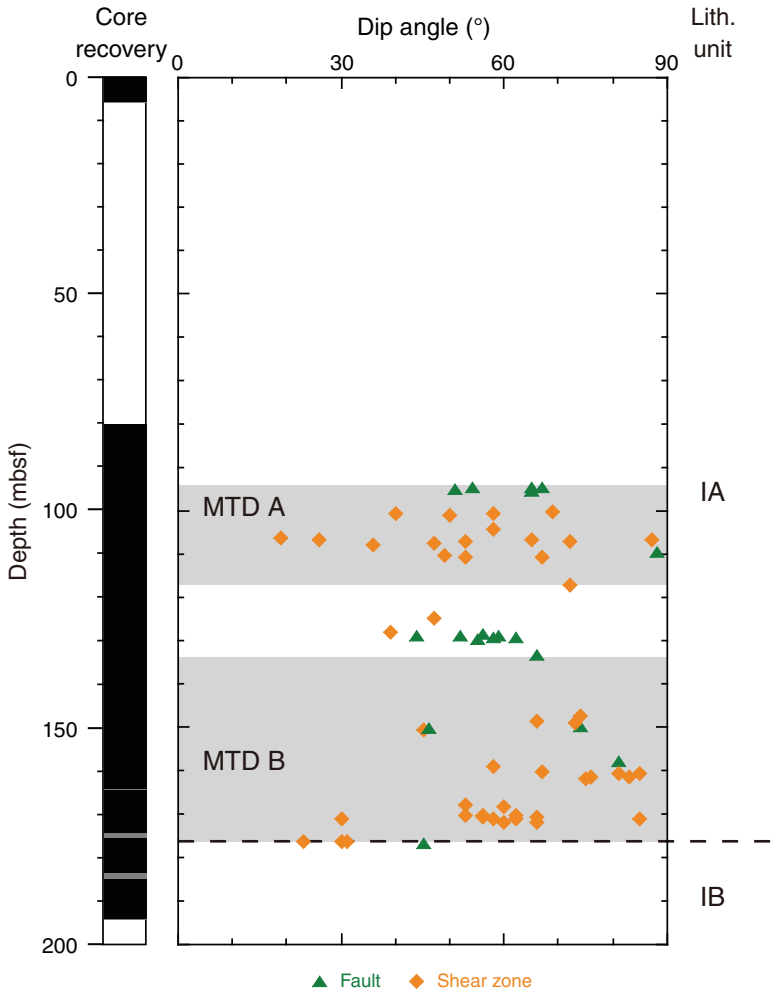

Figure F19. Example of shear zone (red arrows) and fault (white arrows) crossing MTD-related mud clasts shown on core split surface (left) and on X-ray CT image (right) (interval 338-C0021B-3H-6, 108–140 cm).

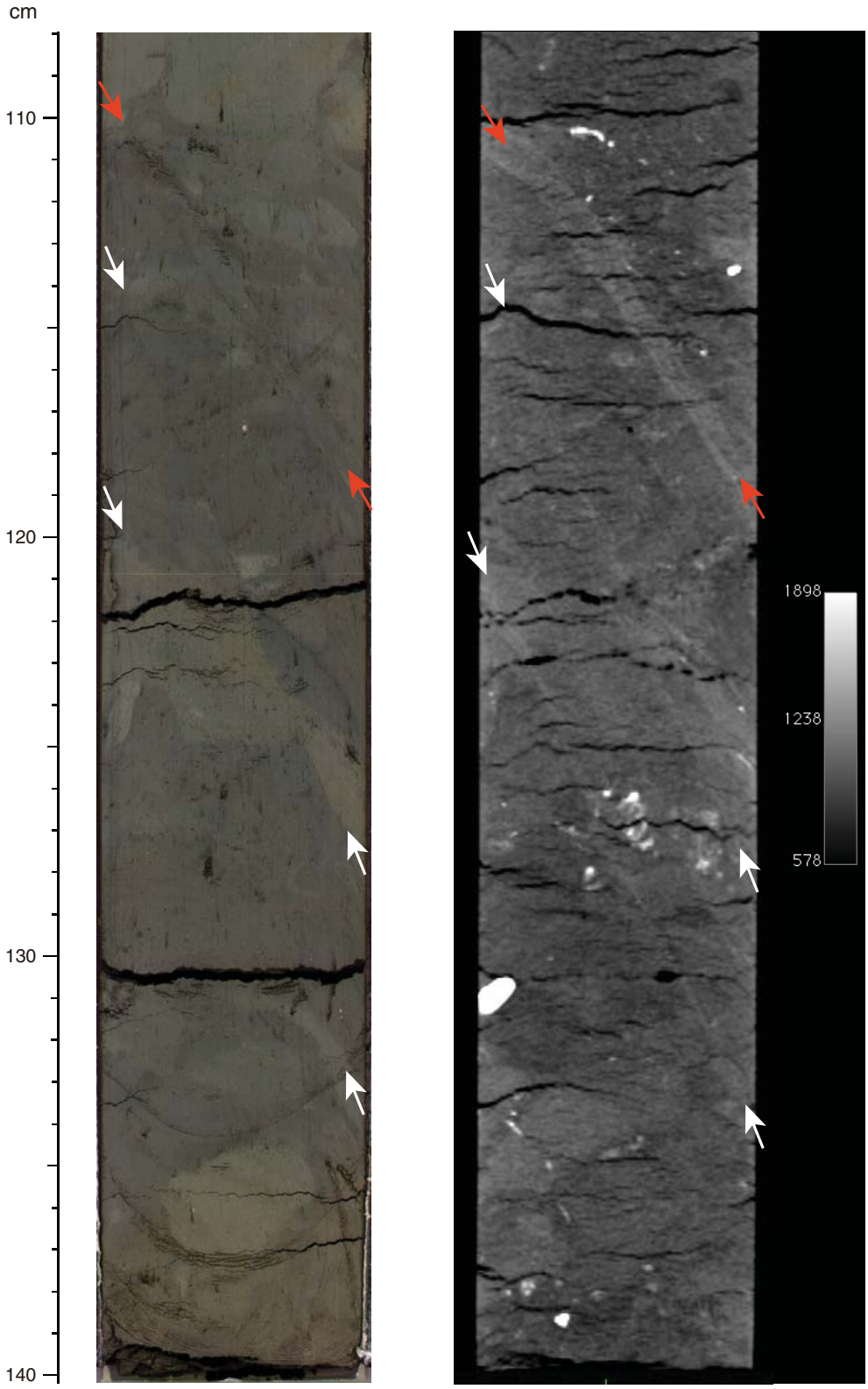

Figure F20. Lower-hemisphere equal-area projections of orientations of faults and shear zones in cores, Hole C0021B. **A.** Faults. Dots on great circles = striations, arrows = slip vectors of hanging wall relative to footwall. **B.** Shear zones.

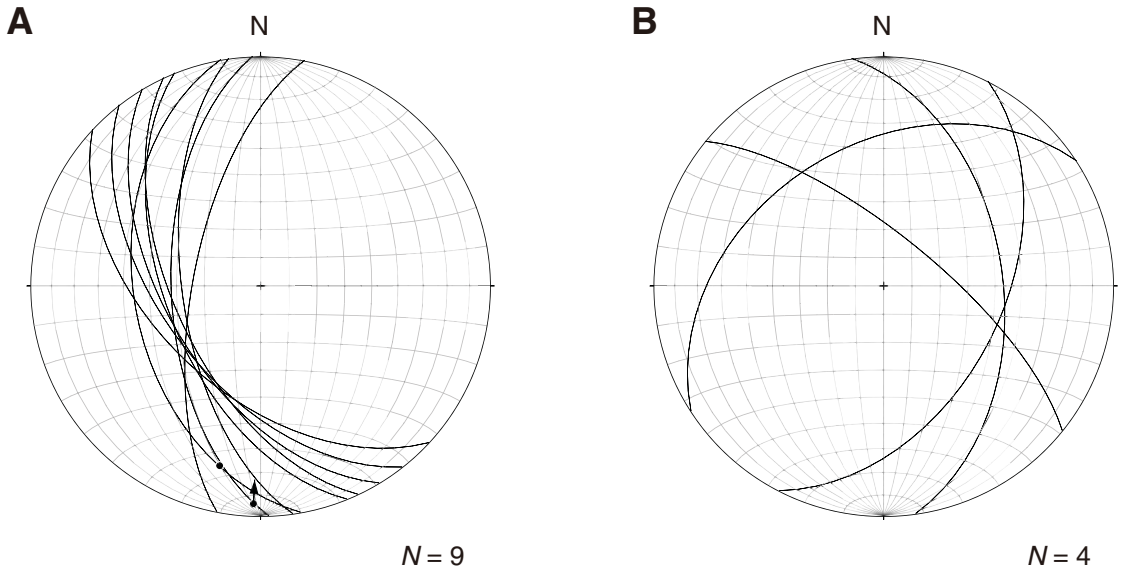

Figure F21. Shear zone truncating bedding (interval 338-C0021B-13T-1, 53–84 cm) shown on core split surface (left) and on X-ray CT image (right). This shear zone could represent the basal shear zone of MTD B. The X-ray CT image is oblique to the core split surface; hence the apparent differences, as seen in depth locations, thicknesses, and (apparent) dip angles of the structures between the two images.

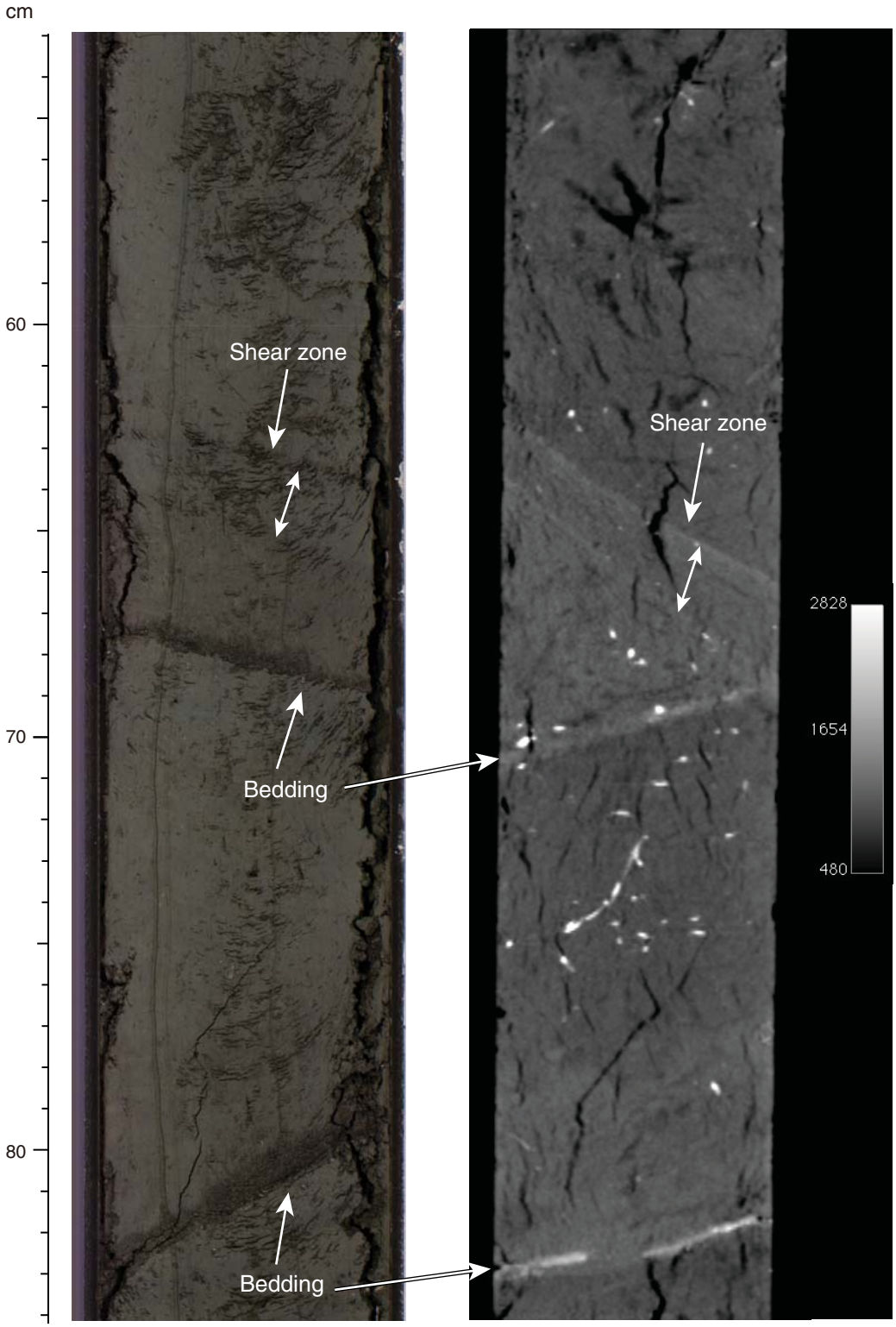

Figure F22. Variation of refractive index, alkalinity, pH, chlorinity, Br^-, SO_4^{2-}, PO_4^{3-}, NH_4^+, Si, and B in Hole C0021B IW samples. MTD = mass transport deposit.

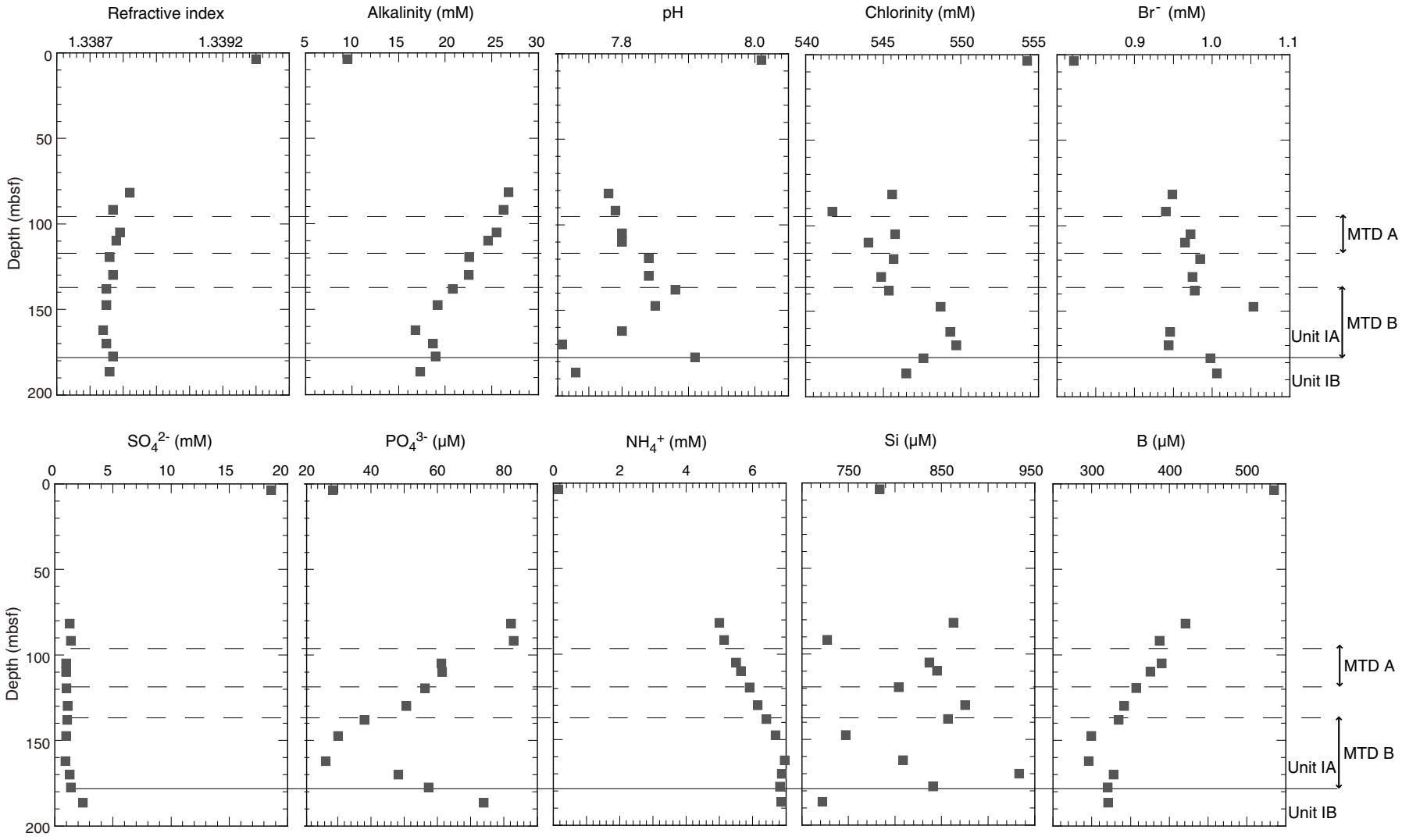

Figure F23. Variation of alkaline metals (Na, K, Li, Rb, and Cs) and alkaline earth metals (Mg, Ca, Sr, and Ba) in Hole C0021B IW samples. MTD = mass transport deposit.

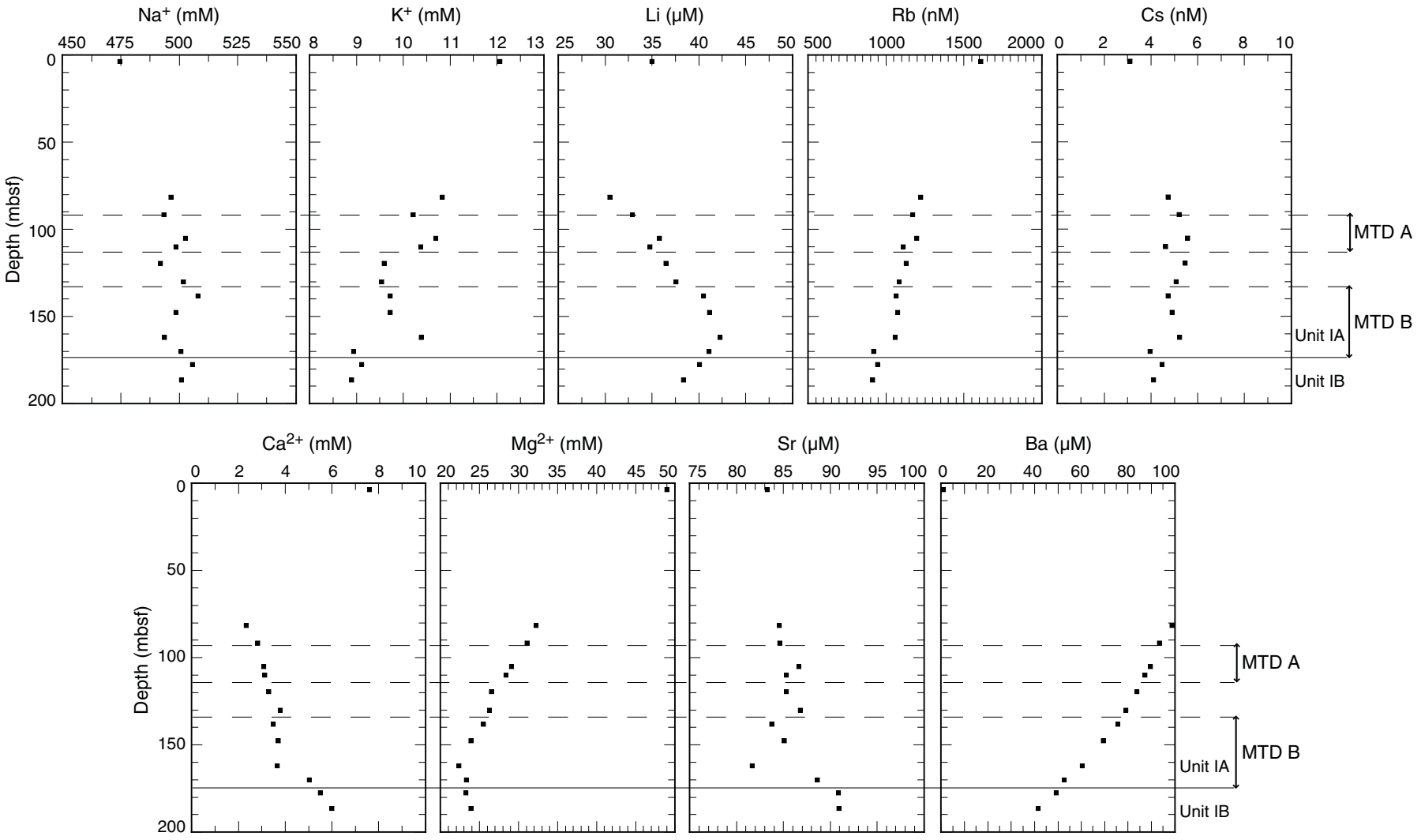

Figure F24. Variation of Fe, Mn, Cu, V, Mo, Pb, Zn, and U in Hole C0021B IW samples. MTD = mass transport deposit.

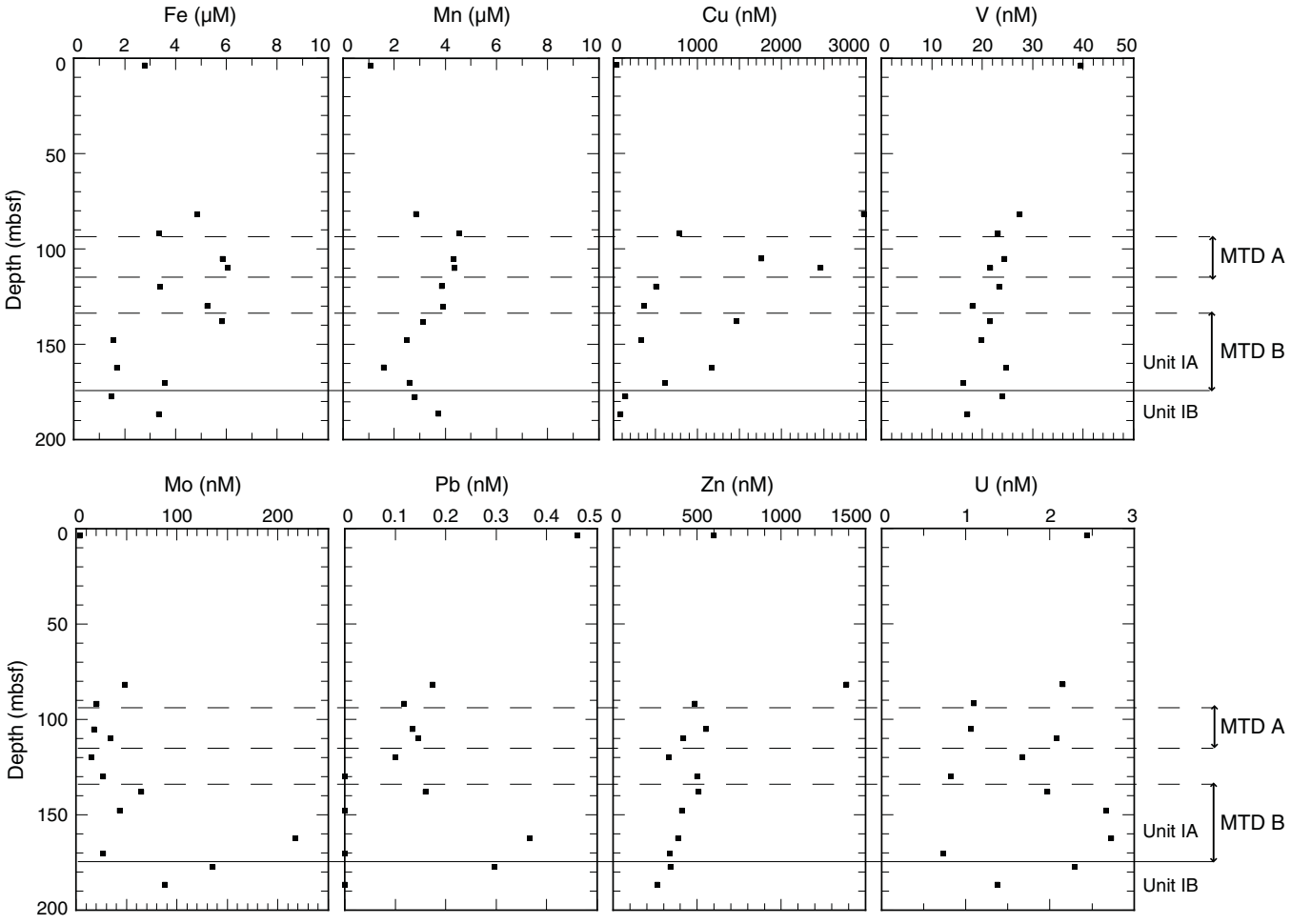

Figure F25. Comparison of data obtained by different methods for extracting headspace gas. Oven = samples analyzed by the conventional method using an oven, NaOH = samples analyzed using an alkaline solution (NaOH). Diagonal 1:1 line is provided for reference.

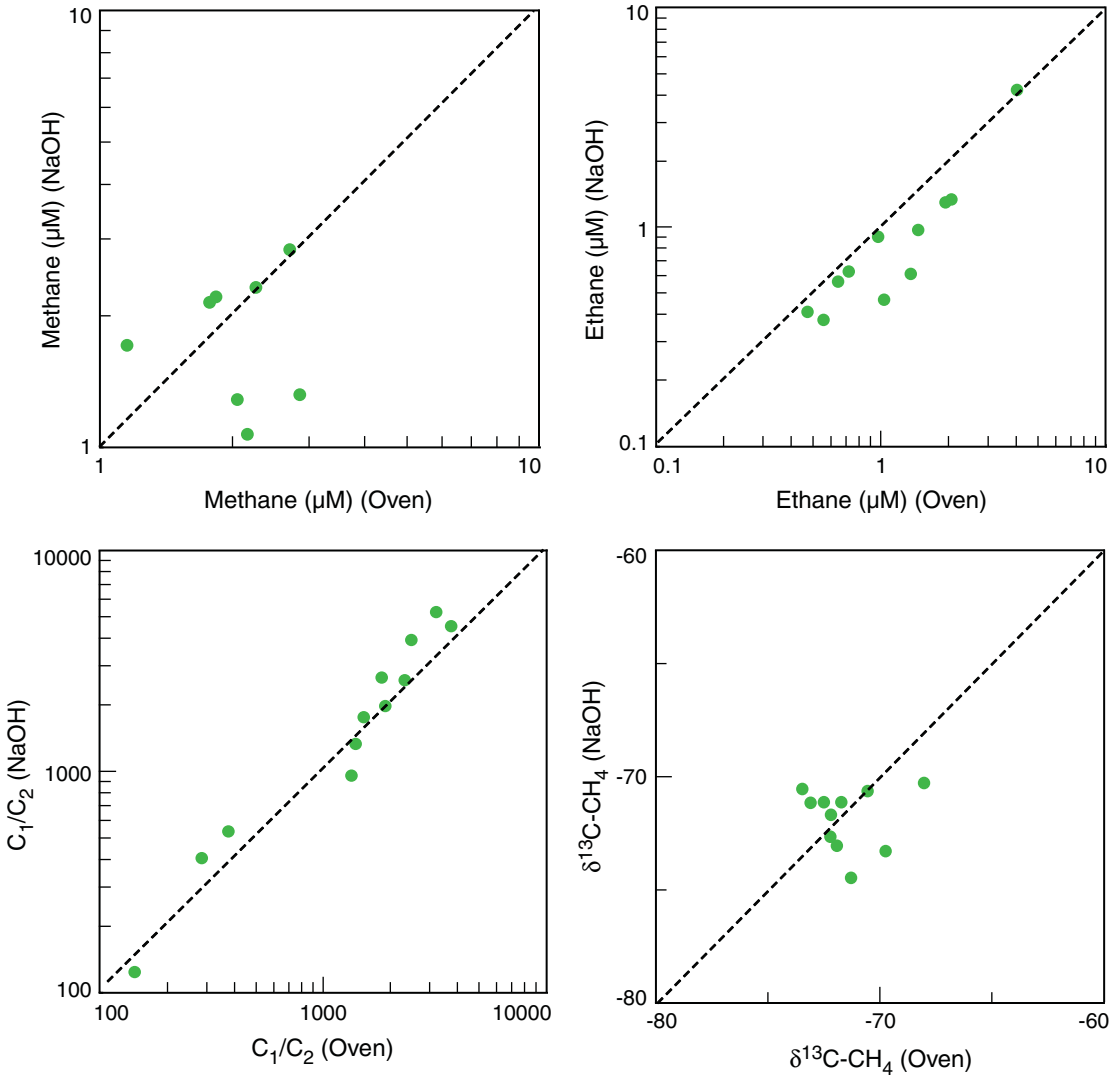

Figure F26. Vertical profiles of methane (CH_4), ethane (C_2H_6), and propane (C_3H_8) concentrations in headspace gas, Hole C0021B. MTD = mass transport deposit.

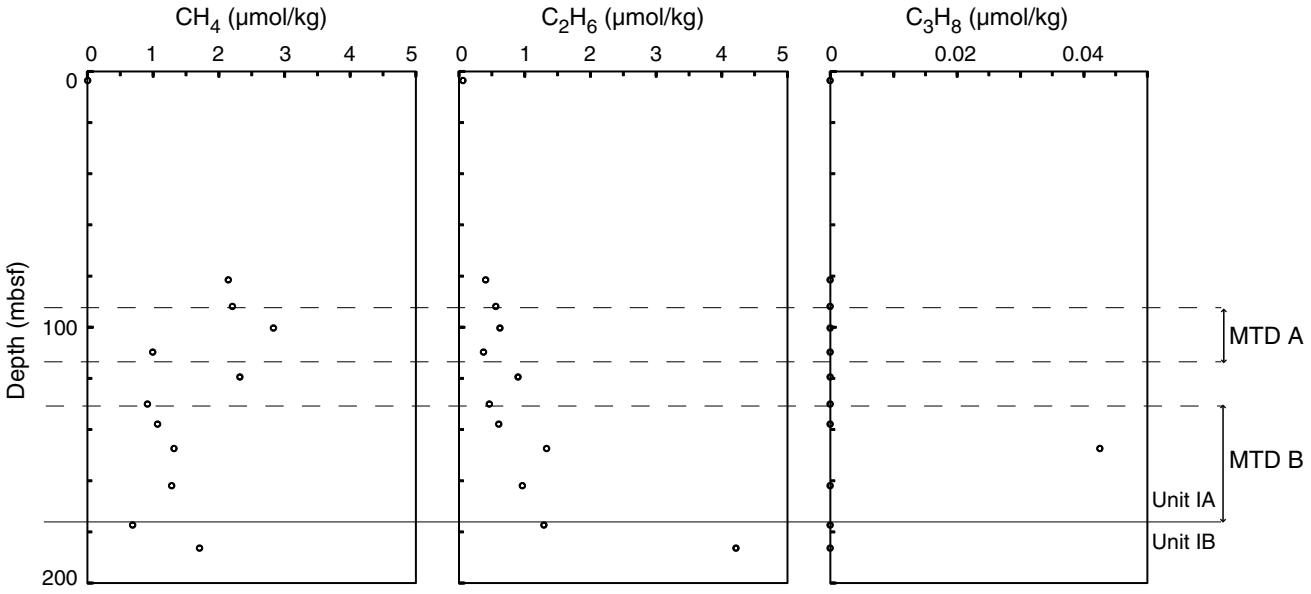

Figure F27. Vertical profiles of $C_1/(C_2 + C_3)$ ratio and $\delta^{13}C\text{-}CH_4$ in headspace gas, Hole C0021B. VPDB = Vienna Peedee belemnite. MTD = mass transport deposit.

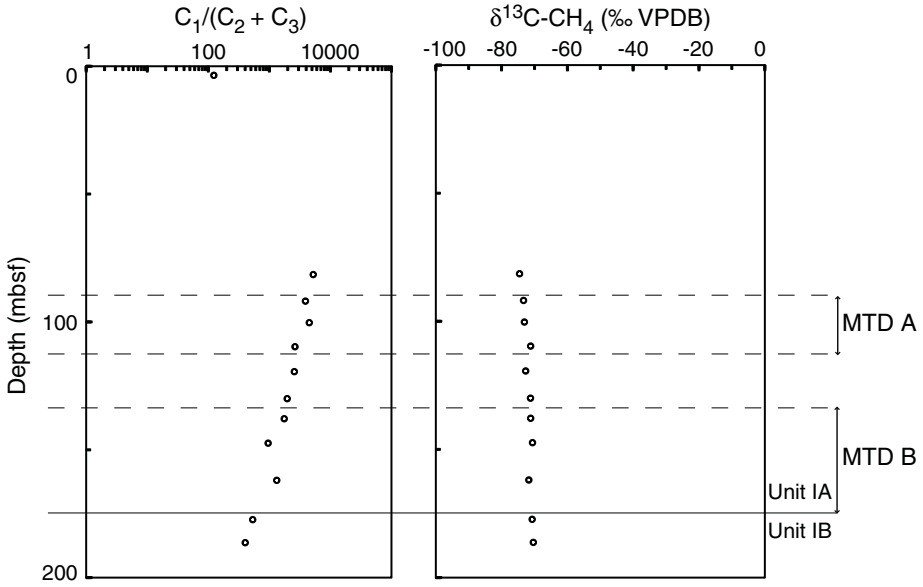

Figure F28. Relationship between $C_1/(C_2 + C_3)$ ratio extracted by the NaOH addition method and $\delta^{13}C\text{-}CH_4$ in headspace gas, Hole C0021B. VPDB = Vienna Peedee belemnite.

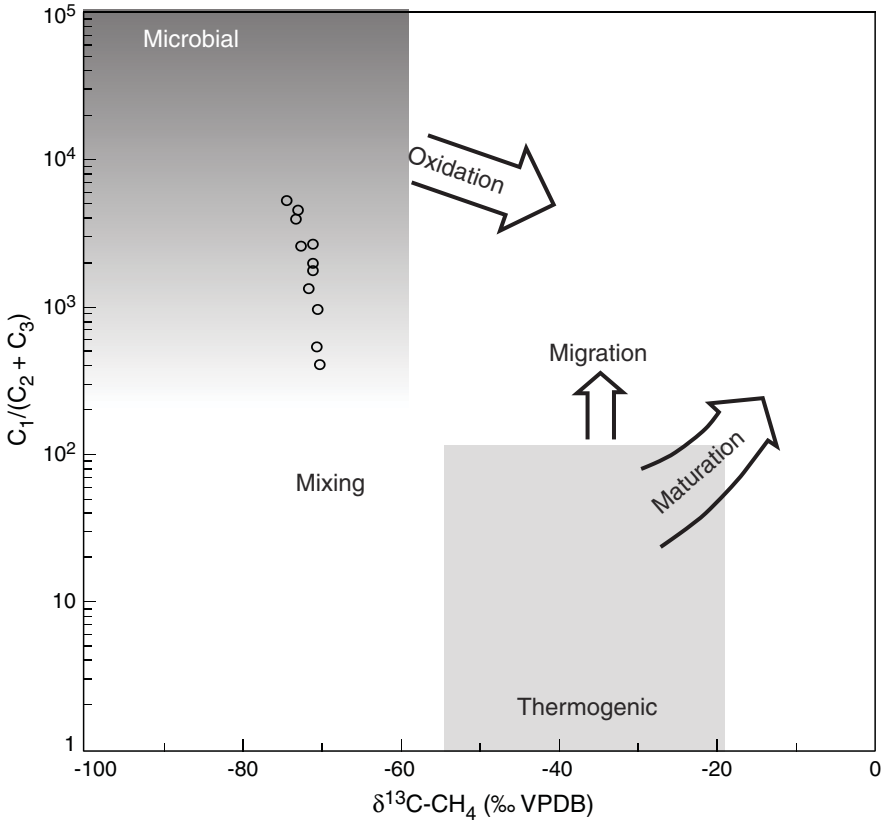

Figure F29. $CaCO_3$, total organic carbon (TOC), total nitrogen (TN), C/N ratio, and total sulfur (TS), Hole C0021B. MTD = mass transport deposit.

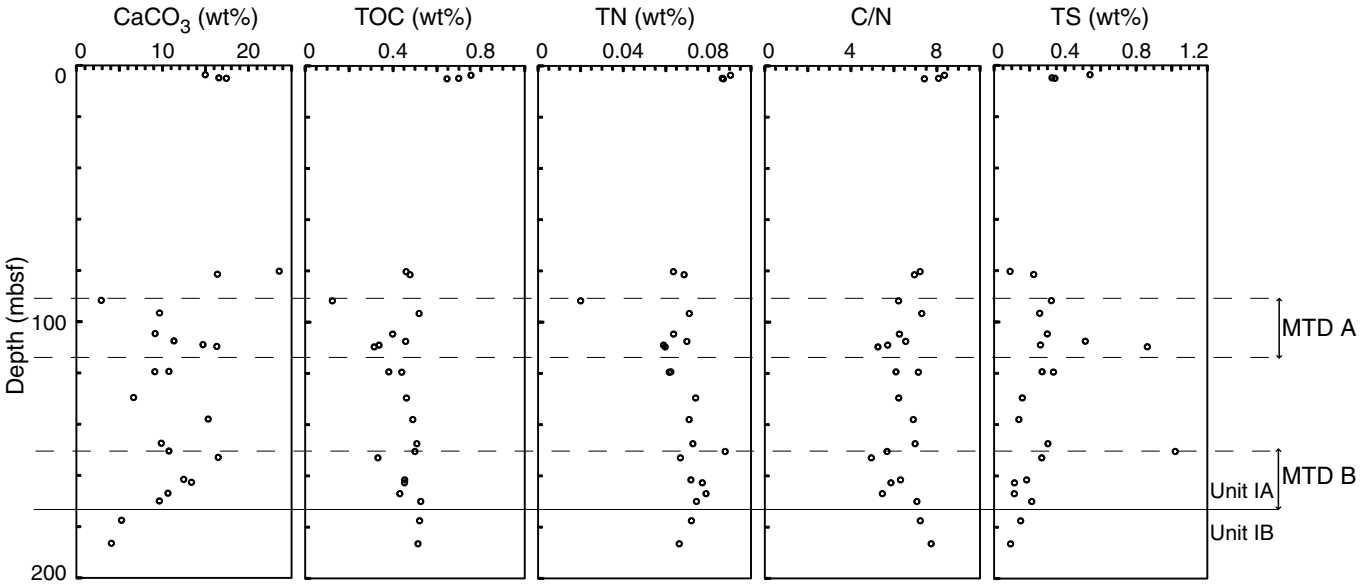

Figure F30. MSCL-W measurements on whole-round cores, Hole C0021B. **A.** Gamma ray attenuation (GRA) bulk density. **B.** Magnetic susceptibility. **C.** Natural gamma radiation (NGR). cps = counts per second. **D.** Non-contact electrical resistivity.

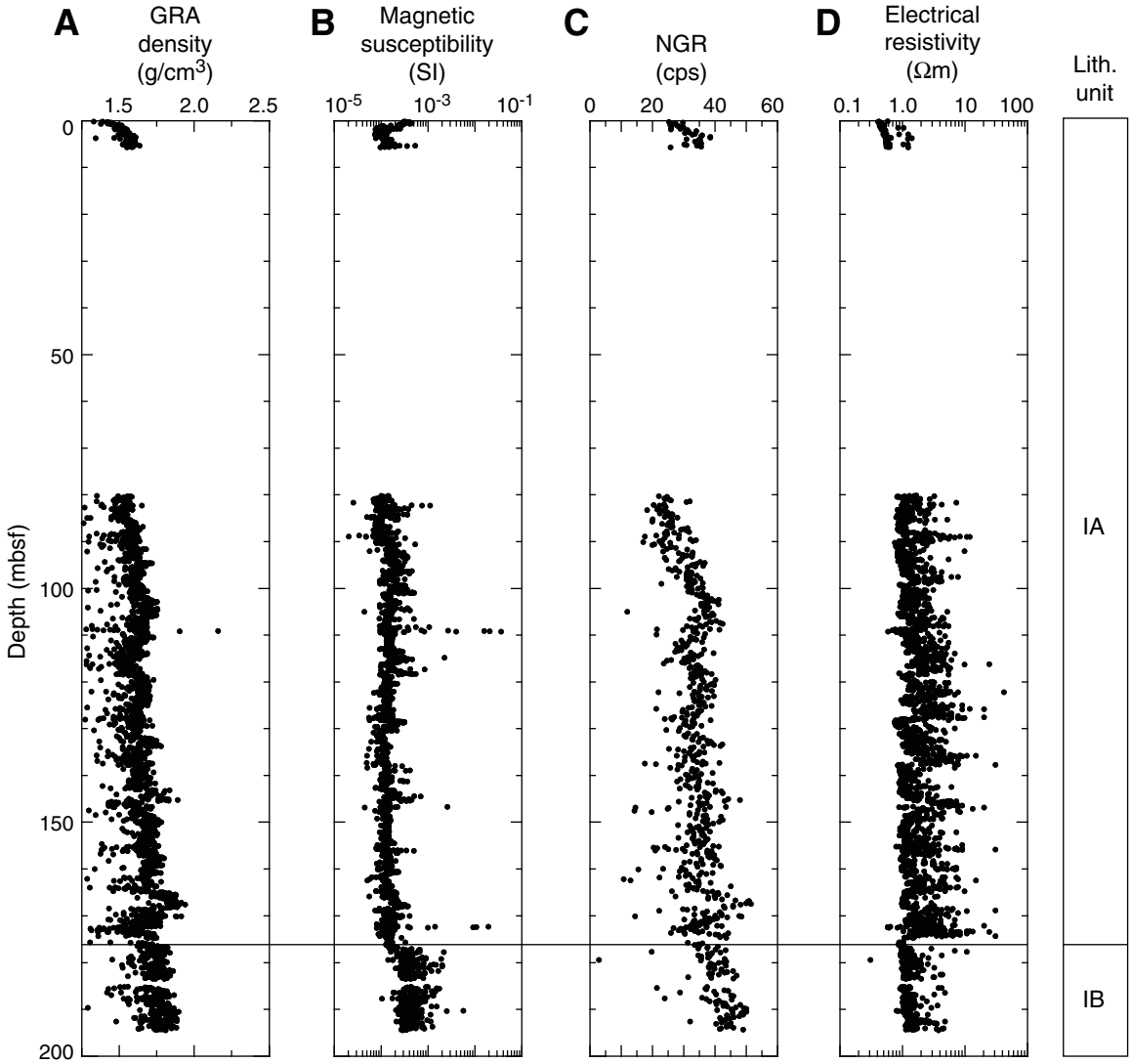

Figure F31. MSCL-W ultrasonic *P*-wave velocity (V_P) measurements (Core 338-C0021B-1H).

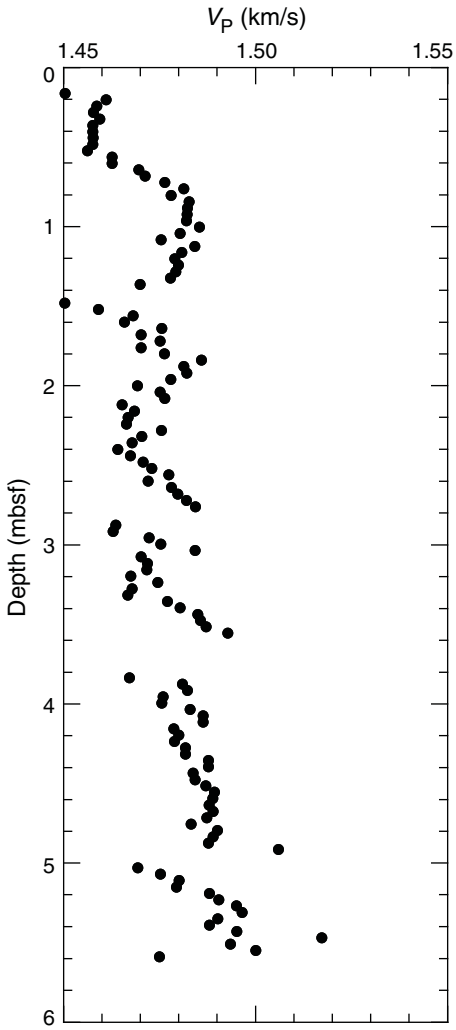

Figure F32. MAD measurements, Hole C0021B. **A.** Bulk density. **B.** Porosity. **C.** Grain density. Open squares = measurements on the *Chikyu*, black dots = shore-based measurements at Kochi Core Center (KCC), red dots = sand samples, green dots = ash samples. MTD = mass transport deposit.

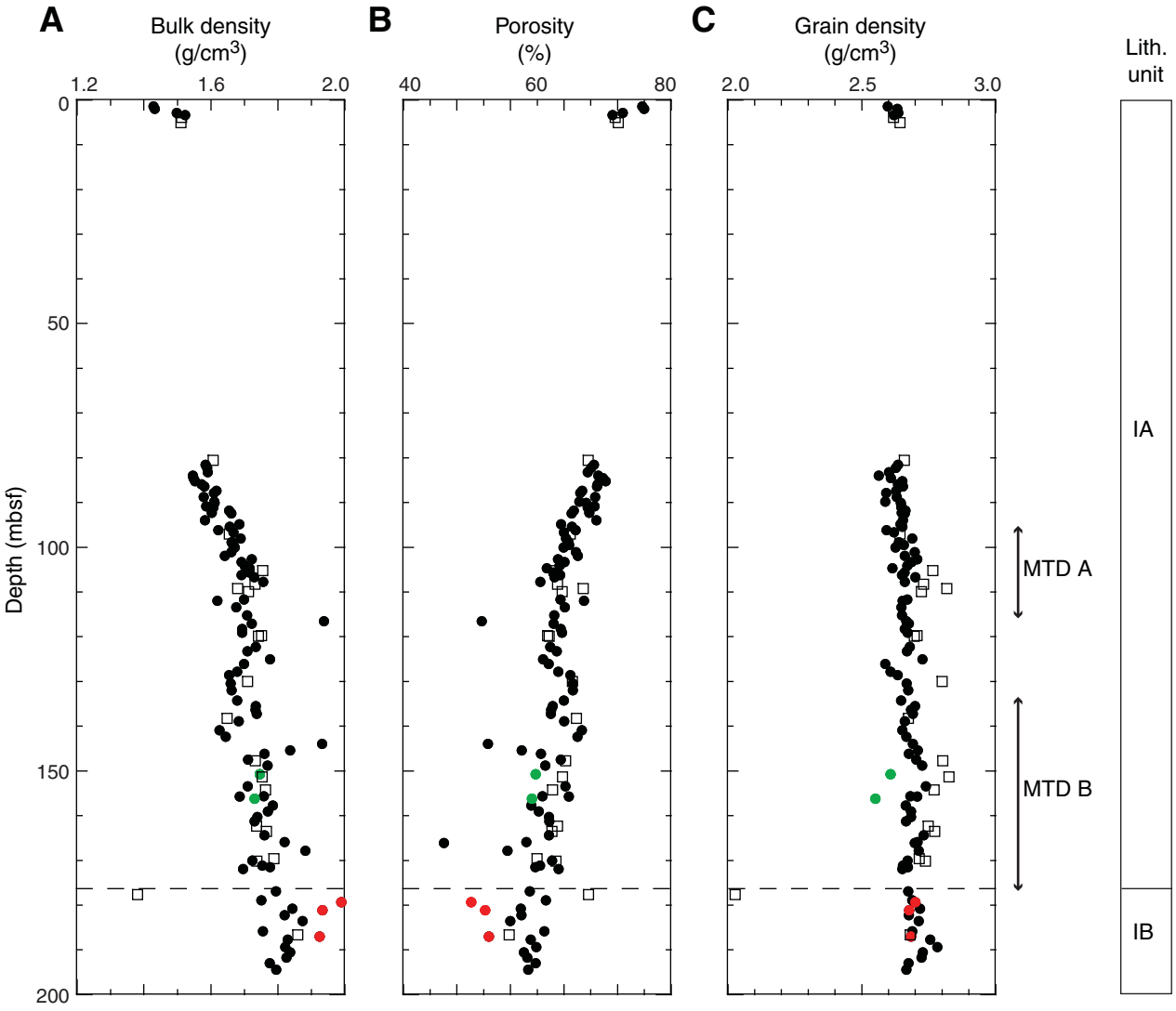

Figure F33. Thermal conductivity, Hole C0021B.

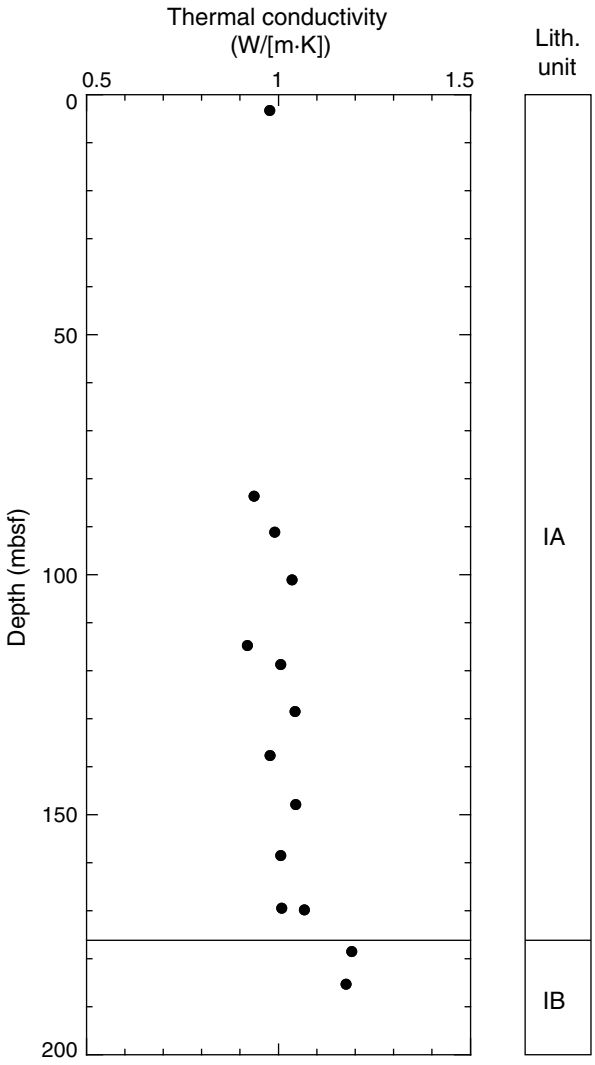

Figure F34. Electrical resistivity, Hole C0021B. Red = Wenner probe measurements, black = MSCL-W measurements.

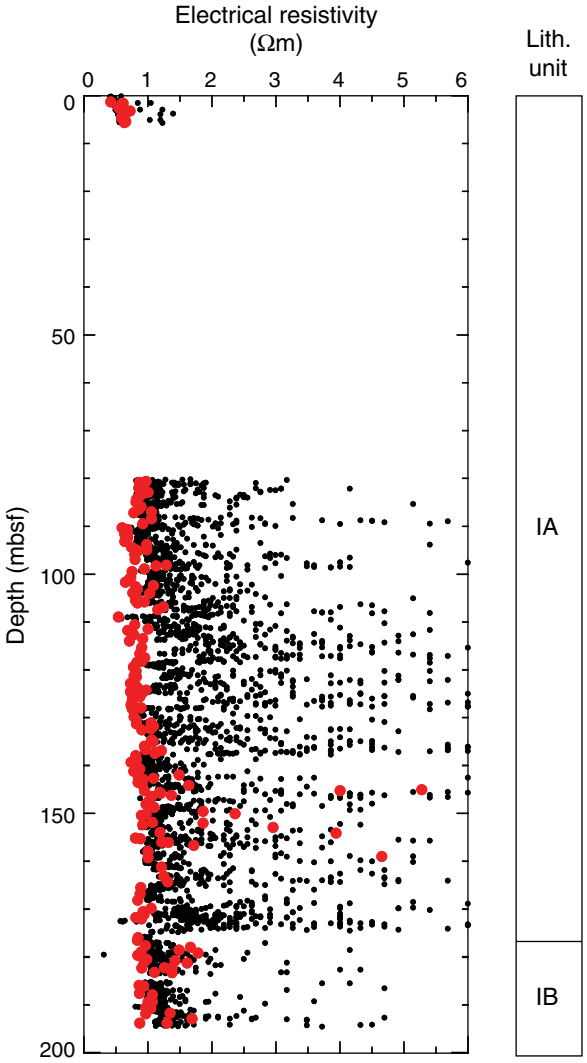

Figure F35. Undrained shear strength, Hole C0021B. MTD = mass transport deposit.

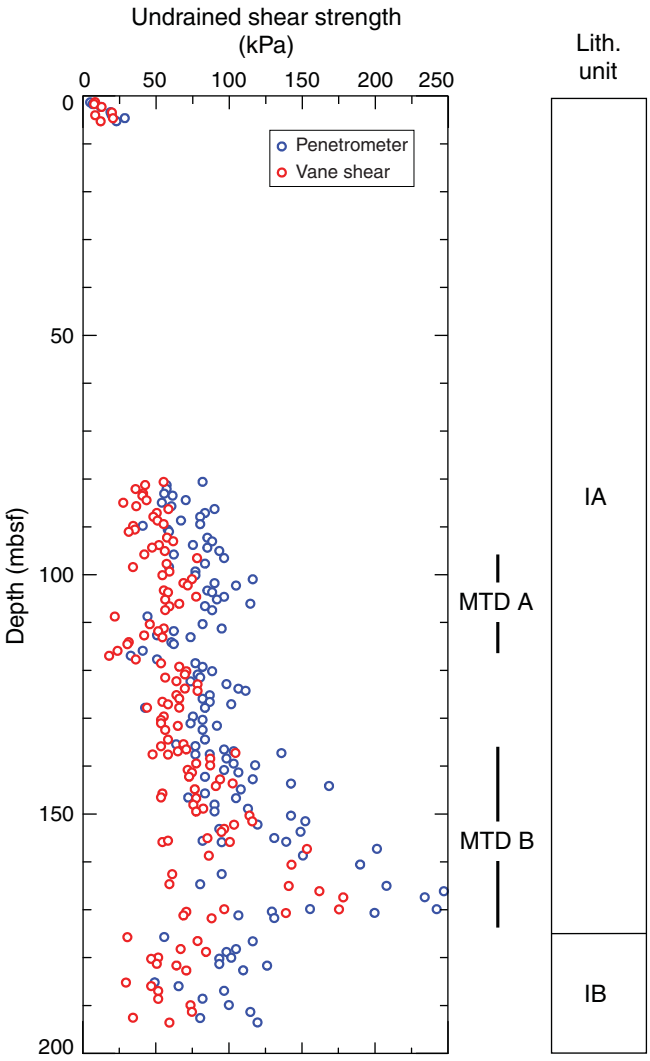

Figure F36. Color reflectance, Hole C0021B. **A.** L*. **B.** a*. **C.** b*.

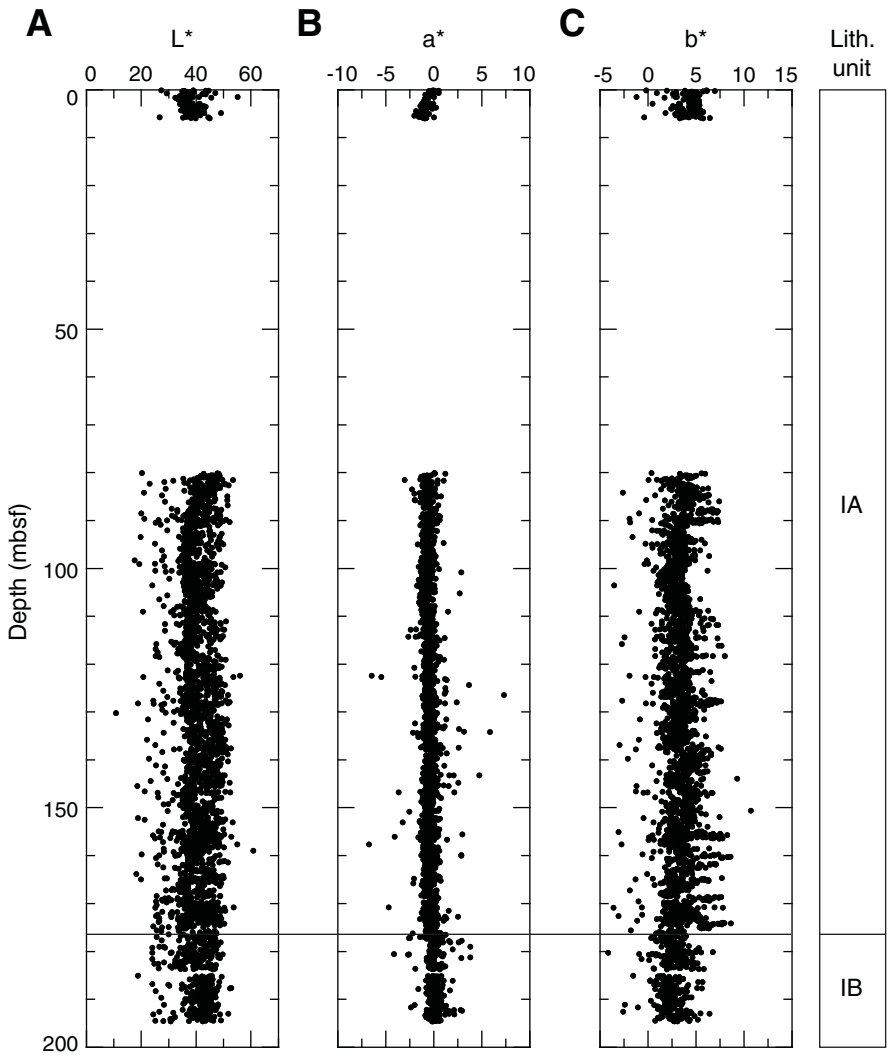

Figure F37. Vector component diagrams of progressive AF demagnetization of samples (**A**) 338-C0021B-2H-2, 50–52 cm, and (**B**) 12H-3, 104–106 cm. Steps are in mT for AF demagnetization. Solid squares = projection onto the horizontal plane, open squares = projection onto the vertical plane.

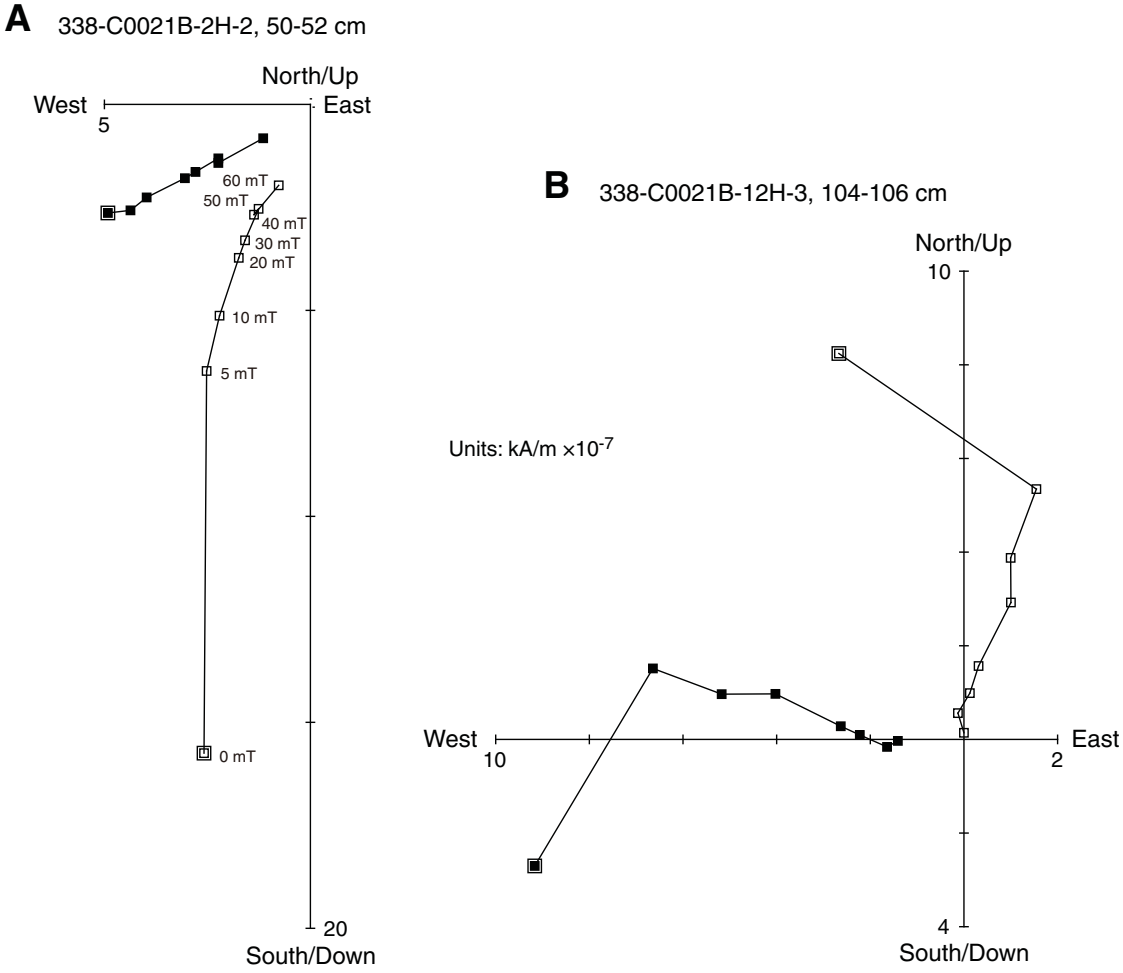

Figure F38. (**A**) Declination, (**B**) inclination, and (**C**) intensity, Hole C0021B. Gray = NRM, red = after 20 mT AF demagnetization. Shaded intervals identify locations of mass transport deposits (MTDs) A and B.

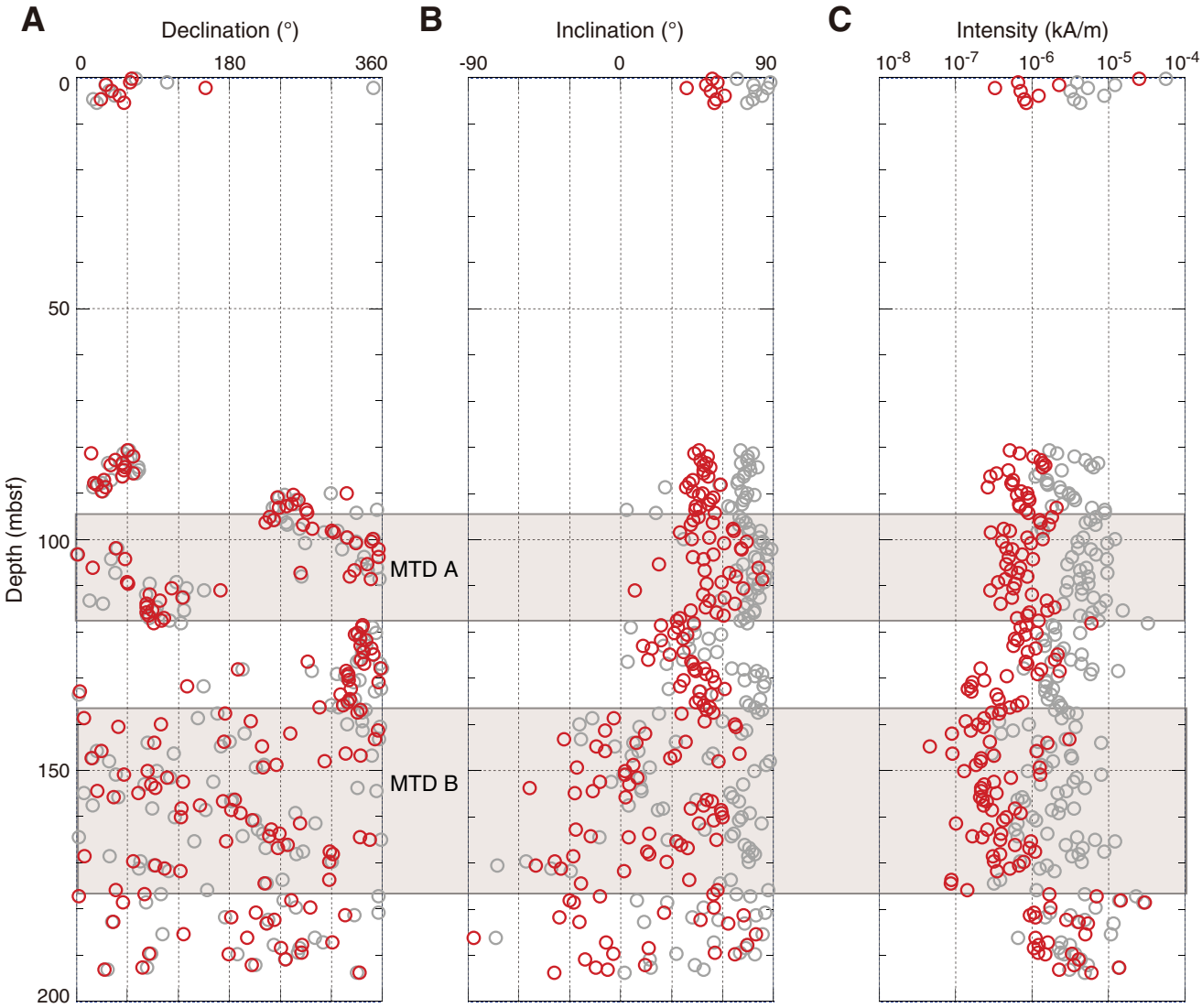

Figure F39. Downhole variations of inclination, Holes (**A**) C0018A and (**B**) C0021B. Inferred polarity, mass transport deposit (MTD), and tephra horizons are also shown. Black = normal polarity, white = reversed polarity. No polarity interpretation provided for gray areas. ? = polarity change indicated by data but magnetostratigraphic correlation not known.

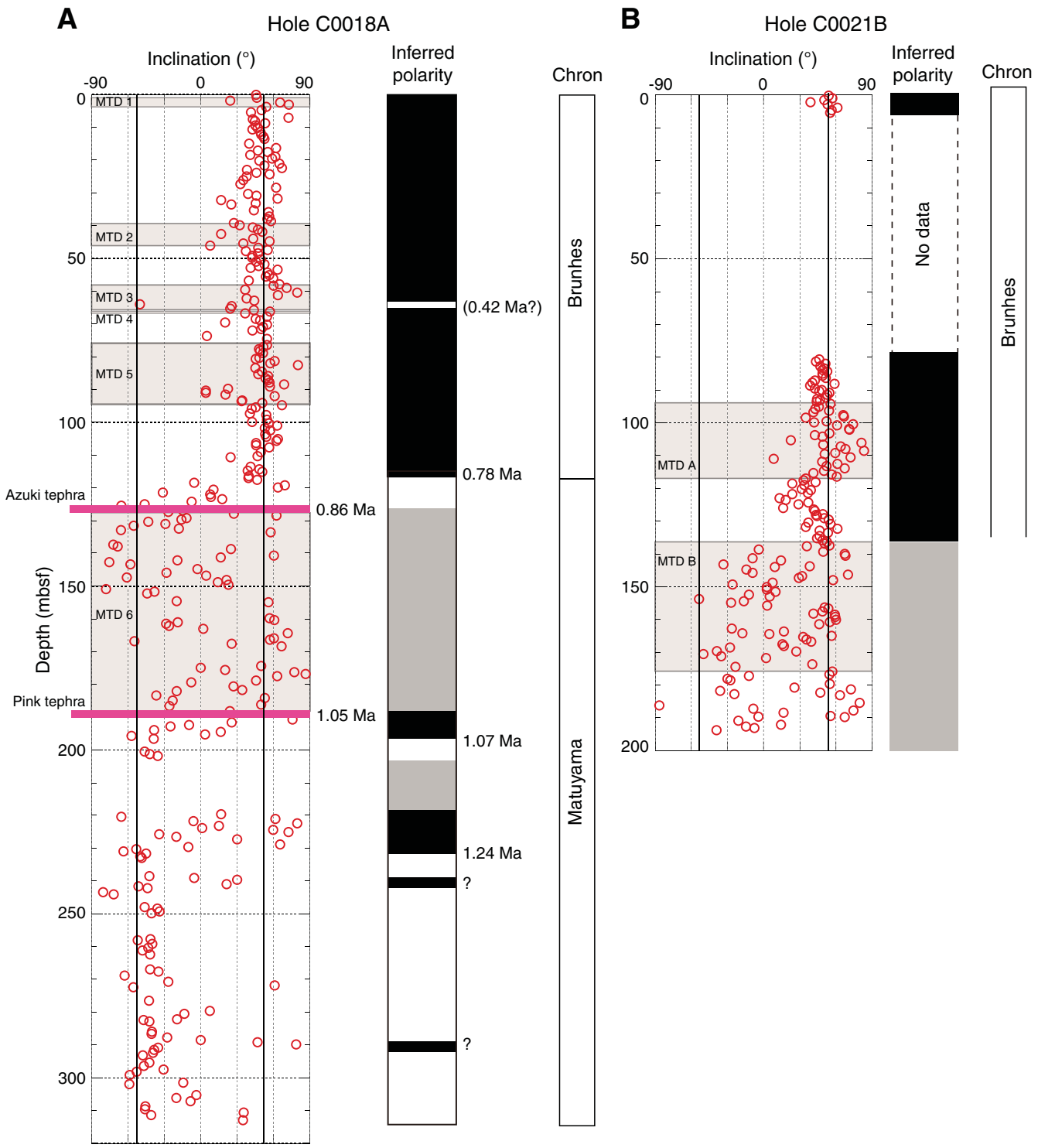

Figure F40. Lithostratigraphic summary columns of Sites C0018 and C0021 overlain onto a cross-section of the seismic volume linking the two sites. Seismic line location is shown in Figure F2 (A–A′). MTD = mass transport deposit. VE = vertical exaggeration.

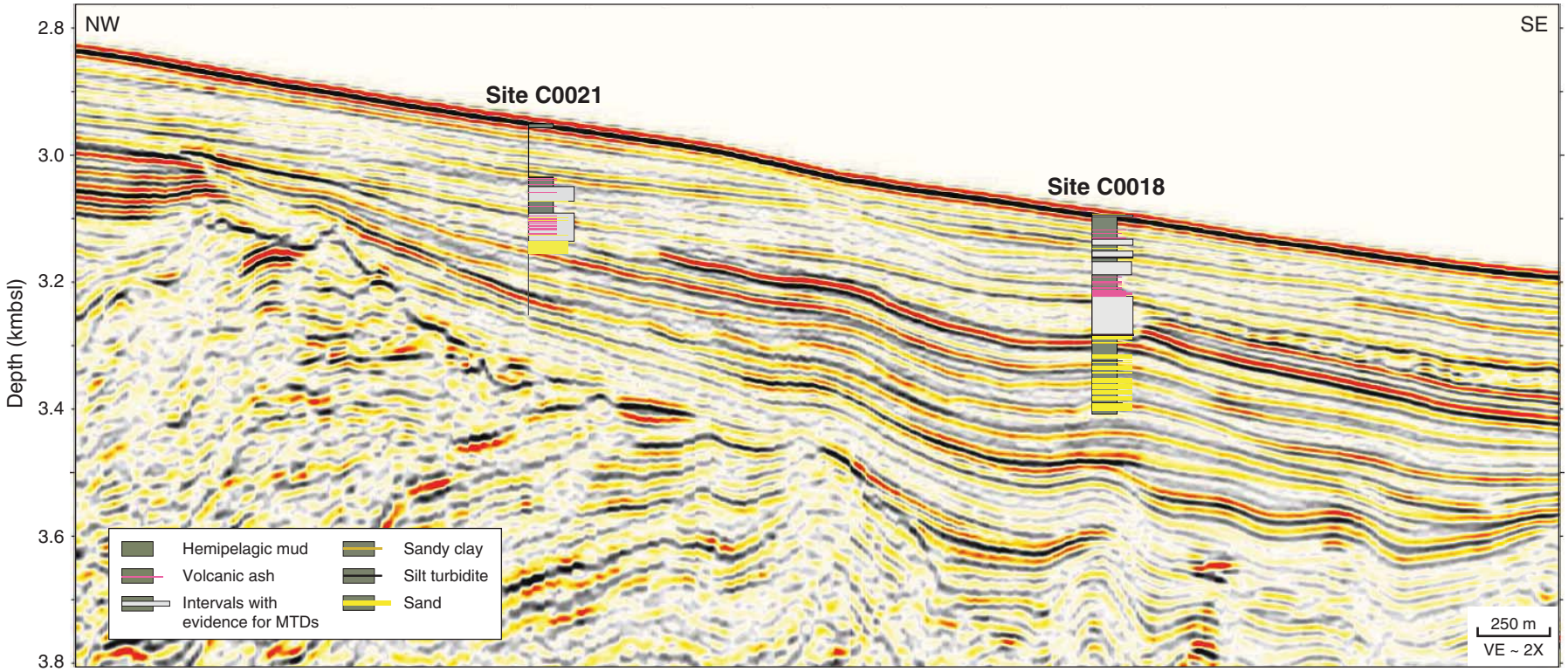

Figure F41. Core-log-seismic integration, Site C0021. Ring resistivity and gamma ray LWD data from Hole C0021A; seismic data from In-line 2270 of the Kumano 3-D PSDM volume (Moore et al., 2009); stratigraphic summary column of Hole C0021B with mass transport deposit (MTD) intervals and lithologic units; tadpole plot of bedding dip angles and directions; and medium button static resistivity image. Dashed lines highlight correlations discussed in the text.

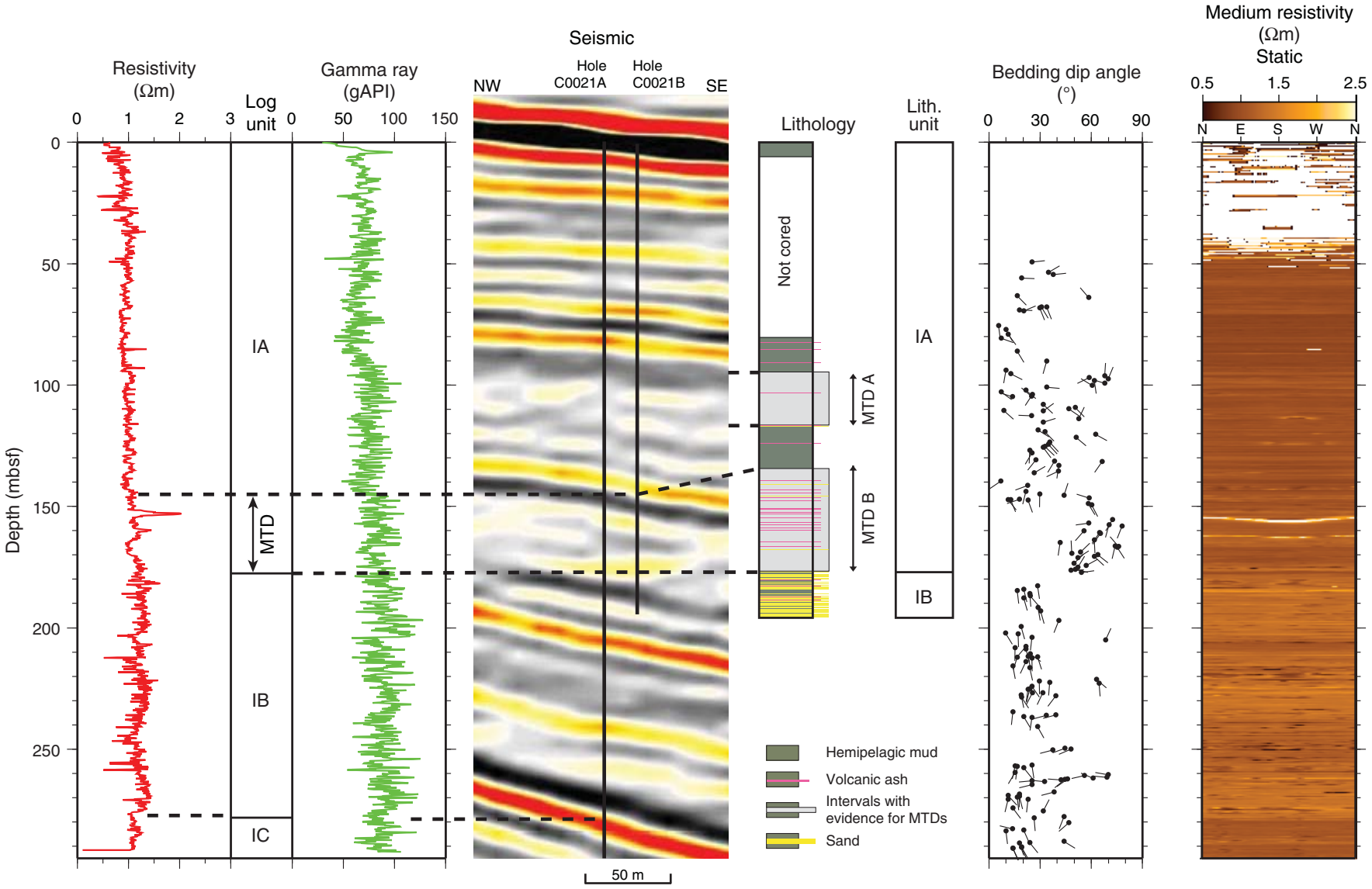

Table T1. Lithologic units defined, Hole C0021B.

Unit	Core, section, interval (cm) Top	Core, section, interval (cm) Bottom	Depth (mbsf) Top	Depth (mbsf) Bottom	Thickness (m)	Stratigraphic age	Lithologic description	Process of formation	Interpretation
IA	338-C0021B-1H-1, 0	338-C0021B-13T-1, 66	0.00	176.16	176.16	Holocene–Pleistocene	Silty clay with occasional thin interbeds of fine sand and ash and intercalated chaotic to deformed beds (MTD)	Hemipelagic settling, thin-bedded turbidites, volcanic ash fall, and submarine landslides	Slope-basin succession
IB	13T-1, 67	14T-CC, 34	176.17	194.69	18.52	Pleistocene	Thin sand beds interbedded with silty clay and ash	Hemipelagic settling and turbidites	Turbiditic slope-basin succession

MTD = mass transport deposit.

Table T2. XRD analysis results, Hole C0021B. Samples were taken from whole-round samples.

Core, section, interval (cm)	Sample	Depth (mbsf)	Integrated peak area (total counts)				Absolute mineral abundance calculated from SVD normalization factors (wt%)					Relative abundance (wt%)			
			Total clay minerals	Quartz	Feldspar	Calcite	Total clay minerals	Quartz	Feldspar	Calcite	Sum	Total clay minerals	Quartz	Feldspar	Calcite
338-C0021B-															
1H-5WR, 0.0–3.0	CKY-1806710	3.76	2,119	29,763	12,822	14,621	30.05	16.10	12.98	16.55	75.67	39.71	21.28	17.15	21.87
1H-5WR, 118.5–120.5	CKY-1807510	4.945	2,048	26,857	13,038	17,234	29.56	14.38	13.30	20.32	77.55	38.11	18.54	17.15	26.20
1H-6WR, 20.0–23.0	CKY-1804710	5.165	1,775	29,095	12,721	18,217	26.42	15.77	12.96	21.96	77.12	34.26	20.45	16.81	28.48
2H-2WR, 24.0–27.0	CKY-1802310	80.395	1,933	24,598	12,155	23,968	28.27	13.11	12.36	29.89	83.63	33.80	15.68	14.78	35.74
2H-3WR, 15.0–18.0	CKY-1791910	81.71	2,379	29,085	12,171	16,846	32.72	15.69	12.17	19.37	79.95	40.93	19.62	15.23	24.22
3H-4WR, 15.0–18.0	CKY-1794010	91.82	2,920	10,124	7,030	4,166	35.69	4.84	6.77	1.79	49.10	72.70	9.87	13.80	3.64
3H-8WR, 85.0–88.0	CKY-1817110	96.93	3,017	31,123	12,602	9,909	39.54	16.76	12.46	8.92	77.67	50.90	21.58	16.04	11.48
4H-6WR, 15.0–19.0	CKY-1796210	105.065	2,707	37,711	14,899	9,943	37.17	20.53	14.96	9.08	81.75	45.47	25.12	18.31	11.11
4H-8WR, 32.0–35.0	CKY-1818010	108.09	2,962	31,594	12,753	11,868	39.11	17.03	12.62	11.69	80.44	48.62	21.17	15.69	14.53
5H-1WR, 57.0–60.0	CKY-1822210	109.07	2,419	30,838	13,687	15,819	33.83	16.61	13.83	17.79	82.05	41.22	20.24	16.85	21.68
5H-2WR, 0.0–4.0	CKY-1801510	109.81	2,248	27,919	12,081	17,244	31.27	15.03	12.14	20.11	78.55	39.81	19.14	15.45	25.60
6H-3WR, 15.0–18.0	CKY-1803910	119.66	2,381	35,819	16,617	11,245	34.52	19.36	17.03	11.25	82.16	42.02	23.56	20.73	13.69
6H-4WR, 0.0–2.5	CKY-1823410	119.8	2,355	38,329	16,098	9,747	33.86	20.88	16.40	9.17	80.31	42.17	26.00	20.42	11.41
7H-4WR, 0.0–3.0	CKY-1805810	129.86	3,289	36,701	13,356	8,140	42.72	19.94	13.09	5.98	81.73	52.27	24.39	16.02	7.32
8H-2WR, 15.0–18.0	CKY-1809610	138.11	2,100	29,589	12,492	18,101	29.87	16.01	12.60	21.42	79.90	37.39	20.04	15.77	26.80
9H-2WR, 15.0–18.5	CKY-1810610	147.62	2,409	37,450	15,087	11,016	34.04	20.42	15.26	10.93	80.65	42.21	25.32	18.92	13.55
9H-5WR, 61.0–64.0	CKY-1835110	151.205	1,870	24,728	9,116	9,100	25.24	13.48	9.04	9.45	57.21	44.12	23.56	15.80	16.52
9H-7WR, 68.0–70.0	CKY-1836010	154.115	2,994	25,650	10,990	16,843	38.96	13.63	10.75	18.76	82.10	47.45	16.60	13.10	22.85
10H-8WR, 16.0–19.0	CKY-1815810	162.215	2,664	30,940	13,590	13,050	36.32	16.64	13.66	13.66	80.27	45.24	20.73	17.01	17.02
10H-9WR, 107.0–110.0	CKY-1836910	163.415	2,770	32,621	11,993	13,431	36.69	17.72	11.79	14.09	80.29	45.70	22.07	14.68	17.55
11H-5WR, 10.0–13.0	CKY-1837810	169.435	3,067	31,911	12,897	10,565	40.26	17.19	12.75	9.74	79.93	50.36	21.50	15.95	12.18
12H-2WR, 0.0–3.0	CKY-1824510	169.99	2,700	29,812	14,671	10,148	37.10	15.90	14.90	9.57	77.48	47.88	20.52	19.24	12.35
13T-3WR, 15.0–19.0	CKY-1825410	177.53	2,922	40,237	17,201	5,547	40.38	21.83	17.45	2.58	82.23	49.11	26.54	21.22	3.13
14T-2WR, 15.0–19.0	CKY-1828310	186.55	2,875	41,796	17,663	2,614	39.91	22.73	17.96	0.00	80.60	49.51	28.21	22.28	0.00

SVD = singular value decomposition.

Table T3. Mass transport deposits (MTDs), Hole C0021B.

MTD	Core, section, interval (cm)		Depth (mbsf)		Thickness (m)
	Top	Bottom	Top	Bottom	
A	338-C0021B- 3H-6, 8	338-C0021B- 5H-8, 6	94.16	116.75	22.59
B	7H-7, 106	13T-1, 66	133.76	176.16	42.4

Table T4. Results of XRF analysis, Hole C0021B.

Core, section, interval (cm)	Depth (mbsf)	Na_2O (wt%)	MgO (wt%)	Al_2O_3 (wt%)	SiO_2 (wt%)	P_2O_5 (wt%)	K_2O (wt%)	CaO (wt%)	TiO_2 (wt%)	MnO (wt%)	Fe_2O_3 (wt%)	Loss on ignition (wt%)
338-C0021B-												
1H-5, 0.0–3.0	3.760	3.12	2.26	14.1	58.0	0.11	2.72	10.5	0.59	0.06	5.28	11.6
1H-5, 118.5–120.5	4.945	3.01	2.24	14.0	58.9	0.11	2.59	11.7	0.56	0.07	5.08	12.6
1H-6, 20.0–23.0	5.165	2.76	2.33	14.3	57.1	0.11	2.53	12.3	0.59	0.07	5.31	12.5
2H-2, 24.0–27.0	80.395	2.60	2.07	13.4	55.3	0.12	2.06	16.9	0.55	0.09	4.82	15.2
2H-3, 15.0–18.0	81.710	2.88	2.18	14.6	58.0	0.10	2.77	11.3	0.57	0.08	5.43	11.8
3H-4, 15.0–18.0	91.820	3.87	0.80	13.1	71.5	0.05	2.45	3.58	0.34	0.07	2.99	5.91
3H-8, 85.0–88.0	96.930	2.79	2.27	15.5	60.8	0.11	2.96	7.15	0.62	0.08	5.60	9.25
4H-6, 15.0–19.0	105.065	2.70	2.43	16.4	60.5	0.11	3.10	6.42	0.69	0.08	5.68	8.66
4H-8, 32.0–35.0	108.090	2.69	2.28	15.3	58.8	0.12	2.81	7.84	0.67	0.08	6.38	9.00
5H-1, 57.0–60.0	109.070	2.83	2.33	14.9	58.3	0.11	2.67	10.2	0.62	0.08	5.94	10.9
5H-2, 0.0–4.0	109.810	2.65	2.16	14.4	56.4	0.11	2.57	11.4	0.61	0.09	6.23	10.5
6H-3, 15.0–18.0	119.660	2.63	2.24	15.4	60.8	0.11	3.02	7.60	0.67	0.07	5.54	9.23
6H-4, 0.0–2.5	119.800	2.87	2.15	15.6	61.6	0.12	2.99	6.51	0.65	0.07	5.34	8.50
7H-4, 0.0–3.0	129.860	3.00	2.39	15.8	62.1	0.10	3.08	5.06	0.69	0.07	5.80	7.76
8H-2, 15.0–18.0	138.110	2.74	2.22	14.5	58.2	0.11	2.54	11.4	0.61	0.08	5.48	11.5
9H-2, 15.0–18.5	147.620	2.76	2.37	15.6	60.9	0.10	2.97	7.06	0.67	0.07	5.93	9.27
9H-5, 61.0–64.0	151.205	2.75	2.37	15.0	59.3	0.11	2.77	7.49	0.67	0.07	6.74	8.92
9H-7, 68.0–70.0	154.115	2.71	2.06	14.9	58.2	0.12	2.65	11.4	0.59	0.08	5.20	11.5
10H-8, 16.0–19.0	162.215	2.74	2.30	15.3	59.9	0.12	2.79	8.76	0.65	0.08	5.75	10.4
10H-9, 107.0–110.0	163.415	2.65	2.21	15.3	60.2	0.12	2.75	9.15	0.65	0.08	5.31	10.6
11H-5, 10.0–13.0	169.435	2.68	2.35	15.8	60.9	0.12	2.92	7.18	0.69	0.09	6.04	9.59
12H-2, 0.0–3.0	169.990	2.80	2.20	15.8	60.4	0.13	2.70	7.36	0.71	0.09	5.84	9.29
13T-3, 15.0–19.0	177.530	2.66	2.28	16.3	63.6	0.10	3.09	3.77	0.71	0.08	5.71	7.52
14T-2, 15.0–19.0	186.550	2.65	2.44	16.8	63.7	0.10	2.96	2.53	0.80	0.11	6.36	6.92

Table T5. Calcareous nannofossils, Hole C0021B.

Age (Ma)	Core, section, interval (cm)	Average depth (mbsf)	Abundance	Preservation	*Calcidiscus leptoporus*	*Calciosolenia murrayi*	*Ceratolithus cristatus*	*Coccolithus pelagicus*	*Discoaster berggrenii*	*Discoaster brouweri*	*Discoaster quinqueramus*	*Discosphaera tubifera*	*Emiliania huxleyi*	*Florisphaera profunda*	*Gephyrocapsa* spp. large (>5.5 µm)	*Gephyrocapsa* spp. medium (4–5.5 µm)	*Gephyrocapsa* spp. small (<4 µm)	*Helicosphaera carteri*	*Helicosphaera inversa*	*Helicosphaera wallichii*	*Oolithotus antillarum*	*Pontosphaera japonica*	*Pontosphaera* spp.	*Pseudoemiliania lacunosa*	*Reticulofenestra asanoi*	*Reticulofenestra pseudoumbilicus*	*Reticulofenestra* spp. (<7 µm)	*Rhabdosphaera clavigera*	*Sphenolithus abies*	*Syracosphaera pulchra*	*Umbilicosphaera sibogae*
	338-C0021B-																														
<0.291	1H-CC, 25.5–30.5	5.88	V	G	+	+	+	+					+	+	+	+	+	+		+		+						+		+	+
0.436–0.903	2H-CC, 68.5–73.5	89.48	V	G	+			+						+	+	+	+	+					+	+				+		+	+
	3H-CC, 33.5–38.5	98.98	V	G	+		+	+			re	+		+	+	+	+	+				+	+	+				+		+	+
	4H-CC, 16.5–21.5	108.48	V	G	+		+	+						+	+	+	+	+				+		+				+		+	+
1.24–1.34	5H-1WR, 44.0–57.0	108.98	V	G	+	+		+						+	+	+	+	+		+		+	+	+		re	+	+	re	+	+
0.436–0.903	5H-CC, 11.0–16.0	117.98	V	G	+	+	+	+						+	+	+	+	+	+		+		+	+				+			+
	6H-CC, 44.0–49.0	127.48	V	G	+	+		+						+		+	+	+		+		+	+	+				+		+	+
	7H-CC, 20.0–-25.0	136.98	V	G	+		+	+						+	re	+	+	+					+	+				+		+	+
0.903–1.04	8H-CC, 28.0–33.0	146.48	A	G	+	+		+	re	re				+		+	+	+				+	+	+	+			+		+	+
	9H-CC, 25.5–30.5	154.98	V	G	+									+		+	+	+		+		+	+	+	+			+		+	+
1.07–1.24	10H-CC, 46.0–51.0	164.48	V	G	+			+						+			+	+				+	+	+		re	+	+			+
1.04–1.107	11H-CC, 31.5–36.5	169.49	V	G	+									+			+	+			+	+	+	+	+		+	+		+	+
0.903–1.04	12H-CC, 41.5–46.5	175.17	V	G	+	+		+				+		+		+	+	+			+		+	+	+		+	+		+	+
1.24–1.34	13T-CC, 25.5–30.5	183.75	A	G	+			+						+	+	+	+	+				+	+	+				+			+
	14T-CC, 29.5–34.5	194.48	V	G	+									+	+	+	+	+		+		+	+	+				+		+	+

Abundance: V = very abundant, A = abundant. Preservation: G = good. re = reworked, + = present. Median numerical ages for last consistent occurrence and first consistent occurrence of *Reticulofenestra asanoi* and last occurrence of large *Gephyrocapsa* are shown.

Table T6. Planktonic foraminifers, Hole C0021B.

Age (Ma)	Core, section, interval (cm)	Average depth (mbsf)	Abundance	Preservation	*Globigerina bulloides*	*Globigerina falconensis*	*Globigerina umbilicata*	*Globigerinella calida*	*Globigerinella obesa*	*Globigerinella siphonifera*	*Globigerinita glutinata*	*Globigerinoides conglobatus*	*Globigerinoides ruber* (white)	*Globigerinoides sacculifer*	*Globoconella inflata* modern form	*Globoconella inflata* transitional form	*Globoconella puncticulata*	*Globorotalia tumida*	*Globorotaloides variabilis*	*Globoturborotalita decoraperta*	*Globoturborotalita obliquus*	*Globoturborotalita rubescens*	*Globoturborotalita tenella*	*Hirsutella scitula*	*Menardella menardii*	*Neogloboquadrina acostaensis* dextral form	*Neogloboquadrina cf. asanoi*	*Neogloboquadrina dutertrei*	*Neogloboquadrina humerosa*	*Neogloboquadrina incompta*	*Neogloboquadrina inglei*	*Neogloboquadrina pachyderma* dextral form	*Neogloboquadrina pachyderma* sinistral form	*Neogloboquadrina praehumerosa*	*Orbulina suturalis*	*Orbulina universa*	*Pulleniatina finalis*	*Pulleniatina obliquiloculata* dextral form	*Pulleniatina obliquiloculata* sinistral form	*Sphaeroidinella dehiscens*	*Truncorotalia crassaformis*	*Truncorotalia tosaensis*	*Truncorotalia truncatulinoides*	*Turborotalita quinqueloba*
	338-C0021B-																																									
	1H-CC, 25.5–30.5	5.88	V	VG	+	+				+	+	+	+	+	+	+	+							+	+				+					+								
	2H-CC, 68.5–73.5	89.48	V	G	+	+		+		+	+	+	+	+	+	+		+						+	+									+							
<0.61	3H-CC, 33.5–38.5	98.98	V	M	+	+				+	+	+	+	+	+	+	+							+	+				+					+							
>0.61	4H-CC, 16.5–21.5	108.48	A	M	+	+				+	+	+	+	+	+	+		+			re	+	+	+	+				+					+							
	5H-1WR, 44.0–57.0	108.98	V	VG	+	+					+	+	+	+	+	+		+		+			+	+	+				+					+							
	5H-CC, 11.0–16.0	117.98	V	VG	+	+				+	+	+	+	+	+	+		+				+		+	+	+			+					+							
	6H-CC, 44.0–49.0	127.48	V	VG	+	+				+	+	+	+	+	+	+		+				+			+				+					+							
	7H-CC, 20.0–25.0	136.98	A	M	+	+		+		+	+	+	+	+	+	+	+	+	+				+		+				+					+							
	8H-CC, 28.0–33.0	146.48	V	VG	+	+		+		+	+	+	+	+	+	+		+					+		+				+					+							
	9H-CC, 25.5–30.5	154.98	A	M	+	+		+			+		+	+	+	+	+	+				+			+				+					+							
	10H-CC, 46.0–51.0	164.48	V	VG	+	+			+	+	+	+	+	+	+	+	+	+		+		+		+	+		+		+					+							
	11H-CC, 31.5–36.5	169.49	V	VG	+	+				+	+	+	+	+	+	+		+		+		+		+	+				+					+							
	12H-CC, 41.5–46.5	175.17	V	VG	+	+				+	+	+	+	+	+	+	+	+				+		+	+	+			+					+							
<1.3	13T-CC, 25.5–30.5	183.75	R	P	+	+					+		+	+	+	+	+								+				+					+							
>1.3	14T-CC, 29.5–34.5	194.48	C	P	+	+	+			+	+		+	+	+	+	+	+			+		+		+			+	+					+							

Abundance: V = very abundant, A = abundant, C = common, R = rare. Preservation: VG = very good, G = good, M = moderate, P = poor. re = reworked, + = present.

Table T7. Geochemistry of interstitial water in sediments sampled from Hole C0021B.

Core, section, interval (cm)	Depth (mbsf)	Salinity (refractive index)*	pH	Alkalinity (mM)	Chlorinity (mM)	Br^- (mM)	SO_4^{2-} (mM)	PO_4^{3-} (µM)	NH_4^+ (mM)	Na^+ (mM)	K^+ (mM)	Mg^{2+} (mM)	Ca^{2+} (mM)	Li (µM)	B (µM)	Mn (µM)
338-C0021B-																
1H-4	3.7	1.33930	8.01	9.5	554.3	0.82	18.6	28.6	0.16	475	12.1	49.0	7.6	35.0	535	1.1
2H-3	81.6	1.33892	7.78	26.8	545.6	0.95	1.3	82.2	4.99	496	10.8	32.2	2.3	30.5	421	2.8
3H-4	91.7	1.33887	7.79	26.3	541.7	0.94	1.4	82.9	5.14	493	10.2	31.1	2.8	32.9	388	4.5
4H-6	104.9	1.33889	7.80	25.5	545.8	0.97	1.0	61.2	5.50	503	10.7	29.1	3.1	35.8	391	4.3
5H-2	109.9	1.33888	7.80	24.6	544.1	0.97	1.0	61.4	5.65	499	10.4	28.4	3.1	34.8	376	4.3
6H-3	119.5	1.33886	7.84	22.6	545.7	0.98	1.0	56.3	5.91	492	9.6	26.5	3.3	36.5	357	3.9
7H-4	129.9	1.33887	7.84	22.6	544.9	0.97	1.1	50.7	6.15	502	9.5	26.3	3.8	37.6	342	3.9
8H-2	138.0	1.33885	7.88	20.8	545.4	0.98	1.1	38.1	6.42	508	9.7	25.5	3.5	40.5	335	3.1
9H-2	147.5	1.33885	7.85	19.2	548.7	1.05	1.0	30.1	6.70	499	9.7	23.9	3.7	41.2	299	2.5
10H-8	162.1	1.33884	7.80	16.8	549.3	0.95	0.9	26.4	6.96	494	10.4	22.4	3.7	42.3	297	1.6
12H-2	170.0	1.33885	7.71	18.7	549.7	0.94	1.3	48.2	6.88	501	8.9	23.3	5.0	41.1	328	2.6
13T-3	177.4	1.33887	7.91	19.0	547.6	1.00	1.4	57.4	6.82	506	9.1	23.3	5.5	40.1	321	2.8
14T-2	186.4	1.33886	7.73	17.3	546.5	1.01	2.4	73.9	6.87	501	8.9	23.9	6.0	38.3	321	3.7

* = data not corrected.

Core, section, interval (cm)	Depth (mbsf)	Fe (µM)	Si (µM)	Sr (µM)	Ba (µM)	V (nM)	Cu (nM)	Zn (nM)	Rb (nM)	Mo (nM)	Cs (nM)	Pb (nM)	U (nM)
338-C0021B-													
1H-4	3.7	2.78	783	83.3	1.0	39.5	35	600	1,609	3	3.10	0.46	2.44
2H-3	81.6	4.86	863	84.6	98.9	27.5	2,976	1,388	1,223	48	4.74	0.17	2.15
3H-4	91.7	3.37	727	84.6	93.5	23.1	785	486	1,171	21	5.21	0.12	1.09
4H-6	104.9	5.85	837	86.7	89.6	24.4	1,754	552	1,197	18	5.57	0.13	1.06
5H-2	109.9	6.06	845	85.3	87.3	21.6	2,466	419	1,112	34	4.62	0.15	2.08
6H-3	119.5	3.37	804	85.3	83.9	23.3	503	331	1,130	15	5.45	0.10	1.68
7H-4	129.9	5.25	876	86.8	79.0	18.0	363	499	1,085	27	5.08	0.00	0.82
8H-2	138.0	5.83	857	83.8	75.6	21.5	1,463	509	1,064	65	4.74	0.16	1.97
9H-2	147.5	1.56	747	85.1	69.5	19.8	327	408	1,075	43	4.90	0.00	2.66
10H-8	162.1	1.68	809	81.7	60.4	24.8	1,164	384	1,060	217	5.23	0.37	2.73
12H-2	170.0	3.58	933	88.7	52.7	16.2	618	336	921	27	3.96	0.00	0.73
13T-3	177.4	1.48	841	90.9	49.3	24.1	141	339	945	136	4.48	0.30	2.30
14T-2	186.4	3.34	722	90.9	41.6	17.1	80	264	914	88	4.11	0.00	1.37

Table T8. Core liner liquid geochemistry, Hole C0021B.

Core, section	Depth (mbsf)	Salinity (refractive index)*	pH	Alkalinity (mM)	Chlorinity (mM)	PO_4^{3-} (µM)	NH_4^+ (mM)	Br^- (mM)	SO_4^{2-} (mM)	Na^+ (mM)	K^+ (mM)	Mg^{2+} (mM)	Ca^{2+} (mM)	Li (µM)	B (µM)	Mn (µM)
338-C0021B-																
1H-1	0.0	1.33943	7.49	2.21	552.2	0.0	0.0	0.84	26.4	485	10.9	54.4	10.7	35.3	432	2.3
13T-5	179.4	1.33931	7.62	5.79	551.5	20.0	3.7	0.85	20.4	481	9.5	44.0	8.8	36.7	396	11.9

* = data not corrected.

Table T9. Hydrocarbon gas composition in extracted headspace gas by oven-heating gas extraction, Hole C0021B.

Core, section, interval (cm)	Depth (mbsf)	Headspace gas (ppmv)				Headspace gas (μM)			δ^{13}C-CH$_4$ (‰ VPDB)
		Methane	Ethane	Propane	$C_1/(C_2 + C_3)$	Methane	Ethane	Propane	
338-C0021B-									
1H-3, 79.5–83.5	3.6	34	0.2	ND	142.6	0.01	0.04	ND	—
2H-2, 136.5–140.5	81.5	6,224	1.7	0.3	3,210	1.78	0.47	0.08	–71.3
3H-5, 0–4	92.0	6,645	2.3	0.3	2,487	1.84	0.65	0.09	–69.7
4H-1, 136.5–140.5	100.4	8,153	2.2	ND	3,752	2.71	0.72	ND	–71.9
5H-1, 127–131	109.8	5,311	2.6	0.3	1,831	1.15	0.56	0.07	–71.7
6H-2, 122–126	119.5	7,532	3.2	ND	2,323	2.26	0.97	ND	–72.2
7H-5, 0–4	130.1	10,554	5.3	0.3	1,901	2.07	1.04	0.05	–73.1
8H-1, 92–96	137.9	10,593	6.6	0.3	1,523	2.17	1.36	0.06	–72.5
9H-1, 93–97	147.4	14,653	10.6	0.3	1,338	2.85	2.06	0.07	–73.5
10H-7, 28.5–32.5	162.0	8,507	6.1	ND	1,400	2.05	1.47	ND	–72.2
13T-2, 44–48	177.3	6,028	15.6	0.4	376	0.75	1.94	0.05	–70.5
14T-1, 136–140	186.4	3,473	12.1	ND	286	1.15	4.03	ND	–68.0

ND = not detected. — = not enough methane to measure δ^{13}C-CH$_4$. VPDB = Vienna Peedee belemnite.

Table T10. Hydrocarbon gas composition in extracted headspace gas by NaOH-addition gas extraction, Hole C0021B.

Core, section, interval (cm)	Depth (mbsf)	Headspace gas (ppmv)				Headspace gas (μM)			δ^{13}C-CH$_4$ (‰ VPDB)
		Methane	Ethane	Propane	$C_1/(C_2 + C_3)$	Methane	Ethane	Propane	
338-C0021B-									
1H-3, 79.5–83.5	3.6	46	0.4	ND	124	0.01	0.06	ND	—
2H-2, 136.5–140.5	81.5	10,489	2.0	ND	5,246	2.15	0.41	ND	–74.5
3H-5, 0–4	92.0	10,495	2.7	ND	3,927	2.21	0.56	ND	–73.3
4H-1, 136.5–140.5	100.4	11,757	2.6	ND	4,525	2.83	0.63	ND	–73.1
5H-1, 127–131	109.8	5,898	2.2	ND	2,650	1.00	0.38	ND	–71.1
6H-2, 122–126	119.5	11,108	4.3	ND	2,579	2.32	0.90	ND	–72.7
7H-5, 0–4	130.1	7,977	4.0	ND	1,971	0.92	0.46	ND	–71.2
8H-1, 92–96	137.9	9,202	5.2	ND	1,759	1.07	0.61	ND	–71.1
9H-1, 93–97	147.4	9,174	9.3	0.3	957	1.32	1.34	0.043	–70.6
10H-7, 28.5–32.5	162.0	6,611	5.0	ND	1,329	1.29	0.97	ND	–71.7
13T-2, 44–48	177.3	6,436	12.0	ND	535	0.69	1.29	ND	–70.6
14T-1, 136–140	186.4	7,631	18.8	ND	405	1.71	4.22	ND	–70.3

ND = not detected. — = not enough methane to measure δ^{13}C-CH$_4$. VPDB = Vienna Peedee belemnite.

Table T11. Hydrocarbon gas composition in the void gas, Hole C0021B.

Core, section, interval (cm)	Depth (mbsf)	Headspace gas (ppmv)			$C_1/(C_2 + C_3)$	δ^{13}C-CH$_4$ (‰ VPDB)
		Methane	Ethane	Propane		
338-C0021B-						
1H-1, 0	0.0	616	0.2	ND	4,088	—
2H-7, 10	84.7	232,208	75.8	ND	3,065	–76.0
3H-5, 36.5	92.3	218,181	22.7	0.7	9,334	–73.1
4H-3, 22.5	100.8	217,486	23.6	0.7	8,939	–73.7
5H-7, 71.5	116.4	202,735	83.5	ND	2,429	–74.5
6H-5, 48	121.7	230,268	79.0	ND	2,914	–74.9
7H-5, 85	130.9	206,510	32.8	0.2	6,268	–74.7
8H-8, 94	146.3	328,881	66.5	ND	4,947	–72.9
9H-1, 41	146.9	254,492	81.0	0.6	3,119	–74.3
10H-9, 109	163.4	127,616	39.7	0.2	3,197	–74.4
13T-6, 16	180.4	193,182	114.7	ND	1,685	–74.4
14T-3, 102	187.7	216,877	204.9	0.1	1,058	–73.7

ND = not detected. — = not enough methane to measure δ^{13}C-CH$_4$. VPDB = Vienna Peedee belemnite.

Table T12. Organic and inorganic carbon, nitrogen, and sulfur in sediment, Hole C0021B.

Core, section, interval (cm)	Depth (mbsf)	IC (wt%)	$CaCO_3$ (wt%)	TN (wt%)	TC (wt%)	TS (wt%)	TOC (wt%)	TOC/TN	TOC/TS
338-C0021B-									
1H-5, 0.0	3.8	1.80	15.0	0.09	2.6	0.54	0.76	8.4	1.40
1H-5, 118.5	4.9	1.99	16.6	0.09	2.7	0.33	0.70	8.1	2.14
1H-6, 20.0	5.2	2.09	17.4	0.09	2.7	0.34	0.65	7.4	1.88
2H-2, 24.0	80.4	2.83	23.6	0.06	3.3	0.09	0.46	7.2	5.05
2H-3, 15.0	81.7	1.97	16.4	0.07	2.4	0.22	0.48	7.0	2.14
3H-4, 15.0	91.8	0.35	2.9	0.02	0.5	0.32	0.12	6.2	0.39
3H-8, 85.0	96.9	1.16	9.7	0.07	1.7	0.26	0.52	7.3	2.01
4H-6, 15.0	105.1	1.10	9.2	0.06	1.5	0.30	0.40	6.3	1.33
4H-8, 32.0	108.1	1.36	11.3	0.07	1.8	0.51	0.46	6.6	0.89
5H-1, 57.0	109.1	1.77	14.7	0.06	2.1	0.26	0.34	5.7	1.29
5H-2, 0.0	109.8	1.96	16.3	0.06	2.3	0.86	0.31	5.3	0.36
6H-3, 15.0	119.7	1.29	10.8	0.06	1.7	0.27	0.38	6.1	1.40
6H-4, 0.0	119.8	1.10	9.1	0.06	1.5	0.34	0.44	7.1	1.31
7H-4, 0.0	129.9	0.80	6.7	0.07	1.3	0.16	0.46	6.2	2.89
8H-2, 15.0	138.1	1.84	15.3	0.07	2.3	0.14	0.49	6.9	3.49
9H-2, 15.0	147.6	1.19	9.9	0.07	1.7	0.30	0.51	7.0	1.68
9H-5, 61.0	151.2	1.29	10.8	0.09	1.8	1.02	0.50	5.7	0.49
9H-7, 68.0	154.1	1.98	16.5	0.07	2.3	0.27	0.33	5.0	1.23
10H-8, 16.0	162.2	1.50	12.5	0.07	2.0	0.18	0.45	6.3	2.46
10H-9, 107.0	163.4	1.61	13.4	0.08	2.1	0.12	0.45	5.9	3.90
11H-5, 10.0	169.4	1.28	10.7	0.08	1.7	0.11	0.43	5.5	3.75
12H-2, 0.0	170.0	1.16	9.7	0.07	1.7	0.21	0.53	7.1	2.48
13T-3, 15.0	177.5	0.63	5.3	0.07	1.2	0.15	0.52	7.2	3.47
14T-2, 15.0	186.6	0.49	4.1	0.07	1.0	0.09	0.51	7.7	5.46

IC = inorganic carbon, TN = total nitrogen, TC = total carbon, TS = total sulfur, TOC = total organic carbon.

Table T13. Moisture and density measurements, Site C0021. (Continued on next page.)

Core, section, interval (cm)	Depth (mbsf)	Density (g/cm^3)		Porosity (%)	Void ratio	Notes
		Bulk	Grain			
338-C0021B-						
1H-1, 120.0	1.20	1.43	2.59	74.42	2.91	
1H-2, 35.0	1.76	1.43	2.63	74.78	2.97	
1H-2, 121.0	2.62	1.49	2.63	70.76	2.42	
1H-3, 31.0	3.13	1.52	2.62	68.86	2.21	
1H-5, 0.0	3.76	1.51	2.62	69.41	2.27	
1H-5, 118.5	4.95	1.51	2.64	70.02	2.34	
2H-2, 24.0	80.40	1.61	2.66	64.40	1.81	
2H-2, 115.0	81.31	1.58	2.63	65.37	1.89	
2H-4, 17.0	82.01	1.59	2.62	64.89	1.85	
2H-4, 115.0	82.99	1.59	2.60	64.18	1.79	
2H-5, 49.0	83.71	1.54	2.56	66.18	1.96	
2H-6, 24.0	84.34	1.54	2.60	67.06	2.04	
2H-7, 41.0	85.00	1.55	2.65	67.62	2.09	
2H-7, 111.0	85.70	1.57	2.63	66.11	1.95	
2H-8, 17.0	86.16	1.58	2.65	65.98	1.94	
2H-8, 115.0	87.14	1.61	2.62	63.20	1.72	
2H-9, 21.0	87.60	1.61	2.59	62.80	1.69	
2H-10, 12.0	88.53	1.58	2.63	65.58	1.91	
2H-10, 117.0	89.58	1.61	2.58	62.62	1.68	
3H-1, 35.5	89.86	1.61	2.64	63.93	1.77	
3H-2, 35.0	90.61	1.58	2.64	65.52	1.90	
3H-3, 14.5	90.87	1.60	2.64	64.18	1.79	
3H-3, 87.5	91.60	1.65	2.66	61.63	1.61	
3H-5, 16.0	92.12	1.60	2.65	64.54	1.82	
3H-5, 23.0	92.19	1.66	2.66	61.20	1.58	
3H-6, 44.0	93.77	1.58	2.65	65.85	1.93	
3H-6, 131.0	94.64	1.68	2.64	59.28	1.46	
3H-7, 43.0	95.17	1.65	2.65	61.25	1.58	
3H-7, 118.0	95.92	1.62	2.59	61.97	1.63	
3H-8, 36.0	96.44	1.66	2.62	59.78	1.49	
3H-8, 85.0	96.93	1.65	2.64	61.03	1.57	
3H-9, 49.0	97.86	1.69	2.69	60.19	1.51	
3H-10, 40.0	98.65	1.66	2.63	60.60	1.54	
4H-1, 28.0	99.28	1.66	2.65	60.73	1.55	
4H-1, 83.0	99.83	1.67	2.62	59.68	1.48	
4H-3, 24.0	100.85	1.66	2.69	62.04	1.63	
4H-3, 105.0	101.66	1.64	2.66	62.38	1.66	
4H-4, 38.0	102.40	1.72	2.70	58.63	1.42	
4H-4, 105.0	103.07	1.69	2.68	59.91	1.49	
4H-5, 40.0	103.86	1.70	2.67	58.99	1.44	
4H-5, 100.0	104.46	1.71	2.61	56.56	1.30	
4H-6, 15.0	105.07	1.75	2.76	58.05	1.38	
4H-6, 53.0	105.45	1.71	2.66	57.80	1.37	
4H-6, 109.0	106.01	1.69	2.65	59.07	1.44	
4H-7, 16.0	106.52	1.73	2.70	57.99	1.38	
4H-7, 117.0	107.53	1.75	2.66	55.35	1.24	
4H-8, 32.0	108.09	1.73	2.73	58.62	1.42	
5H-1, 57.0	109.07	1.68	2.82	63.49	1.74	
5H-2, 0.0	109.81	1.71	2.72	59.51	1.47	
5H-3, 131.0	111.42	1.70	2.67	59.14	1.45	
5H-4, 20.0	111.72	1.62	2.65	63.51	1.74	
5H-5, 28.0	113.20	1.67	2.64	59.94	1.50	
5H-6, 72.0	115.03	1.71	2.65	57.97	1.38	
5H-7, 57.0	116.29	1.94	2.66	44.42	0.80	Sand
5H-8, 18.0	116.87	1.72	2.67	57.86	1.37	
5H-9, 65.0	118.05	1.69	2.66	59.19	1.45	
6H-2, 64.0	118.89	1.69	2.67	59.42	1.46	
6H-3, 15.0	119.66	1.75	2.70	56.80	1.31	
6H-4, 0.0	119.80	1.74	2.69	57.10	1.33	
6H-5, 84.0	122.05	1.73	2.68	57.20	1.34	
6H-6, 39.0	123.00	1.71	2.66	58.44	1.41	
6H-7, 80.0	124.83	1.77	2.72	55.88	1.27	
6H-8, 38.0	125.82	1.70	2.58	56.95	1.32	
6H-9, 81.0	127.61	1.68	2.60	58.74	1.42	
7H-2, 19.0	128.35	1.65	2.63	60.97	1.56	
7H-4, 0.0	129.86	1.71	2.80	61.44	1.59	
7H-5, 15.0	130.20	1.66	2.66	61.45	1.59	

Table T13 (continued).

Core, section, interval (cm)	Depth (mbsf)	Density (g/cm³)		Porosity (%)	Void ratio	Notes
		Bulk	Grain			
7H-6, 32.5	131.75	1.66	2.67	61.45	1.59	
7H-7, 131.0	134.01	1.68	2.64	59.77	1.49	
7H-8, 113.0	135.31	1.73	2.69	57.67	1.36	
7H-9, 43.0	136.09	1.73	2.68	57.37	1.35	
7H-10, 25.0	137.00	1.73	2.69	57.33	1.34	
8H-2, 15.0	138.11	1.65	2.67	62.21	1.65	
8H-3, 44.0	138.68	1.68	2.66	59.82	1.49	
8H-4, 106.0	140.72	1.62	2.65	63.12	1.71	
8H-5, 102.0	142.09	1.64	2.66	62.32	1.65	
8H-6, 120.0	143.73	1.93	2.69	45.59	0.84	Sand
8H-7, 125.0	145.18	1.83	2.71	51.90	1.08	
8H-8, 62.0	145.95	1.76	2.67	55.49	1.25	
9H-1, 72.0	147.22	1.71	2.70	59.20	1.45	
9H-2, 15.0	147.62	1.73	2.80	60.19	1.51	
9H-3, 81.0	148.57	1.77	2.72	56.30	1.29	
9H-4, 131.0	150.50	1.74	2.60	54.49	1.20	Ash
9H-5, 61.0	151.21	1.75	2.82	59.58	1.47	
9H-6, 120.0	153.23	1.71	2.74	60.09	1.51	
9H-7, 68.0	154.12	1.76	2.77	57.72	1.37	
9H-8, 61.0	155.46	1.76	2.68	55.78	1.26	
10H-1, 51.0	155.51	1.68	2.70	60.72	1.55	
10H-2, 31.0	155.96	1.73	2.55	53.81	1.17	Ash
10H-3, 46.0	157.52	1.78	2.66	53.69	1.16	
10H-4, 37.0	158.82	1.77	2.68	55.11	1.23	
10H-5, 43.0	160.07	1.74	2.68	57.01	1.33	
10H-6, 65.0	161.04	1.73	2.66	57.05	1.33	
10H-8, 16.0	162.22	1.74	2.75	58.68	1.42	
10H-9, 107.0	163.42	1.76	2.77	57.61	1.36	
10H-10, 41.0	164.17	1.76	2.73	56.98	1.32	
11H-1, 117.0	165.67	1.82	2.70	52.79	1.12	
11H-2, 10.0	165.88	2.07	2.69	37.37	0.60	Sand
11H-3, 39.0	167.57	1.88	2.71	49.24	0.97	
11H-5, 10.0	169.44	1.79	2.71	54.86	1.22	
12H-1, 32.0	169.82	1.72	2.67	57.59	1.36	
12H-2, 0.0	169.99	1.74	2.74	58.40	1.40	
12H-3, 71.0	170.90	1.75	2.65	55.33	1.24	
11H-6, 51.0	171.31	1.77	2.67	54.43	1.19	
12H-4, 5.0	171.66	1.69	2.65	58.81	1.43	
13T-1, 118.0	176.68	1.79	2.67	53.42	1.15	
13T-3, 15.0	177.53	1.38	2.02	64.44	1.81	
13T-4, 110.0	178.67	1.75	2.68	56.40	1.29	
13T-5, 15.0	179.12	1.99	2.70	42.46	0.74	Sandy
13T-6, 33.0	180.52	1.84	2.71	51.70	1.07	
13T-6, 76.0	180.95	1.93	2.67	45.09	0.82	Sand
13T-7, 51.0	182.01	1.82	2.67	51.85	1.08	
13T-8, 88.0	183.32	1.87	2.71	49.75	0.99	
14T-1, 61.0	185.61	1.75	2.68	56.11	1.28	
14T-2, 15.0	186.55	1.86	2.68	49.64	0.99	
14T-3, 15.0	186.84	1.92	2.68	45.78	0.84	Sand
14T-3, 78.0	187.47	1.83	2.75	53.59	1.15	
14T-4, 101.0	189.17	1.82	2.78	54.66	1.21	
14T-5, 69.0	190.28	1.83	2.72	52.34	1.10	
14T-6, 50.0	191.50	1.82	2.72	52.90	1.12	
14T-7, 31.0	192.79	1.77	2.67	54.52	1.20	
14T-8, 115.0	194.17	1.79	2.66	53.09	1.13	

Table T14. Electrical resistivity measurements, Site C0021. (Continued on next page.)

Core, section, interval (cm)	Depth (mbsf)	Electrical resistivity (Ωm)	Notes
338-C0021B-			
1H-1, 125.0	1.25	0.392	Mud
1H-2, 95.0	2.36	0.587	Mud
1H-2, 118.0	2.59	0.606	Mud
1H-2, 25.0	1.66	0.551	Mud
1H-2, 10.0	1.51	0.532	Mud
1H-3, 69.0	3.51	0.713	Mud
1H-3, 26.0	3.08	0.626	Mud
1H-5, 72.0	4.48	0.603	Mud
1H-5, 106.0	4.82	0.634	Mud
1H-5, 10.0	3.86	0.58	Mud
1H-5, 33.0	4.09	0.599	Mud
1H-6, 36.0	5.33	0.651	Mud
1H-6, 53.0	5.50	0.628	Mud
2H-2, 103.0	81.19	0.962	Mud
2H-2, 133.0	81.49	0.86	Mud
2H-2, 40.0	80.56	0.909	Mud
2H-2, 57.0	80.73	0.892	Mud
2H-4, 83.0	82.67	0.915	Mud
2H-4, 103.0	82.87	0.898	Mud
2H-4, 125.0	83.09	0.851	Mud
2H-4, 40.0	82.24	0.995	Mud
2H-4, 8.0	81.92	0.972	Mud
2H-5, 81.0	84.03	0.849	Mud
2H-5, 80.0	83.82	0.844	Mud
2H-6, 18.0	84.28	0.81	Mud
2H-7, 86.0	85.45	0.888	Mud
2H-7, 127.0	85.86	0.809	Mud
2H-8, 111.0	87.10	0.855	Mud
2H-8, 96.0	86.95	1.05	Mud
2H-8, 35.0	86.31	0.774	Mud
2H-8, 98.0	88.37	1.044	Mud
2H-10, 99.0	89.40	0.913	Mud
3H-1, 72.0	90.22	0.592	Mud
3H-1, 92.0	90.42	0.624	Mud
3H-2, 39.0	90.65	0.671	Mud
3H-3, 86.0	91.58	0.678	Mud
3H-1, 24.0	90.96	0.633	Mud
3H-5, 114.0	93.10	0.68	Mud
3H-5, 33.0	92.29	0.629	Mud
3H-6, 95.0	94.28	0.781	Mud
3H-6, 139.0	94.72	0.977	Mud
3H-6, 41.0	93.74	0.735	Mud
3H-7, 117.0	95.91	0.974	Mud
3H-7, 30.0	95.04	0.841	Mud
3H-7, 9.0	94.83	0.789	Mud
3H-8, 82.0	96.90	0.793	Mud
3H-9, 82.0	98.19	1.28	Mud
3H-9, 69.0	98.06	1.118	Mud
3H-10, 62.0	98.87	0.943	Mud
4H-1, 40.0	99.40	0.684	Mud
4H-3, 104.0	101.65	0.725	Mud
4H-3, 36.0	100.97	0.704	Mud
4H-3, 3.0	100.64	0.642	Mud
4H-4, 110.0	103.12	0.798	Mud
4H-4, 36.0	102.38	0.831	Mud
4H-4, 52.0	102.54	1.08	Mud
4H-5, 108.0	104.54	0.76	Mud
4H-5, 129.0	104.75	1.019	Mud
4H-5, 38.0	103.84	0.8	Mud
4H-5, 48.0	103.94	0.814	Mud
4H-6, 107.0	105.99	0.797	Mud
4H-6, 84.0	105.76	0.938	Mud
4H-6, 48.0	105.40	0.833	Mud
4H-7, 101.0	107.37	1.235	Mud
4H-7, 42.0	106.78	1.148	Mud
5H-1, 39.0	108.89	0.532	Mud
5H-3, 127.0	111.38	0.789	Mud
5H-3, 36.0	110.47	0.998	Mud
5H-4, 106.0	112.58	0.681	Mud
5H-4, 12.0	111.64	0.776	Mud
5H-5, 105.0	113.97	0.91	Mud
5H-5, 51.0	113.43	0.703	Mud
5H-6, 93.0	115.24	0.899	Mud
5H-7, 86.0	116.58	0.864	Mud
5H-8, 68.0	117.37	0.946	Mud
5H-9, 77.0	118.17	0.895	Mud
6H-2, 110.0	119.35	0.82	Mud
6H-2, 18.0	118.43	0.766	Mud
6H-4, 118.0	120.98	0.81	Mud
6H-4, 43.0	120.23	0.787	Mud
6H-5, 104.0	122.25	0.775	Mud
6H-5, 21.0	121.42	0.812	Mud
6H-5, 4.0	121.25	0.771	Mud
6H-6, 118.0	123.79	0.722	Mud
6H-6, 91.0	123.52	0.823	Mud
6H-6, 18.0	122.79	0.801	Mud
6H-7, 45.0	124.48	0.815	Mud
6H-7, 108.0	125.11	0.969	Mud
6H-7, 87.0	124.90	0.81	Mud
6H-7, 15.0	124.18	0.721	Mud
6H-8, 46.0	125.90	0.758	Mud
6H-8, 106.0	126.50	0.866	Mud
6H-8, 13.0	125.57	0.752	Mud
6H-9, 55.0	127.35	0.89	Mud
6H-9, 107.0	127.87	0.738	Mud
6H-9, 18.0	126.98	0.731	Mud
7H-1, 57.0	128.07	0.744	Mud
7H-3, 35.0	129.80	0.779	Mud
7H-5, 123.0	131.28	0.814	Mud
7H-5, 95.0	131.00	1.044	Mud
7H-5, 40.0	130.45	0.816	Mud
7H-6, 111.0	132.53	1.08	Sandy
7H-6, 84.0	132.26	1.038	Mud
7H-6, 30.0	131.72	0.897	Mud
7H-8, 97.0	135.15	1.054	Mud
7H-8, 80.0	134.98	1.075	Mud
7H-8, 37.0	134.55	1.036	Mud
7H-9, 95.0	136.61	0.942	Mud
7H-9, 25.0	135.91	0.955	Mud
7H-10, 60.0	137.35	1.118	Mud
7H-10, 11.0	136.86	1.1	Mud
7H-10, 46.0	137.21	1.201	Mud
8H-3, 106.0	139.30	0.806	Mud
8H-3, 50.0	138.74	0.817	Mud
8H-1, 85.0	137.85	0.733	Mud
8H-4, 102.0	140.68	0.825	Mud
8H-4, 131.0	140.97	0.821	Mud
8H-4, 31.0	139.97	0.865	Mud
8H-5, 87.0	141.94	0.769	Mud
8H-5, 136.0	142.43	0.834	Mud
8H-5, 9.0	141.16	1.48	Mud
8H-5, 41.0	141.48	0.847	Mud
8H-6, 131.0	143.84	1.077	Mud
8H-6, 93.0	143.46	0.917	Mud
8H-6, 30.0	142.83	0.843	Mud
8H-6, 9.0	142.62	0.905	Mud
8H-7, 132.0	145.25	1.636	Mud
8H-7, 111.0	145.04	5.272	Mud
8H-7, 122.0	145.15	3.995	Sandy
8H-7, 18.0	144.11	0.939	Sandy
8H-8, 108.0	146.41	1.196	Mud
8H-8, 87.0	146.20	1.176	Mud
8H-8, 20.0	145.53	1.053	Mud
8H-8, 46.0	145.79	1.362	Sandy
9H-1, 84.0	147.34	1.011	Mud

Table T14 (continued).

Core, section, interval (cm)	Depth (mbsf)	Electrical resistivity (Ωm)	Notes
9H-3, 98.0	148.74	0.988	Mud
9H-3, 34.0	148.10	0.968	Mud
9H-3, 5.0	147.81	1.092	Mud
9H-4, 116.0	150.35	0.968	Mud
9H-4, 87.0	150.06	2.353	Ash
9H-4, 34.0	149.53	0.892	Mud
9H-4, 96.0	150.15	1.856	Ash
9H-5, 139.0	151.99	1.062	Mud
9H-5, 125.0	151.85	1.854	Mud
9H-6, 86.0	152.89	0.916	Ash
9H-6, 30.0	152.33	2.947	Mud
9H-7, 65.0	154.09	1.182	Mud
9H-7, 46.0	153.90	3.935	Mud
9H-8, 121.0	156.06	0.875	Mud
9H-8, 38.0	155.23	1.318	Mud
10H-1, 13.0	155.13	0.801	Mud
10H-2, 99.0	156.64	1.212	Mud
10H-2, 33.0	155.98	1.71	Ash
10H-3, 88.0	157.94	0.995	Mud
10H-4, 47.0	158.92	4.65	Mud
10H-4, 80.0	159.25	0.997	Mud
10H-6, 83.0	161.22	1.202	Mud
10H-9, 78.0	163.13	1.239	Mud
10H-10, 53.0	164.29	1.306	Mud
11H-1, 100.0	165.50	0.88	Mud
11H-2, 97.0	166.75	0.872	Mud
11H-3, 93.0	168.11	0.837	Mud
11H-5, 111.0	170.45	0.917	Mud
11H-6, 96.0	171.76	0.806	Mud
12H-1, 28.0	169.78	1.042	Mud
12H-3, 93.0	171.12	0.934	Mud
12H-4, 46.0	172.07	0.893	Mud
13T-1, 101.0	176.51	0.839	Mud
13T-1, 46.0	175.96	0.833	Mud
13T-4, 97.0	178.54	0.956	Mud
13T-4, 138.0	178.95	1.656	Sand
13T-4, 6.0	177.63	1.482	Sandy
13T-4, 40.0	177.97	0.888	Mud
13T-5, 18.0	179.15	1.78	Sand
13T-5, 66.0	179.63	0.837	Mud
13T-6, 105.0	181.24	0.975	Mud
13T-6, 86.0	181.05	1.419	Sand
13T-6, 60.0	180.79	0.934	Mud
13T-6, 29.0	180.48	1.606	Sand
13T-7, 79.0	182.29	1.25	Ash
13T-7, 76.0	182.26	1.374	Sand
13T-7, 70.0	182.20	0.896	Mud
13T-8, 76.0	183.20	1.098	Mud
13T-8, 83.0	183.27	1.371	Sand
14T-1, 92.0	185.92	0.859	Mud
14T-1, 108.0	186.08	0.929	Mud
14T-3, 88.0	187.57	0.862	Ash
14T-3, 121.0	187.90	1.063	Mud
14T-4, 113.0	189.29	1.064	Sand
14T-4, 121.0	189.37	0.995	Mud
14T-5, 115.0	190.74	0.959	Mud
14T-5, 102.0	190.61	1.039	Sand
14T-6, 77.0	191.77	1.343	Sand
14T-6, 87.0	191.87	0.962	Mud
14T-7, 44.0	192.92	1.682	Coarse sand
14T-8, 80.0	193.82	0.865	Mud
14T-8, 74.0	193.76	1.293	Sand

Table T15. Penetrometer and vane shear measurements, Hole C0021B. (Continued on next two pages.)

Core, section, interval (cm)	Depth (mbsf)	Undrained shear strength (kPa)	
		Penetrometer	Vane shear
338-C0021B-			
1H-1, 131.0	1.31		8.285
1H-1, 135.0	1.35	4.905	
1H-2, 30.0	1.71	6.54	
1H-2, 31.0	1.72		7.648
1H-2, 90.0	2.31		12.747
1H-2, 90.0	2.31	12.263	
1H-3, 58.0	3.395	18.803	
1H-3, 65.0	3.465		19.758
1H-5, 25.0	4.01	19.62	
1H-5, 27.0	4.03		8.354
1H-5, 88.0	4.64	28.613	
1H-5, 90.0	4.66		20.53
1H-6, 32.0	5.285	22.89	
1H-6, 33.5	5.3		12.1
2H-2, 43.0	80.585	81.75	
2H-2, 45.0	80.605		55.184
2H-2, 110.0	81.255		42.54
2H-2, 111.0	81.265	39.567	
2H-4, 24.0	82.08	57.225	
2H-4, 25.0	82.09		35.984
2H-4, 120.0	83.04		41.135
2H-4, 121.0	83.05	55.59	
2H-5, 25.0	83.47	61.313	
2H-5, 26.0	83.48		40.667
2H-6, 31.0	84.405	70.305	
2H-6, 33.0	84.425		43.476
2H-7, 36.0	84.945	53.955	
2H-7, 37.0	84.955		27.554
2H-7, 109.0	85.675		36.452
2H-7, 110.0	85.685	60.495	
2H-8, 29.0	86.275	89.925	
2H-8, 30.0	86.285		58.462
2H-8, 110.0	87.085		50.501
2H-8, 111.0	87.095	83.385	
2H-9, 50.0	87.89		48.159
2H-9, 50.0	87.89	80.115	
2H-10, 27.0	88.68	67.035	
2H-10, 28.0	88.69		50.969
2H-10, 100.0	89.41		55.184
2H-10, 102.0	89.43	80.115	
3H-1, 28.0	89.78	40.875	
3H-1, 30.0	89.8		34.345
3H-2, 30.5	90.56		35.515
3H-2, 33.0	90.585	58.043	
3H-3, 28.0	91	58.86	
3H-3, 30.5	91.025		31.301
3H-5, 29.5	92.25		57.525
3H-5, 31.0	92.265	85.02	
3H-5, 105.0	93.005		61.74
3H-5, 107.0	93.025	88.29	
3H-6, 46.0	93.785	75.21	
3H-6, 48.0	93.805		51.995
3H-6, 100.0	94.325		47.326
3H-6, 103.0	94.355	85.02	
3H-7, 30.0	95.035	65.237	
3H-7, 32.0	95.055		55.997
3H-7, 102.0	95.755		41.989
3H-7, 104.0	95.775	62.13	
3H-8, 44.0	96.52	96.465	
3H-8, 46.0	96.54		78.009
3H-9, 32.0–34.0	97.685	83.385	
3H-9, 36.0	97.725		57.233
3H-10, 15.0	98.395	58.86	
3H-10, 16.0	98.405		34.206
4H-1, 32.0	99.32	76.845	
4H-1, 35.0	99.35		59.152
4H-1, 110.0	100.1		54.355
4H-1, 112.0	100.12	76.845	
4H-3, 32.0	100.925		74.503
4H-3, 35.0	100.955	116.085	
4H-3, 114.0	101.745		68.746
4H-3, 116.0	101.765	89.925	
4H-4, 22.0	102.24		71.625
4H-4, 25.0	102.27	104.64	
4H-4, 126.0	103.28		55.314
4H-4, 129.0	103.31	85.02	
4H-5, 22.0	103.675	88.29	
4H-5, 25.0	103.705		58.192
4H-5, 116.0	104.615		77.381
4H-5, 118.0	104.635	96.465	
4H-6, 28.0	105.195	91.56	
4H-6, 30.0	105.215		56.273
4H-6, 118.0	106.095	114.45	
4H-6, 120.0	106.115		65.868
4H-7, 25.0	106.605	83.385	
4H-7, 28.0	106.635		59.152
4H-7, 107.0	107.425		56.273
4H-7, 110.0	107.455	88.29	
5H-1, 25.0	108.75	44.145	
5H-1, 28.0	108.78		21.734
5H-3, 23.0	110.34	81.75	
5H-3, 27.0	110.38		45.72
5H-3, 115.0	111.26		55.314
5H-3, 117.0	111.28	94.83	
5H-4, 28.0	111.795	62.13	
5H-4, 30.0	111.815		51.476
5H-4, 116.0	112.675	50.685	
5H-4, 118.0	112.695		41.882
5H-5, 15.0	113.065	73.575	
5H-5, 18.0	113.095		54.355
5H-5, 119.0	114.105		31.328
5H-5, 121.0	114.125	60.495	
5H-6, 19.0	114.5	62.13	
5H-6, 21.0	114.52		30.369
5H-7, 18.0	115.895	40.875	
5H-7, 20.0	115.915		23.652
5H-8, 24.0	116.93	32.7	
5H-8, 26.0	116.95		17.896
5H-9, 30.0	117.7	50.685	
5H-9, 32.0	117.72		36.125
6H-2, 25.0	118.5	76.845	
6H-2, 27.0	118.52		53.395
6H-2, 99.0	119.24		65.868
6H-2, 101.0	119.26	81.75	
6H-4, 37.0	120.17	88.29	
6H-4, 35.5	120.185		70.665
6H-4, 105.0	120.85		69.706
6H-4, 107.0	120.87	78.48	
6H-5, 27.0	121.48	80.115	
6H-5, 30.0	121.51		56.273
6H-5, 105.0	122.26		63.949
6H-5, 109.0	122.3	73.575	
6H-6, 26.0	122.87	98.1	
6H-6, 30.0	122.91		78.341
6H-6, 119.0	123.8		69.706
6H-6, 122.0	123.83	106.275	
6H-7, 23.0	124.26	111.18	
6H-7, 26.0	124.29		78.341
6H-7, 113.0	125.16		63.949
6H-7, 116.0	125.19	86.655	
6H-8, 47.0	125.905		65.868
6H-8, 50.0	125.935	81.75	
6H-8, 113.0	126.565		54.355
6H-8, 116.0	126.595	86.655	
6H-9, 28.0	127.075	101.37	

Table T15 (continued). (Continued on next page.)

Core, section, interval (cm)	Depth (mbsf)	Undrained shear strength (kPa)	
		Penetrometer	Vane shear
6H-9,30.0	127.095		58.192
6H-9, 100.0	127.795		65.868
7H-1, 30.0	127.8		43.801
7H-1, 32.0	127.82	42.51	
6H-9, 103.0	127.825	83.385	
7H-3, 18.0	129.63		54.355
7H-3, 20.0	129.65	75.21	
7H-5, 29.0	130.34	81.75	
7H-5, 31.0	130.36		53.395
7H-5, 101.0	131.06		53.395
7H-5, 103.0	131.08	73.575	
7H-6, 15.0	131.57	91.56	
7H-6, 18.0	131.6		64.908
7H-6, 101.0	132.43	81.75	
7H-6, 103.0	132.45		56.273
7H-8, 28.0	134.46	83.385	
7H-8 30.0	134.48		58.192
7H-8 125.0	135.43		68.746
7H-8, 127.0	135.45	63.765	
7H-9, 18.0	135.84	76.845	
7H-9, 20.0	135.86		53.395
7H-9, 86.0	136.52		70.665
7H-9, 88.0	136.54	96.465	
7H-10, 15.0	136.9	103.005	
7H-10, 17.0	136.92		64.908
7H-10, 51.0	137.26		104.246
7H-10, 54.0	137.29	135.705	
7H-10, 79.0	137.54	86.655	
7H-10, 81.0	137.56		47.639
8H-1, 58.0	137.58	76.845	
8H-1, 60.0	137.6		58.192
8H-3, 18.0	138.42	98.1	
8H-3, 21.0	138.45		86.976
8H-3, 122.0	139.46		77.381
8H-3, 125.0	139.49	103.005	
8H-4, 17.0	139.83	117.72	
8H-4, 20.0	139.86		86.976
8H-4, 114.0	140.8		71.625
8H-4, 117.0	140.83	96.465	
8H-5, 26.0	141.33	106.275	
8H-5, 28.0	141.35		74.503
8H-5, 116.0	142.23		72.584
8H-5, 118.0	142.25	83.385	
8H-6, 22.0	142.75	116.085	
8H-6, 25.0	142.78		93.692
8H-6, 115.0	143.63		102.327
8H-6, 113.0	143.66	142.245	
8H-7, 23.0	144.16	168.405	
8H-7, 25.0	144.18		90.813
8H-7, 92.0	144.85		76.422
8H-7, 94.0	144.87	107.91	
8H-8, 38.0	145.71	83.385	
8H-8, 40.0	145.73		54.355
8H-8, 121.0	146.54		53.395
8H-8, 124.0	146.57	71.94	
9H-1, 19.0	146.69	104.64	
9H-1, 22.0	146.72		77.381
9H-3, 29.0	148.045	89.925	
9H-3, 31.0	148.065		75.462
9H-3, 112.0	148.875		82.178
9H-3, 114.0	148.895	112.815	
9H-4, 27.0	149.455	89.925	
9H-4, 30.0	149.485		77.381
9H-4, 114.0	150.325		113.84
9H-4, 116.0	150.345	142.245	
9H-5, 91.0	151.505	152.055	
9H-5, 94.0	151.535		115.759
9H-6, 18.0	152.205	119.355	
9H-6, 20.0	152.225		103.286
9H-6, 107.0	153.095		96.57
9H-6, 109.0	153.115	93.195	
9H-7, 27.0	153.705	148.785	
9H-7, 30.0	153.735		94.651
9H-8, 17.0	155.015	130.8	
9H-8, 20.0	155.045		85.057
10H-1, 57.0	155.57		58.192
10H-1, 59.0	155.59	81.75	
10H-2, 15.0	155.795	138.975	
10H-2, 19.0	155.835		100.408
9H-8, 101.0	155.855		54.355
9H-8, 104.0	155.885	94.83	
10H-3, 22.0	157.275	201.105	
10H-3, 25.0	157.305		153.177
10H-4, 23.0	158.675	150.42	
10H-4, 26.0	158.705		86.016
10H-6, 17.0	160.555	189.66	
10H-6, 20.0	160.585		142.623
10H-9, 20.0	162.545	94.83	
10H-9, 23.0	162.575		61.071
10H-10, 90.0	164.655		59.152
10H-10, 92.0	164.675	80.115	
11H-1, 51.0	165.01	207.645	
11H-1, 54.0	165.04		140.704
11H-2, 34.0	166.12		161.812
11H-2, 36.0	166.14	246.885	
11H-3, 21.0	167.39	233.805	
11H-3, 24.0	167.42		178.122
12H-1, 36.0	169.86	155.325	
11H-5, 55.0	169.885	241.98	
12H-1, 39.0	169.89		96.57
11H-5, 59.0	169.925		175.244
11H-5, 63.0	169.965	N/A	
11H-5, 70.0	170.035		N/A
11H-5, 105.0	170.385	129.165	
11H-5, 110.0	170.435		70.665
12H-3, 47.0	170.66	199.47	
12H-3, 50.0	170.69		138.785
11H-6, 38.0	171.18	106.275	
11H-6, 40.0	171.2		68.746
12H-4, 14.0	171.745	130.8	
12H-4, 19.0	171.795		87.935
13T-1, 21.0	175.71	55.59	
13T-1, 24.0	175.74		30.369
13T-1, 105.0	176.55		78.341
13T-1, 110.0	176.6	116.085	
13T-4, 65.0	178.22		66.827
13T-4, 66.0	178.23	104.64	
13T-4, 124.0	178.81		84.097
13T-4, 126.0	178.83	98.1	
13T-5, 102.0	179.99		51.476
13T-5, 106.0	180.03	101.37	
13T-6, 4.0	180.23	93.195	
13T-6, 8.0	180.27		46.679
13T-6, 111.0	181.3		50.517
13T-6, 115.0	181.34	93.195	
13T-7, 15.0	181.65		63.949
13T-7, 18.0	181.68	125.895	
13T-8, 22.0	182.655	109.545	
13T-8, 25.0	182.685		70.665
14T-1, 16.0	185.16	49.05	
14T-1, 20.0	185.2		29.409
14T-1, 93.0	185.93		46.679
14T-1, 95.0	185.95	65.4	
14T-3, 23.0	186.92	96.465	
14T-3, 26.0	186.95		51.476

Table T15 (continued).

Core, section, interval (cm)	Depth (mbsf)	Undrained shear strength (kPa)	
		Penetrometer	Vane shear
14T-4, 41.0	188.57	81.75	
14T-4, 45.0	188.61		51.476
14T-5, 30.0	189.89	99.735	
14T-5, 34.0	189.93		73.543
14T-6, 32.0	191.315		74.503
14T-6, 34.0	191.335	114.45	
14T-7, 7.0	192.545		34.206
14T-7, 14.0	192.615	80.115	
14T-8, 35.0	193.365		59.152
14T-8, 52.0	193.535	119.355	